Photoelectric Behavior and Photovoltaic Performance of Bismuth Chalcohalides

Sen Li

Kagawa University

Japan

September 2021

Table of contents

Chapter I

General Introduction

As the global demand for energy is expected to grow rapidly, the securing of clean energy is essential for sustainable economic growth. Photovoltaics (PVs), which directly convert solar energy to electric energy, offer a practical solution to challenge the increasing demand for sustainable energy.[1, 2] The solar cell is a photovoltaic device that can separate the excited electrons and holes before they relax and forces them to flow through an external circuit.[3] In the solar cell, a light absorber material generates the excited electrons and holes by absorption of light, where the recombination of the excited electrons and holes also occurs simultaneously. Therefore, the development of the suitable light absorber materials, which can efficiently achieve the charge separation process, is a primary challenge for the development of high performance solar cells, since the first practical solar photovoltaic cell was created in 1952 by Chapin, Fuller and Pearson at Bell Labs.[4] Various semiconductor materials have been applied as light absorber for development of PVs in the past several decades.

At the present, the photovoltaic market is dominated by crystalline silicon panels which possess relatively high efficiency, but the high cost has prompted the development of low cost high performance PVs. Some new types of PVs, such as the thin film type of $CuIn_{1-x}Ga_xSe_2$ (CIGS) and CdTe PVs, have been developed to reduce the cost and increase power conversion efficiency (PCE). Although the PCE of these PVs having recently reached 22%, their potential and future prospect are limited by the high cost of indium and scarcity of tellurium. In the past decade, the hybrid organic-inorganic lead halide perovskites solar cells (PSCs) have gained huge attention and already achieved an excellent PCE of 25%.[5] Unfortunately, the intrinsic instability of PSCs and the environmental risk of toxic Pb are still unresolved, limiting its commercial applications.[6] As a potential alternative candidate for the lead halide perovskites, bismuth-based materials have gained increasing attention in the

photovoltaic field because bismuth is a non-toxic and non-bioaccumulating element.[7] Undoubtedly, figuring out the connection between the semiconductor and photovoltaic behavior is significant for the material engineering of PVs.

In this chapter, general information about solar energy, including semiconductors for solar cells, evolution of solar cells, performance parameters of solar cells, and factors affecting the performance of solar cells are described. In addition, we put emphasis on Bi-VI-VII compounds, including the synthesis processes, the physical and chemical properties, and the applications. Furthermore, the purposes of this dissertation are also presented.

1.1 Solar energy

Energy is necessary for human life. The evolution of humanity is also a history of energy revolution. One of the main factors that characterize the production of energy is the resource that is being exploited. The available energy resources can be divided in two main categories: non-renewable and renewable. The first category includes mainly the nature sources that are finite in quantity, or need a long time to regenerate. So it is considered as non-renewable energy resource. An example is carbon-based fossil fuel, such as coal and oil. This king of resources can release relative high energy. The second category, namely renewable energy resources, includes carbon neutral sources, such as sunlight, wind, rain, tides, waves, and geothermal heat, which are naturally replenished on a human timescale. Compared with the renewable sources, the energy currently obtained from the non-renewable sources is much higher at the present. However, as a theoretically inexhaustible source of energy, developing renewable energy attracts a lot of attention, especially in view of a depletion of non-renewable sources in the near future.

Among all the energy sources, both renewable and non-renewable, solar energy is the most environmental friendly renewable energy and attracted a lot of interests. The idea to convert sunlight into usable electric energy is the base concept of the solar cell.

The solar cell is an optoelectronic device able to convert light into electric current, including both the sun light and also artificial or ambient light. The sun emits electromagnetic waves of all over the spectrum of frequencies like a black body with a temperature of 5777 K.[8] Only a fraction of this radiation reaches the surface of the Earth. The air mass coefficient (AM1.5) defines the direct optical path length through the Earth's atmosphere used to determine the effective electromagnetic radiation emitted by the sun at the sea level. Figure 1.1 shows the solar irradiance spectrum above the atmosphere and at the surface. Most of the irradiance occurs between 250 and 2500 nm with the maximum in the visible region of light (wavelength from 400 to 700 nm), which means that solar cells should strive to absorb the visible light in the solar spectrum as much as possible.

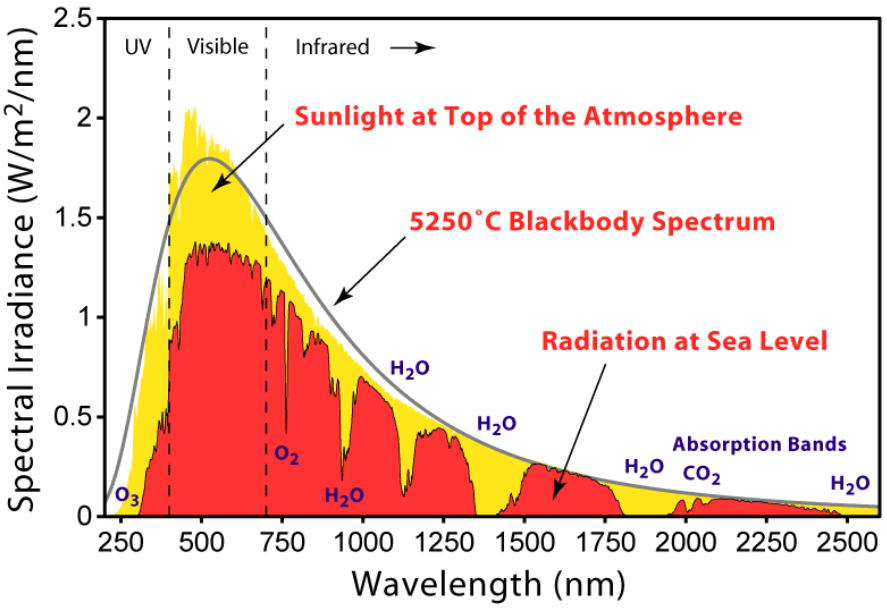

Figure 1.1 Solar irradiance spectrum above the atmosphere and at the surface. Reproduced with permission, Copyright Wikimedia commons.

A solar cell can absorber light and convert it into electric current, where light goes in and electrons go out. Generally, solar cells must respect the following characteristics:[8]

i. Absorb the incident light. Light must be absorbed before converted into electric current. It is one of the most important characteristic for the material and is dependent on the absorption spectrum of the material. A material's absorption spectrum is the fraction of incident radiation absorbed by the

material over a range of frequencies and is determined by the atomic and molecular composition of the material. An ideal material for PVs has an absorption spectrum that matches with the AM1.5 solar spectrum.

ii. Generate charges. The core of PVs must be able to generate carriers when light fall on the material. The photogeneration defines the type of solar cells. Semiconductors used in the solar cells must meet these requirements to efficiently produce carriers, where their electronic band structures are very important.

iii. Transport carriers. PVs need to collect, separate, and transport the carriers generated by light absorption immediately, because the photogenerated electrons and holes will immediately recombine without driving force. So PVs form an internal electric field named as build-in field to separate and transport the electrons and holes in opposite directions.

1.2 Semiconductors for solar cells

1.2.1 Bandgap and light absorption

When two atoms form a molecule, the respective electron orbitals in the atoms combine together to form molecular orbitals, with new energy levels. When this process is repeated to form a solid, each atomic orbital splits in a continuum of levels forming a “band”. as shown in Figure 1.2. Now, these bands may or not overlap and this is due to the energy distribution, which is a reflection of the electronic properties of the atoms. The occupation of these bands depend on the original occupation of the molecular orbitals. The highest occupied band is defined as the valence band (VB). The lowest unoccupied band is defined as conduction band (CB). If the valence band and the conduction band overlap, the solid is a metal. If the two band are separated in energy, the solid is a semiconductor or an insulator. And if the separation is large, the solid is an insulator. The separation in energy (eV) between the two bands, namely bandgap

energy, determine the type of material: metals - 0 eV, semimetals - less than 0.5 eV, semiconductors - between 0.5 and 3 eV, insulator more than 3 eV.

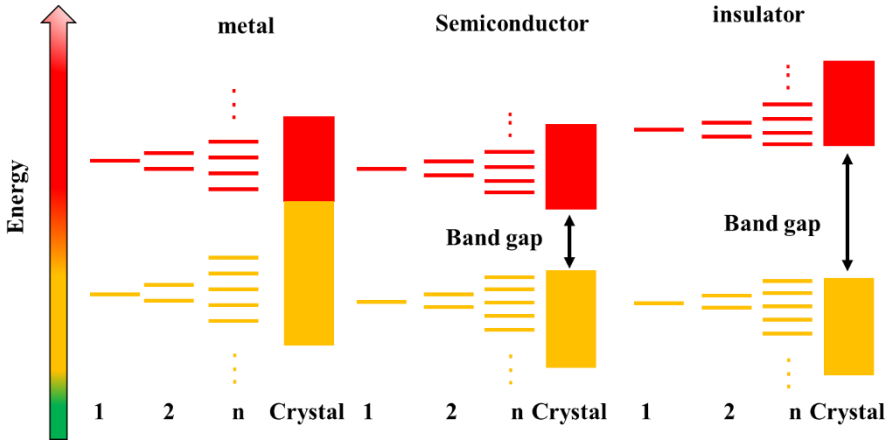

Figure 1.2 Nature of the band structure for a metal and a semiconductor.

When an electron is promoted from the VB to the CB, a positively charged vacancy remains in the VB. This vacancy is usually filled by the near electrons in the VB, moving the vacancy to the neighbor site. In the presence of an electric field this process can be repeated, resulting in a current represented by the movement of the vacancy in the opposite direction to the promoted electron. Since this vacancy results from a lack of negative charge (missing one electron), the relative current can be described as the current of positive holes in the VB. The electron and the relative hole are charges with opposite signs. Usually these two charges are considered independent one from the other, however in some conditions they can be interacting. In this particular conditions the Coulomb interaction, which is manifested between charges with opposite sign, bind the electron and the holes in a unique state that is called an exciton. These excitons can be both stationary or mobile within the material. They result in a series of intra-band gap states slightly above the VB and below the CB. Although excitonic states are not relevant for electrons and holes in isolation, they are important for the optical properties of semiconductors.

An excellent light absorber material for solar cells should absorb visible light because most of the light energy of solar spectrum located in the visible light range. Semiconducting and insulating materials possess bandgaps, but only semiconductors

have the suitable bandgap for visible light absorption, since the bandgap of insulators is too large.[8] The nature of the bandgap in a semiconductor is related to its atomic characteristics.[9]

1.2.2 Carrier generation and recombination

Generation is an electronic excitation event which increases the number of free carriers available to carry charge. Recombination is an electronic relaxation event that reduces the number of free carriers.[10] Generation is a process that requires energy; this energy can be provided by vibration (phonons), or light (photons). Recombination is a process that releases energy, with the inverse mechanisms of generation. For every generation process there is a recombination process.

The generation of charges from light absorption is called photogeneration, such as in solar cells. This process starts with the absorption of a photon and the promotion of an electron from the VB to the CB, creating an electron-hole pair, namely exciton. Recombination is the decay of the electron from the CB back to the lower state. when an electron is excited it quickly decays to the minimum energy of the conduction band, this process takes few femtoseconds.[9] Then the recombination to the valence band occurs with a slower mechanism which takes several microseconds, giving enough time to the solar cell to extract the electron. This process is sketched in Figure 1.3.

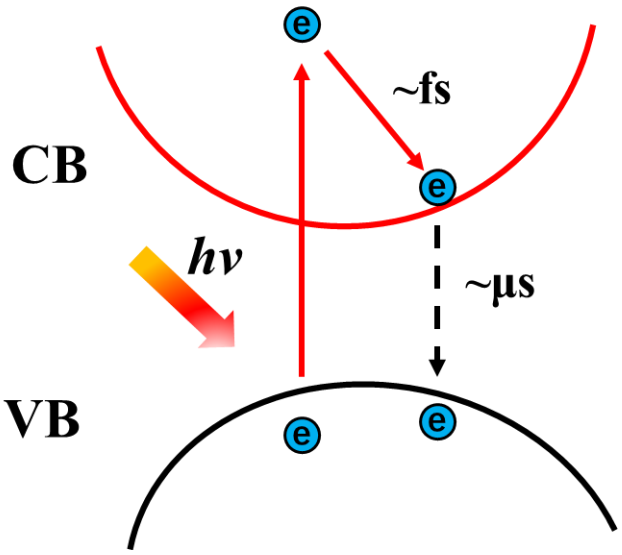

Figure 1.3 Excitation mechanism of an electron from the valence band (VB) to the

conduction band (CB) by the absorption of a photon.

The term recombination includes one or more mechanisms that reduce the number of mobile electrons and holes. There are two kind of recombination: unavoidable and avoidable.

Unavoidable recombination.

This mechanism is related to the intrinsic physical processes of the material. Radiative recombination and Auger recombination belong to this category.

Radiative recombination: Radiative recombination is the spontaneous emission of a photon from the recombination of an electron with a hole at the minimum/maximum of the CB/VB respectively. The energy of the emitted photon is equal to the band gap. It is one of the most important recombination mechanism in photovoltaics.

Auger recombination: It is the collision of two similar carriers, for example electrons. In this non-radiative process one carrier transfers its kinetic energy to the other carrier. This leads to the decay of the first carrier in the VB and the promotion of the second carrier to high energy excited states before decaying and losing its energy in the form of phonons.

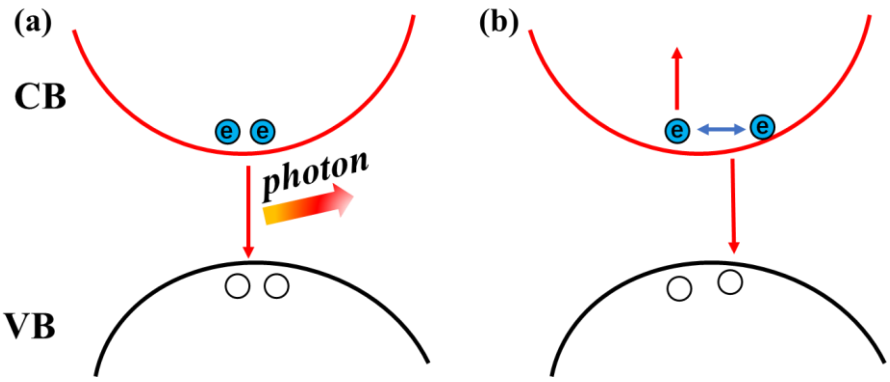

Figure 1.4 Unavoidable recombination mechanisms: radiative recombination (a), Auger recombination (b).

Avoidable recombination.

This mechanism is related to defects and impurities in the material, such as recombination through traps states and grain boundaries, as shown in Figure 1.5.

Traps states: Traps states locate sub-bandgap levels that act as a sink for both excited electrons and holes, like a potential well. These states act as recombination centers when the energy of the state lies deep within the bandgap such that recombination with the opposite carrier is much more likely than thermal detrapping back into the band. Otherwise electrons and holes can be detrapped, resulting in a slower current.

Grain boundaries recombination: Surfaces and grain boundaries in polycrystalline films are defects rich zones. Localized states, like broken bonds or extrinsic impurities can create recombination centers similar to the traps states, shortening the electron and holes capturing time.

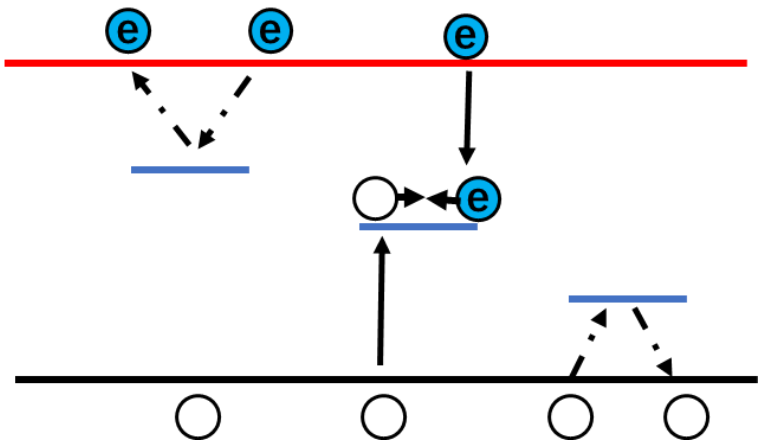

Figure 1.5 Avoidable recombination assisted by trap state.

1.2.3 Direct and indirect semiconductors

In semiconductor physics, the band gap of a semiconductor can be of two basic types, a direct band gap or an indirect band gap. Generally, the minimal-energy state in the conduction band and the maximal-energy state in the valence band are each characterized by a certain crystal momentum (k-vector) in the Brillouin zone. If the k-vectors are different, the material is indirect semiconductor. if the crystal momentum of electrons and holes is the same in both the conduction band and the valence band, the material is direct semiconductor, as shown in Figure 1.6.[11]

Electronic optical absorption processes are called direct transition if only an

optical photon is involved in the process. A direct optical transition involving the absorption of a photon only with the creation of an electron and a hole, with no phonon involved. The energy of a photon absorbed must be equal to the bandgap energy for a transition from the top of the valance band to the bottom of the conduction band, and there is almost no change in K upon making the transition. The direct transition is shown in Figure 1.7(a). If the limits of the energy bands plotted against the wave vector K the conduction band minimum and valance band maximum occur at , then the absorption edge makes well. In Figure 7(a) only vertical transitions are allowed. Non-vertical transitions are normally forbidden.[12]

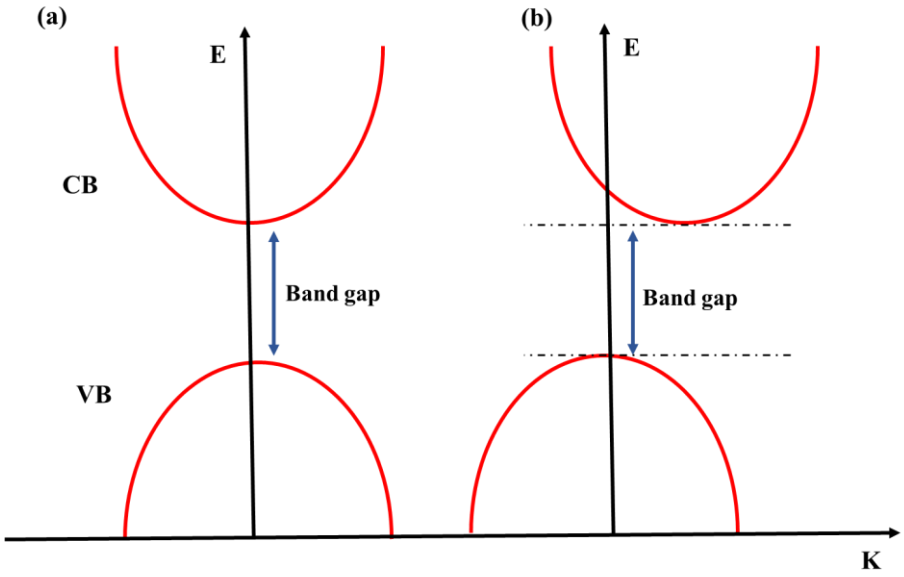

Figure 1.6 (a) Direct and (b) indirect bandgap.

As for indirect transition, it is a reverse of the direct absorption process. In an indirect gap material, the conduction band minimum and valance band maximum are at different points in the Brillion zone. Indirect transitions can be thought of as a two-step process: (1) absorption of a photon; (2) absorption of a phonon. Figure 1.7(b) shows the E-K diagram of an indirect transition, the conduction band minimum does not occur at K = 0, but rather at some other value of K. Both photon absorption and emission and absorption of photons are considered.[12]

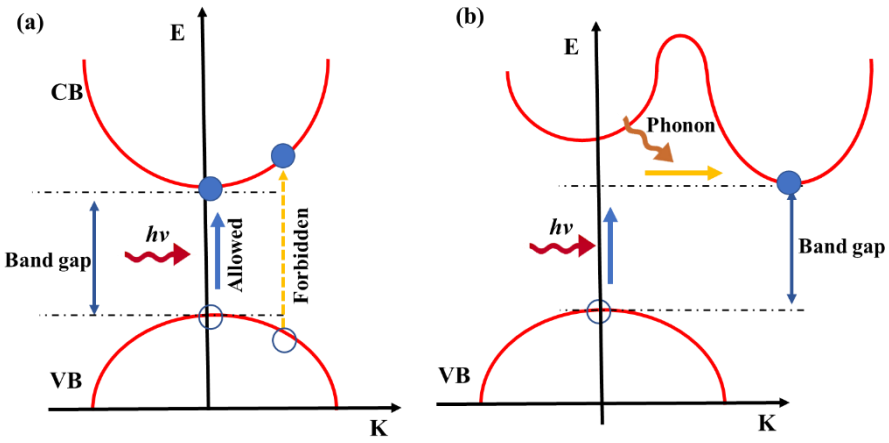

Figure 1.7 (a) Diagram of direct and (b) indirect transition processes.

According to above explanation, direct bandgap semiconductors are better than the indirect band gap semiconductors for solar cell applications. This is because direct bandgap materials have strong optical transitions between the valence and conduction band. However, indirect materials have fairly weak optical transitions since absorption and emission of a photon must occur with the simultaneous absorption or emission of a phonon.

1.3 Evolution of solar cells

Solar cells are usually divided into three main categories. The 1st generation contains solar cells that are relatively expensive to produce, and have a low efficiency. Single crystal silicon solar cells are the typical 1st generation solar cells, which account for about 85% of commercial market share of the devices today. But its market expansion is hampered by high cost of single crystal silicon. The 2nd generation solar cells, such as thin film type of $CuIn_{1-x}Ga_xSe_2$ (CIGS) and CdTe PVs, use the thin-film technology for minimizing material consumption to reduce cost, although their efficiencies are even lower than that of the 1st generation cells. In this way, the cost to generate per watt is lower than in the first generation cells. These thin films can also be grown on flexible substrates. Therefore, they have some other advantages, such as flexibility, lightness, and visual aesthetic. They are much more applicable on windows,

cars, building integrations etc. The 3rd generation of solar cells, such as perovskite PVs, dye-sensitized PVs, and organic semiconductor PVs, would be extremely higher efficiency and lower cost than those of the 2nd generation cells. The thin film solar cells used low cost materials are the mainstream of the 3rd generation cells, which is considered to be the most promising technologies for the evolution of PVs. Figure 1.8 shows efficiency versus cost for the three generations of solar cells.

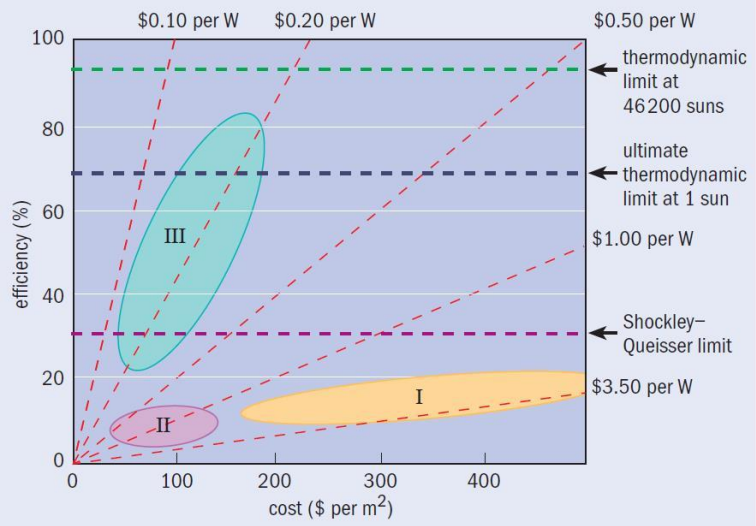

Figure 1.8 Efficiency versus cost for the three generations of solar cells. Reproduced with permission.[13] Copyright IOP science.

Figure 1.9 exhibits evolution of the best research-cell efficiencies (PCE) for various solar cells. At the present, the PCE of the 3rd generation cells are not reaching to the single crystalline silicon, but this generation of solar cells can dramatically lower the costs of materials and fabrication process. Especially, the fabrication process cost can be lowered by using solution-processed techniques, including industrial printing techniques such as roll-to-roll, slot dye, inkjet printing and bar coating, which are easily scalable to large productions.

According Shockley-Queisser limit, the single-junction solar cells can achieve a maximum efficiency of 33.7%.[14] To further improve the efficiency, multijunction solar cells were developed by stacking several p/n junction layers of semiconductors in order to cover the whole solar spectrum. The multijunction solar cells retain the record in

terms of PCEs. The applications of the 3rd generation cells to the multijunction solar cells and on flexible substrates are attracting more and more interest due to their potential high PCE and low cost benefits and broad applications.

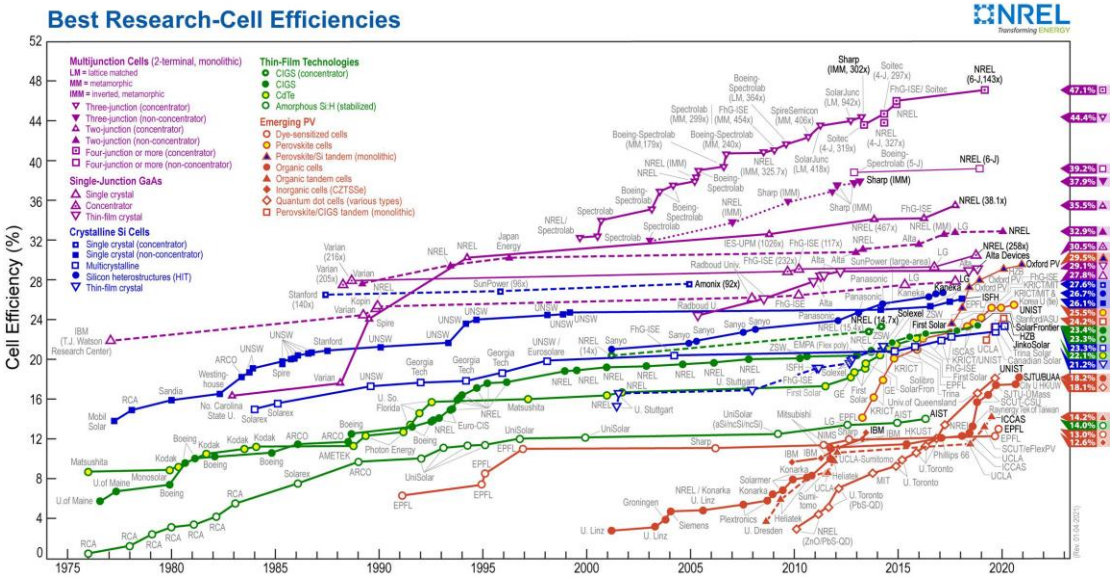

Figure 1.9 Best Research-Cell Efficiency Chart. From NREL (National Renewable Energy Laboratory) website.[15]

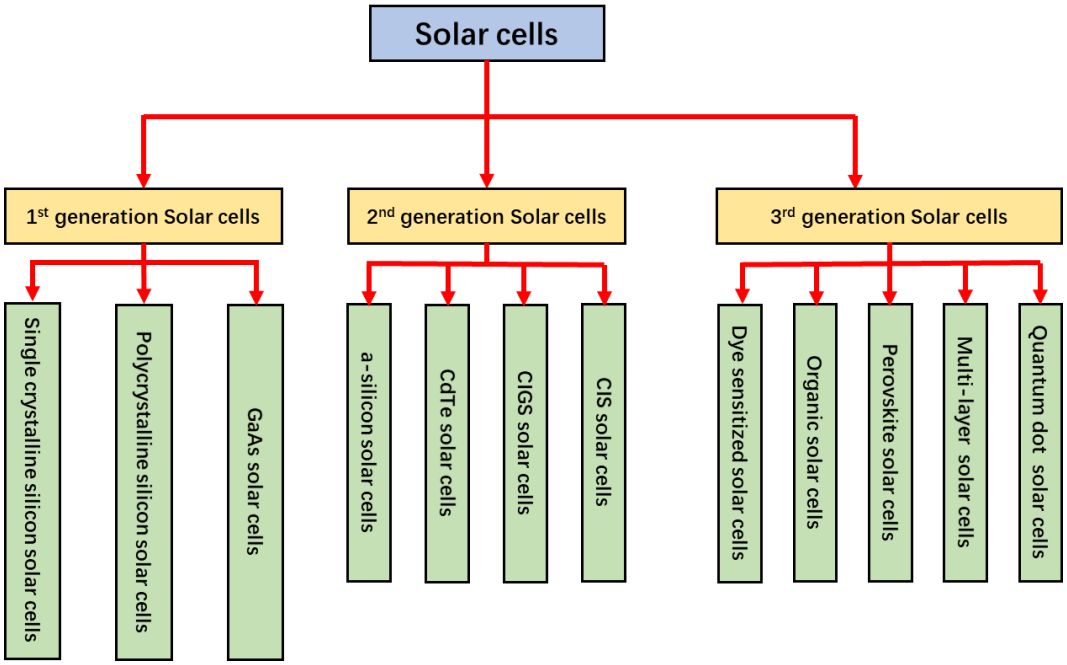

Figure 1.10 Classification of solar cells.

1.3.1 The 1st generation solar cells

Single-crystal silicon

Most of silicon solar cells are fabricated from silicon wafers, which may be either single-crystalline or multi-crystalline. Single-crystal silicon cells are the most common in the PV industry. Czochralski method is the main technique for producing single-crystal silicon.[16] A single-crystal silicon seed is dipped into a quartz crucible where contains melted high-purity polycrystalline. A single-crystalline can be formed with the seed slowly pulled from the melt. The ingots are then sawed into thin wafers about 200-400 μm. The thin wafers are then polished, doped, coated, interconnected and assembled into modules and arrays. A single-crystal silicon has a uniform molecular structure. Compared to non-crystalline materials, its high uniformity results in higher energy conversion efficiency. The higher a PV cell's conversion efficiency, the more electricity it generates for a certain area of exposure to the sunlight. The PCE for single-silicon commercial modules ranges between 15-20%.[8] Not only are they energy efficient, single-silicon modules are highly reliable for outdoor power applications.[17]

Polycrystalline silicon

Consisting of small grains of single-crystal silicon, Pol PV cells are less energy efficient than single-crystalline silicon PV cells. The grain boundaries in polycrystalline silicon hinder the flow of electrons and reduce the power output of the cell. The PCE for a commercial module made of polycrystalline silicon ranges between 10 to 14%.[18] Slicing thin wafers from blocks of cast polycrystalline silicon is a common way to produce polycrystalline silicon PV cells. Another more advanced method is the "ribbon growth" method in which silicon is grown directly as thin ribbons or sheets with the approach thickness for making PV cells. The cost is lower compare with single-crystal silicon because of no sawing process. The most commercially developed ribbon growth approach is edge-defined film-fed growth.[19] Compared to single-crystalline silicon, polycrystalline silicon material is stronger and can be cut into one-third the thickness of single-crystal material. It also has slightly lower wafer cost and less strict growth requirements. However, their lower manufacturing cost is offset by the lower cell

efficiency.

Gallium Arsenide (GaAs)

GaAs possesses a crystal structure similar to that of silicon. GaAs solar cells were thoroughly studied, and quickly became a reference system for thin film solar cells due to their good electric, heat resistant properties, high efficiency and performance. An advantage of GaAs is that it has high level of light absorptivity. To absorb the same amount of sunlight, GaAs requires only a layer of few micrometers thick while crystalline silicon requires a wafer of about 200-300 μm.[20] Also, GaAs has a much higher energy conversion efficiency than crystal silicon, reaching about 25 to 30%. Its high resistance to heat makes it an ideal choice for concentrator systems in which cell temperatures are high. GaAs is also popular in space applications where strong resistance radiation damage and high cell efficiency are required. The biggest drawback of GaAs PV cells is the high cost of the single-crystal substrate that GaAs is grown on. Therefore it is most often used in concentrator systems where only a small area of GaAs cells is needed.

1.3.2 The 2nd generation solar cells

The second generation solar cells is based on the thin-film solar cells, which include amorphous Si (a-Si), cadmium telluride/cadmium sulfide (CdTe/CdS), copper indium diselenide (CIS) and copper indium gallium selenide (CIGS) solar cells. Their efficiencies are less than 1st generation, their costs are also less than 1st generation. In addition they have an advantage in visual aesthetic. Since there are no fingers in front of the thin film solar cells for metallization, they are much more applicable on windows, cars, building integrations etc.[21]

Amorphous Silicon (a-Si)

Amorphous silicon solar cells are mostly used in consumer electronic products, which require lower power output. Amorphous silicon has been the dominant thin-film PV material since it was first discovered in 1974.[22] Amorphous silicon is a non-crystalline form of silicon i.e. its silicon atoms are disordered in structure. A significant

advantage of a-Si is its high light absorptivity, about 40 times higher than that of single-crystal silicon. Therefore only a thin layer of a-Si is sufficient for making PV cells (about 1 μm thick as compared to 200 or more micrometers thick for crystalline silicon cells). Also, a-Si can be deposited on various low-cost substrates, including steel, glass and plastic, and the manufacturing process requires lower temperatures and thus less energy. So the total material costs and manufacturing costs are lower per unit area as compared to those of crystalline silicon cells. Despite the promising economic advantages, a-Si still has two major roadblocks to overcome. One is the low PCE, ranging between 5- 9%, and the other is the outdoor reliability problem in which the efficiency degrades within a few months of exposure to sunlight, losing about 10 to 15%.

Cadmium Telluride (CdTe)

As a polycrystalline semiconductor compound made of cadmium and tellurium, CdTe has a high light absorptivity level only about a micrometer thick can absorb 90% of the solar spectrum.[23] Another advantage is that it is relatively easy and cheap to manufacture by processes such as high-rate evaporation, spraying or screen printing. The PCE for a CdTe commercial module is about 7%, similar to that of a-Si. The instability of cell and module performance is one of the major limitation of using CdTe for PV cells. Another disadvantage is that cadmium is a toxic substance. Although very little cadmium is used in CdTe modules, extra precautions have to be taken in manufacturing process.

Copper Indium Gallium Selenide (CIGS)

Since its initial development, copper indium diselenide ($CuInSe_2$) thin-film technology has been considered promising for solar cells because of its favorable electronic and optical properties. It was later found that by substituting gallium (Ga) for indium (In), the bandgap can be increased from about 1.04 eV for copper indium diselenide (CIS) films to about 1.68 eV for copper gallium diselenide (CGS) films. Optimal devices have been fabricated with only a partial substitution of Ga for In, leading to a substantial increase in overall efficiency and more optimal bandgap. These solar cells are commonly known as a copper indium gallium diselenide [$Cu(In_xGa_{1-}$

$_x$)Se_2], or CIGS, cells. Up to now, the PCE of CIGS solar cells in laboratory have over 20%, but its commercial modules is limited between 12 to 14%.[24]

1.3.3 The 3rd generation solar cells

Third generation solar cells are emerging as novel PV technologies. They aimed to achieve both high PCE and low cost. This type of solar cells was widely adopt semiconductor nanoparticle as a light absorbers, which could give a high current. In this concept, it was thought the most promising generation solar cells attracted more researchers' attention. In addition, this type of solar cells are potentially overcome the Shockley-Queisser efficiency limit for single bandgap solar cell by using semiconductor nanoparticles.[25] Commonly, third-generation solar cells include multi-layer cells made of a-silicon or GaAs, dye-sensitized solar cells (DSSCs), organic solar cell, hybrid perovskite solar cells and quantum dot solar cells (QDSSCs).[26] The champion PCE achieved so far was about 14% for DSSCs, and as for the QDSSCs, between 8 to 10% has been achieved. As regard organic solar cells, the PCE has achieved 10 to 15% up to now.[27] Surprisingly, the perovskite solar cells (PSCs) with hybrid organic-inorganic perovskite as a light absorber have achieved over 24% since it was emerged in 2009.[28] In addition, some others methods also also employed to improve the PCE, like hot carrier cells, multiband cells and tandem solar cells.

1.3.3.1 Dye-sensitized solar cell (DSSCs)

Principle and mechanism of DSSCs

Dye-sensitized solar cells are considered as a new paradigm for the low-cost and high-efficiency solar cells. Pioneered by Michael Grätzel and co-workers in 1991.[29] A typical DSSCs consists of totally four components, namely, photoanode, sensitizer, electrolyte and a counter electrode. A photoanode is typically a nanocrystalline TiO_2 coated on the FTO conducting glass substrate. Various morphologies of TiO_2 nanomaterials such as spherical, rod, hierarchical and tubular were analyzed effectively for the photoanode applications. These structures strongly affect the light harvesting, charge injection and charge-collecting properties of the DSSCs. Since TiO_2 is a wide

bandgap material (E_g = 3.2 eV for anatase phase), its absorption range is limited only up to the UV region. To improve the light absorption in the visible region, organometallic ruthenium-based dyes are used as effective sensitizers. Upon illumination of the dye, electron from the highest occupied molecular orbital (HOMO) transfers to lowest unoccupied molecular orbital (LUMO) which then transfers into the photoanode in a femtosecond time scale. Ruthenium-based molecular sensitizers such as cis-di (thiocyanato) bis (2,20-bipyridyl)-4,4- 0-dicarboxylate) ruthenium(II) (termed as N3 or N-719 dye) which absorbs photons in the wavelength of 400–800 nm are extremely effective for improving PCE of DSSCs.[30-32] These dyes have good anchoring groups like -COOH in its side chain which helps them to get better adsorption with surface of the highly mesoporous TiO_2 layer. In addition, potential compounds such as osmium(II) complex, metal-free dyes, organic dyes and porphyrin dyes were also analyzed.[33] Natural dyes are another group of dyes frequently used to achieve low-cost DSSCs, but still the PCE of natural dyes are very low compared with the ruthenium-based molecular dyes.

Methods like incorporation of energy relay dyes, co-sensitization have been observed as suitable ways to enhance the efficiency of the DSSCs. A redox electrolyte solution is employed to regenerate oxidized dye molecule to complete the external circuit. Generally, iodine/tri-iodide (I^-/I_3^-) electrolyte solution is widely adopted for this process; other compounds like Br^-/Br_3^-, $SCN^-/ (SCN)_3^-$ and $SeCN^-/(SeCN)_3^-$ were also used.[34] Ionic liquids is also alternative as the potential electrolytes for DSSCs. In view of the risk of leaking or freezing of electrolyte solution, solid-state dye-sensitized solar cells have also studied. Spiro-OMeTAD is a solid-state hole-transporting materials widely used in DSSCs.

Platinum-coated FTO is commonly used as counter electrode. In recent years, low-cost good electrocatalytic materials have attracted more attention to replace platinum. The basic device configuration and energy level diagram of a DSSC are given in Figure 1.11.

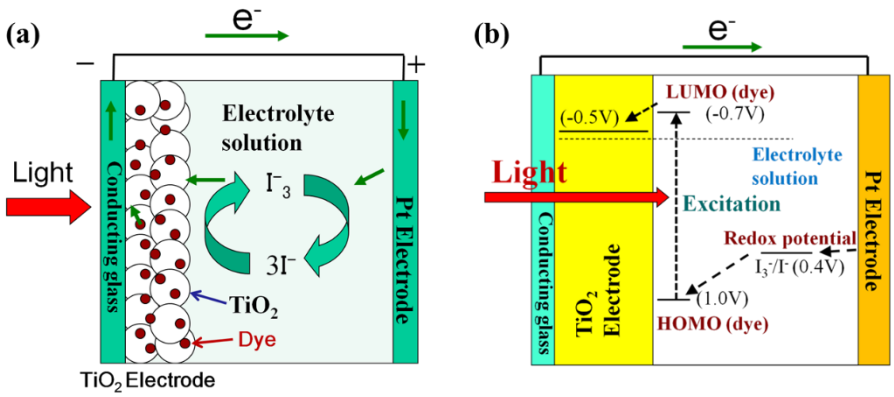

Figure 1.11 (a) Basic structure of a DSSC and (b) illustration of the typical energy diagram of DSSC.

Factors affecting PCE of DSSCs

Once the electrons from photoexcited dye are injected into the TiO_2 layer, it's oxidized by the receiving electrons from redox electrolyte. Hence, the redox electrolyte should get reduced by the electrons from the external circuit, as shown in Figure 1.12. In this stage, the counter electrode plays a major role in injecting electrons to redox electrolyte. The suitable counter electrode material for DSSC is identified based on its ability to reduce the over potential. The intrinsic catalytic activity of the counter electrode material functioning as effectively to regenerate the redox electrolyte.[35] The most commonly used counter electrode material for the DSSCs is a noble metal, platinum. In order to lower the cost, many compounds/nanocomposites including carbon-based materials, conducting polymers, metal sulfides, metal oxide materials, transition metal nitrides and carbides have been used for the counter electrode applications.[34, 36] Typical PCE records of DSSCs using various counter electrodes are shown in Figure 1.13. The results clearly suggest that these materials are almost equal or superior performance in DSSCs.

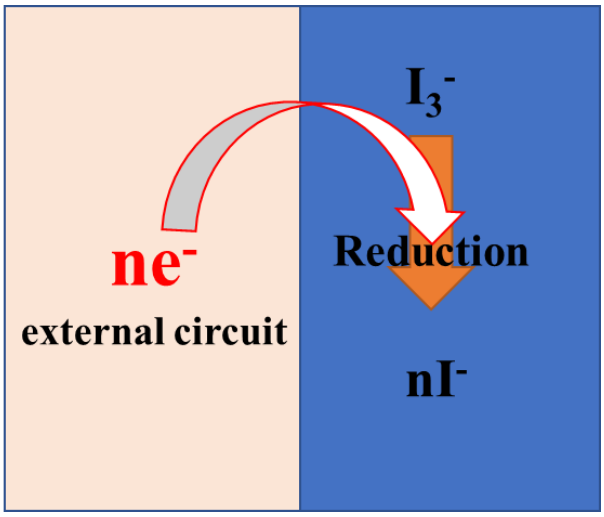

Figure 1.12 Schematic diagram of reduction of electrolyte at the counter electrode of DSSC.

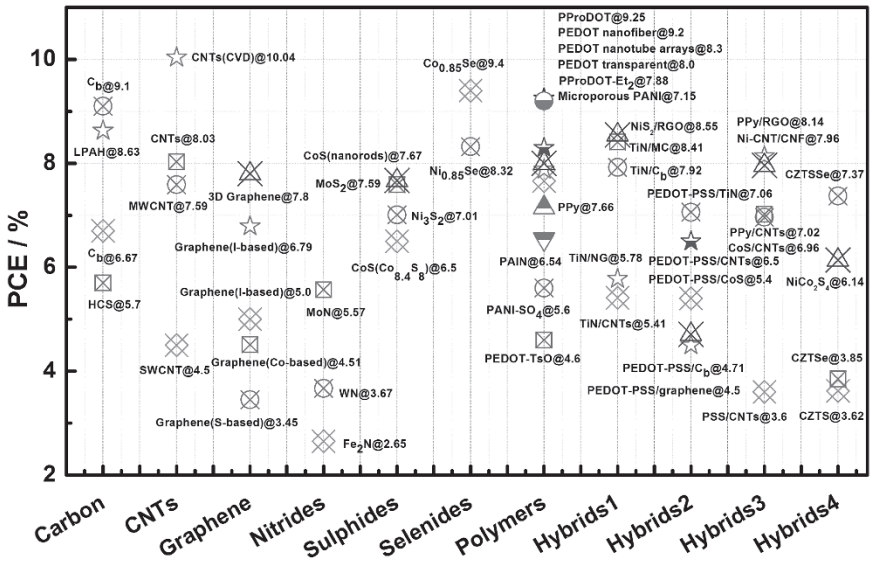

Figure 1.13 PCE records of DSSCs with typical counter electrodes. Reproduced with permission.[36] Copyright Wiley online library.

Stability of DSSCs is also a critical issue to handle since the organometallic dyes and electrolytes are not quite stable for a long time. Contamination of photocathode, incorporation of oxygen and moisture from atmosphere, desorption and degradation of dyes, degradation of all components by UV light irradiation from the sunlight and thermal stress, etc. are the major existing challenges in improving the stability.[37] Electrolytes have a risk of leaking from the device, and hence proper sealants like Surlyn, Bynel or certain kind of resins are required to seal the device.[38]

From the above discussions, development of new dyes and new inorganic

nanomaterials will have new possibilities in improving the PCE of DSSCs. Also, exploration of methods to improve dye loading, stability will be also effective ways.

1.3.3.2 Perovskite Solar Cells

Perovskite solar cells (PSCs) based on organic-inorganic perovskites (OIP) have been receiving increasing attention due to their impressive efficiency record within the past decade. The PCE over 25% has been achieved for OIP recently.[39] OIP are having the common structure of ABX_3 in which A is organic cation (e.g. CH_3NH_{3+},$C_2H_5NH_3$ etc.) and X is halide ion (Cl^-, Br^-, I^-), as shown in Figure 1.14.[40] $CH_3NH_3PbX_3$ (X = Cl^-, Br^-, I^-) are a class of perovskites that are most commonly studied as promising photovoltaic applications since 2009. Having the common structural formula of ABX_3, the high absorption coefficient of OIPs in the visible region (from 380 to 750 nm), particularly, $CH_3NH_3PbI_3$, has shown the excellent light harvesting ability, high charge-carrier mobility, high conductive (10^{-3} S•cm^{-1}), large exciton diffusion length (over 1 μm) and well-matched energy band level with the commonly used electron transport and hole transport materials.[41] The bandgap of $CH_3NH_3PbI_3$ is around 1.55 eV which are tunable via substitution between halogens. This kind of halide-based tunable optical properties is one of the most advantages of IOP. Moreover, IOP have very unusual open-circuit voltage (V_{oc} = 1 to 1.5 V) which suggests the low thermodynamic loss in the system.[42, 43] The most striking property of IOP is having an ambipolar behavior, which can play as both electron and hole transporter.[44] Moreover, the deposition of layers based on low temperature solution methods such as spin coating, printing, during the fabrication of perovskite solar cells enable a low cost fabrication methods.[45] All these advantages have promoted PSCs becoming a most hot material of study.

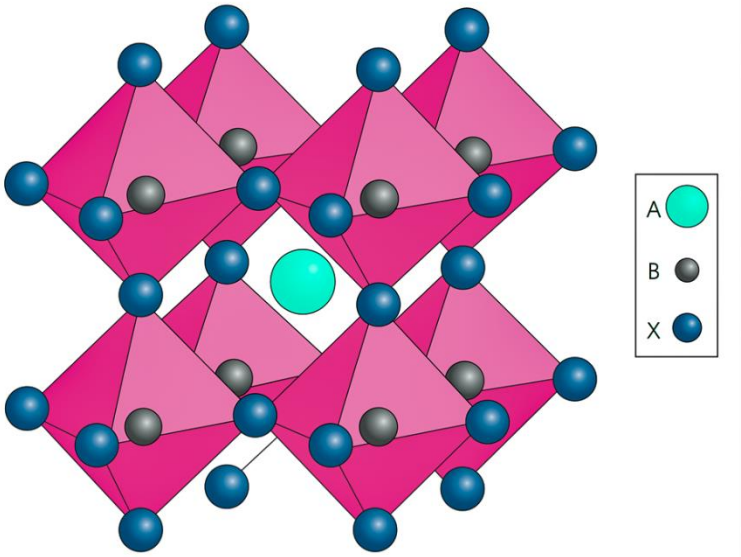

Figure1.14 Conventional 3D perovskite structure of ABX_3.

Device structure

The device structure of PSCs have emerged with various forms at the past decade. The common device structure was given as glass/FTO/TiO_2/$CH_3NH_3PbI_3$/HTM/Ag or Au at the beginning.[40] Later, the device structure was framed with different configurations, namely, planar and mesoporous architectures, as shown in Figure 1.15. In the mesoporous type structure, a porous layer of metal oxide is employed in order to adsorb the perovskites, and this is eliminated in the planar-type structure. Other than these configurations, an Al_2O_3 photoanode-based perovskite solar cell, called meso-superstructured solar cells (MSSCs) also successfully demonstrated. In the porous architecture, for the electron transport layer, other than TiO_2, SnO_2 and ZnO are also employed. It was Kojima et al. in 2009 who fabricated the first perovskite-sensitized solar cell using traditional iodine/tri-iodide redox couple electrolyte with 3.8% efficiency.[28] Due to the limitation and drawbacks with the liquid electrolytes, the scenario of the hole conductor has changed from liquid to solid state. Different hole transport materials (HTMs) such as PEDOT:PSS, P3HT, PCPDTBT, PCDTBT, poly-triarylamine, $CsSnI_3$ and spiro-OMeTAD were studied with $CH_3NH_3PbI_3$ in device performance. Even though spiro-OMeTAD was studied much for HTM, a recent analysis demonstrated using PTAA which function as best HTM with improved efficiency and high-hole mobility (~1×10^{-2} to ~1×10^{-3} cm^2 V^{-1} s^{-1}), high work function

than spiro-OMeTAD.[46] Other than organic HTMs, p-type inorganic semiconductor materials such as CuSCN, PbS, Cu_2O and CuO were also successfully used. Starting the efficiency from 3.8% (2009), about 25.6% (2021) of efficiency has reached so far within a short period in perovskite solar cells.[39] Recently, over 15% efficiency has achieved through the sequential deposition and vapor phase deposition technique which is a remarkable record in the hybrid organic-inorganic solar cell research field.[47] The fundamental working mechanism of perovskite-sensitized solar cell is yet to understand and there are several proposed theories describing about the possible operation. Some possible theories have been proposed to explain the origin of the hysteresis in PSCs, involving ferroelectricity, vacancy-assisted ionic migration, charge carrier trapping, and capacitive effect.[48] in addition, tandem perovskite architecture has also attracted large interest and achieved higher PCE since the first development in 2014.[49]

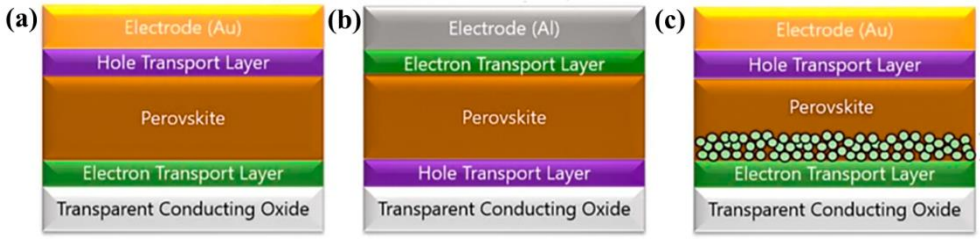

Figure 1.15 Basic device structure of perovskite solar cell with different configuration (a) conventional planar n-i-p structure (b) planar p-i-n (inverted) structure and (c) mesoporous.

Challenges and solutions

Despite the remarkable progress has been made in lead-based halide perovskites solar cells, the issue of lead toxicity still remains and inhibits further development. In recent years, lead-free perovskite solar cell materials have developed which also showing promising efficiencies. Elements such as Sn, Ge Bi and Sb were used to replace Pb, and their performance was also evaluated.[50] In addition, PSCs have problematic stability issues which is strongly affected by water, moisture and UV light. When the humidity is high, it has been found that about 55% of $CH_3NH_3PbI_3$ start to decompose.[51]

The great efforts on optimizing materials modification, device architecture and the method of fabrication of active layer and playing with the electrode modification via active materials have paving the way for future applications. It is expected that future

approaches in fabrication of devices will help to reach the higher efficiency. However, there are many challenges to overcome, including low efficiency of lead-free-PSCs, poor film quality, serious charge carrier recombination, large electron and hole effective mass and wide or indirect bandgap.

Undoubtedly, reliable deposition methods, fabricating high quality stable layers, new material compositions and novel tandem approaches will bring PSCs into new direction in near future.

1.4 Performance parameters of solar cells

The solar cell will generate photovoltage when the cell illuminated.[8] Under dark condition (without light illumination), a standard solar cell behaves similar to a diode, as shown in Figure 1.16, with a different amount of current under forward bias ($V > 0$) respect to reverse bias ($V < 0$). This rectifying behavior is a feature of photovoltaic devices and is a consequence of the asymmetric junction needed to separate charges. Under light illuminating condition, the I(V) characteristic of the diode is shifted by a factor theoretically proportional to the short circuit current. The resulting total current is the superimposing of the photocurrent and the dark current.

The open-circuit voltage, V_{OC}, is the maximum voltage available to be outputted from a solar cell, and this occurs at zero current. The V_{OC} corresponds to the amount of forward bias on the solar cell due to the bias of the solar cell junction with the light-generated current. The current generated by the cell under illumination when the two terminals are connected together with a load resistance R_L=0 is the short circuit current (I_{SC}). With increasing R_L, the cell provides a current I(V) between I_{SC} and 0 with a corresponding voltage between 0 and V_{OC} based on rectification effect of a diode, as shown in Figure 1.16. The behavior of I and V defines the current-voltage characteristic of the cell under a particular illumination. Since the current generated by the cell is proportional to the illuminated area, the short circuit current density (J_{sc}) replaces the I_{SC}, as the current normalized over this area.

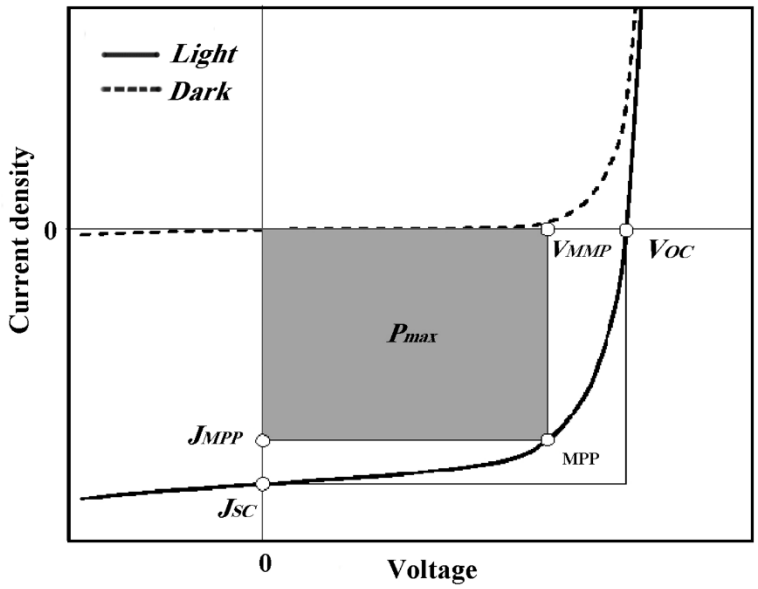

Figure 1.16 Current-voltage characteristic of a solar cell.

The electrical equivalent circuit of solar cells is shown in Figure 1.5, namely, the solar cell is equivalent to a current generator in parallel with a diode. The photocurrent produced is divided between the variable resistance of the diode and the load applied. Without the diode there is no photovoltage and nothing to lead the photocurrent through the load.

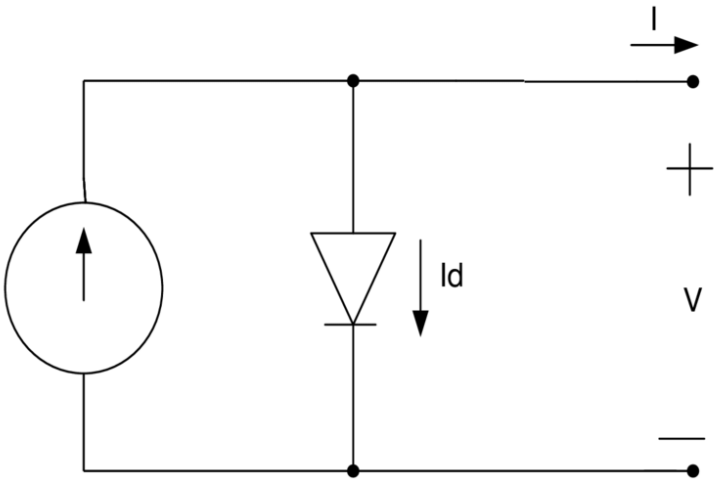

Figure 1.17 Equivalent circuit of an ideal single diode PV Cell.

The working zone of a solar cell is the range of bias from 0 to Voc. Within this

range the cell delivers output power. The power density of the cell is:

$$P = \text{JV} \qquad (1)$$

The maximum value of P is defined as the maximum power point of the cell, which occurs at a voltage V_m with a corresponding current density J_m. The Fill Factor (*FF*) can be defined from J_m and V_m as:

$$FF = \frac{J_{MMP}V_{MMP}}{J_{SC}V_{OC}} \qquad (2)$$

which basically describes the "squareness" of the J-V curve (Figure 1.16). The efficiency η of a cell is the power delivered at the maximum power point as a fraction of the incident light power density P_s:

$$\eta = \frac{J_m V_m}{Ps} \qquad (3)$$

Using the definition of FF in (3):

$$\eta = \frac{J_m V_m FF}{Ps} \qquad (4)$$

The four parameters: J_{SC}, V_m, *FF* and η are the key performance characteristics of a solar cell. These parameters must be defined under standard illumination conditions using the AM1.5 sun spectrum under an incident power density of 1000 W/m^2.

1.5 Factors affecting the performance of solar cells

The factors affecting the performance of solar cells can divide into extrinsic and intrinsic factors. The most important extrinsic factors can attribute to the solar radiation intensity received, such as cloud and other shading effects, module orientation, weather conditions, and geographical location, and the cell temperature, inverter efficiency, cable resistance also are extrinsic factors.[52] In this section, I will focus on the some intrinsic factors affecting the performance of solar cells from the following aspects.

Light absorber materials: As illustrated in the section of "semiconductors for solar cells", photons with energies below the bandgap are not absorbed, namely cannot generated photocurrent. The photons with energies above the bandgap are absorbed, but their energies are not fully converted to electrical energy because of thermalization of

charge carriers. The maximum PCE of a solar cell is dependent on the bandgap of the light absorber used in the solar cell, which can be evaluated according to the Shockley-Queisser detailed-balance model. Figure 1.18 shows the evaluated PCE results (S-Q limit) as the function of the bandgap for a single-junction solar cell under "one-sun" illumination with the standard AM1.5 solar spectrum. This maximum PCE corresponds to a solar cell with the maximum V_{oc}, J_{sc}, and FF, where maximum V_{oc}=bandgap, maximum J_{sc}=100% quantum efficiency for the photons with larger energy than the bandgap, and maximum FF=100%.[53]

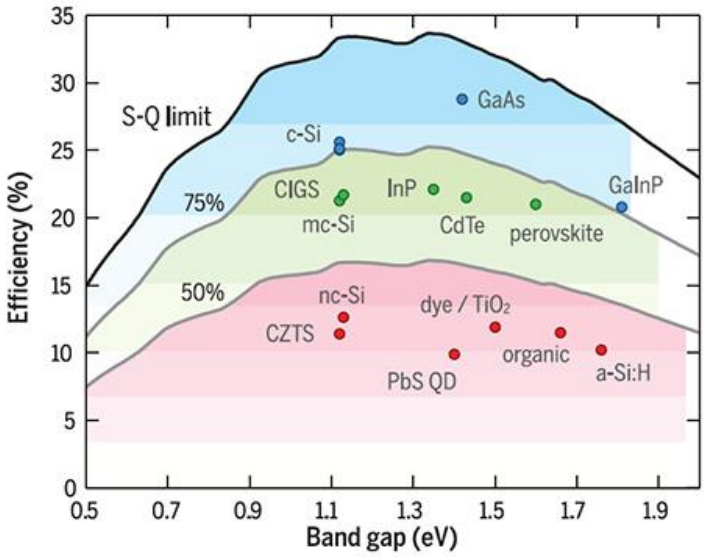

Figure 1.18 Theoretical Shockley-Queisser detailed-balance efficiency limit as a function of bandgap (black line) and 75% and 50% of the limit (gray lines). The record efficiencies for different materials are plotted for the corresponding bandgaps. Reproduced with permission.[53] Copyright AAAS.

The maximum PCE occurs for a light absorber with a bandgap of 1.34 eV and is 33.7%.[14] Scientists put more efforts into finding materials which possess a closest bandgap to the optimum, or altering the bandgap by bandgap engineering, namely, controlling the composition of the light absorbers, such as GaAlAs, InGaAs, and $CH_3NH_3PbI_xCl_{3-x}$. Figure 1.18 shows also the maximum PCEs as the function of bandgap under 75% and 45% incident spectrum power conditions, and the record PCEs

for various light absorbers.

Morphology of light absorber layer: Morphology of the light absorber layers, which depends on the fabrication process and conditions as well as characteristics of the light absorber materials, dramatically influences the performance of solar cells by reason of their distinctive features consisting of efficient carrier separation, decoupling directions of light absorption and charge-carrier collection as well as direction of charge carriers transport.[54] Generally speaking, the crystal morphology control can be achieved by morphology engineering, including additives engineering, solvent engineering, humidity control, compositional engineering, thermal engineering, self-assembled monolayers and interface engineering.[55] Saliba et al. used inorganic cesium as an additive to make highly stable PSC devices with a power output of 21.1%.[56] Shiu et al. adopted well-aligned silicon nanowire for poly heterojunction solar cells through solution process, this nanowire structure increases the area of heterojunctions and shortens the carriers diffusion distance, and therefore, it greatly increases carriers collection efficiency.[57]

Thickness of light absorber layer: It is known that the thickness of the light absorber layer is one of the most importance factors for solar cells.[58] Thus optimization of photoactive layer thickness is often the first step when optimizing solar cell performance. When a thin light absorber layer is used in the device, it cannot absorb all incident light, resulting low a photocurrent, while its low resistance results a high carrier extraction efficiency. For a thick light absorber layer, although more carriers can be generated by increasing incident light absorption in the device, lower carrier extraction efficiency due to carriers recombination at higher resistance affects mainly FF and V_{oc}.[59] Experimentally, photoactive layer thickness can be readily tuned over a broad range in various solar cells, typically locates in 200 nm to 1 mm. Perovskite layer thickness is important for high performing PSCs and there is no advantage of using perovskite layer with thickness <200 nm or >700 nm in the device.[59] However, the optimum thickness for crystalline silicon is calculated to be about 100 μm.[58]

The optimum thickness for direction semiconductors will thinner than that of indirect semiconductors due to the larger light absorption coefficient for the direct

semiconductors. On the other hand, the optimization of light absorber layer thickness needs to balance the other layers in the device. The optimum light absorber layer thickness is the competition result between carriers generation and carriers extraction and transport.[60]

Energy level alignment: In photovoltaic devices, charges extraction and transport are strongly dependent on the energy level alignment at the interfaces.[61] Typically, the solar cells architecture consists of several layers, so there are some interfaces between the different layers. The energy offsets at interfaces determine the moving directions of the charge carriers. The excited electrons transfer from the CB of a layer with higher energy level to the CB of another layer with lower energy level through their interface, while photo-generated holes transfer from the VB of a layer with lower energy level to the VB of another layer with higher energy level through their interface, if there is not drastic barrier at the interface. To extract charge carriers from the device, namely, electrons and holes transfer to cathode and anode, respectively, a suitable energy level alignment for the all layers used in the device is necessary. The optimization of the energy level alignment, namely the energy level matching in the cell architecture, is significant to enhance the V_{oc} of solar cells.

1.6 Bi-VI-VII-type semiconductors

Bi-VI-VII-type semiconductors (where VI = O, S, Se, Te and VII = Cl, Br ,I) evoke great interest owing to their variety of physical properties, such as high photoconductivity, photoelectricity, ferroelectricity, piezoelectricity, electromechanical effect, electrooptical effect, and temperature dependence of bandgap.[62, 63] They have high potential application as optoelectronic materials because of the Bi(III) contains a fully occupied $6s^2$ electron configuration. As shown in Figure 1.19, in Bi-VI-VII-type semiconductors, Bi(III) has an electron configuration of $6s^2$, the fully occupied Bi(III) $6s^2$ orbital hybridizes with the fully occupied np orbital of X^-, enabling a dispersive

valence band. The conduction band is dominated by the spatially extended empty 6p orbitals of B(III), which hybridize with the fully occupied np orbital of X anion of the valence band, giving a significant cross-bandgap hybridization in Bi-VI-VII semiconductors. This will lead to a mixed ionic-covalent character, which is known to enhance lattice polarization significantly.[64-66] Therefore, a B(III) compound with $6s^2$ electron configuration often has dispersive valence and conduction bands and a large static dielectric constant. The strong screening of charged defects and impurities reduces the rates of carrier scattering and trapping. These electronic and dielectric properties are favorable for efficient carrier transport.[67]

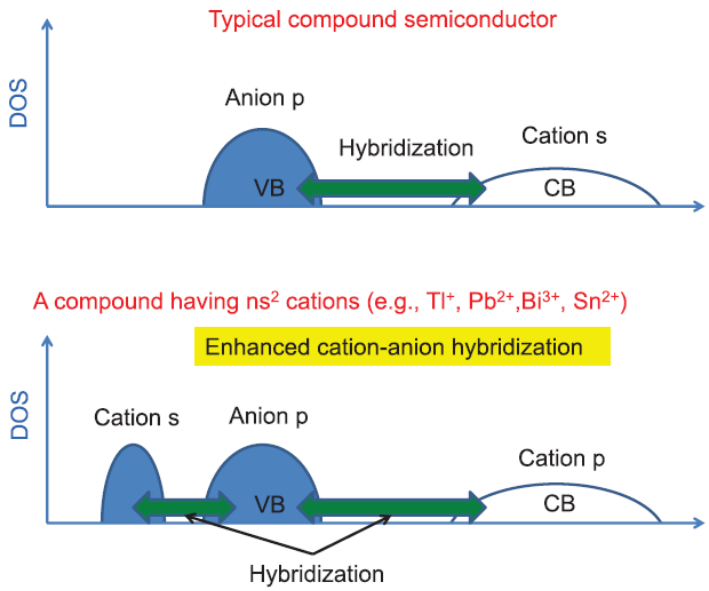

Figure 1.19 Density of states for a typical compound semiconductor and a compound having cations with ns^2 orbital. Reproduced with permission.[67] Copyright APS physics.

Some efforts have been made to prepare Bi-VI-VII-type semiconductors. Traditionally, Bridgeman-Stockbarger technique or vapor phase growth have been used to prepare their single crystals, which need long time and complex equipment.[63, 68-70] In recent years, solvothermal and hydrothermal methods have been widely adopted to synthesize their nanocrystals; ensuring them can be extensively applied on various areas, such as photocatalytic, photovoltaic.[71-74] In addition, A variety of morphologies of Bi-

VI-VII-type semiconductors endow unique superiorities in applications. In this section, the most representative Bi-VI-VII-type semiconductors, Bi-O-X, Bi-Se-X, and Bi-S-X (X = Cl, Br, and I) are reviewed from their crystal structures, photoelectric properties, and applications.

1.6.1 Crystal structures

Bismuth oxyhalides (BiOX; X = Cl, Br, I) have layered structures, as shown in Figure 1.20 (a). The BiOX structure is composed of $[Bi_2O_2]$ slabs interleaved with double halogen atom slabs along the c-axis direction.[75] However, as a category of Bi-VI-VII-type semiconductors, Bi(Se/S)X (X = Cl, Br, I) possess different crystal structure from BiOX. As shown in Figure 1.20 (b) and (c), Bi(Se/S)X structure consist of $[(Bi(Se/S)X)_2]_\infty$ ribbons which growths along the b axis, where each Bi atom is six-coordinated with three X atoms and three Se/S atoms. Two of the Se/S atoms and two X atoms form a parallelogram parallel to *b* axis, with the remaining atoms occupying the apices of the pyramids formed on either side of this parallelogram.

$Bi_{13}S_{18}X_2$ (X = Cl, Br, I) is also an important Bi-VI-VII-type semiconductor. However, there are some debates on their structures and chemical compositions. Miehe et al. reported first study on $Bi_{13}S_{18}I_2$ compound and concluded that it belongs to the hexagonal crystal system with the space group of $P6_3$ and a chemical formula of $Bi(Bi_2S_3)_9I_3$.[76] Other studies reported that $Bi_{13}S_{18}I_2$ compound belongs to the hexagonal system with space group of $P6_3/m$ or $P6_3$ and a chemical formula of $Bi_{19}S_{27}I_3$ or $(Bi(Bi_2S_3)_9I_3)_{2/3}$.[77-79] Recently, Groom et al. rediscovered the $Bi_{13}S_{18}I_2$ structure by single crystal XRD and powder synchrotron XRD, resulting in a stoichiometry of $Bi_{13}S_{18}I_2$ with space group of P3 due to formation of bivalent Bi(II) dimer of (Bi_2^{4+}) in this compound.[80] In this structure, ribbon-like subunits of $[Bi_4S_6]$ form six spokes around a central hexagonal channel at the corners of the unite cell. The $[Bi_4S_6]$-ribbons spokes are connected together to form a triangular tunnel structure in the direction of c-axial, where I^- located in the tunnel site of the $Bi_{13}S_{18}I_2$ structure, as shown in Figure 1.20 (d). Lesser reported studies on $Bi_{19}S_{27}Br_3$ and $Bi_{19}S_{27}Cl_3$ compounds belonged to

the hexagonal crystal system with the $P6_3$ space group, where all Bi are trivalence. (Ref.???) We think these compounds will adopt chemical composition of $Bi_{13}S_{18}X_2$ (X=Br, Cl) and hexagonal structure with space group of P3 same as $Bi_{13}S_{18}I_2$ than that $Bi_{19}S_{27}X_3$ (X=Br, Cl) because formation of Bi(II) dimer of Bi_2^{4+} is also possible in these compounds.

In view of their inherent structures, BiOX tend to form a plate-like particle morphology, while Bi(Se/S)X and $Bi_{13}S_{18}X_2$ tend to form a rod-like particle morphology.

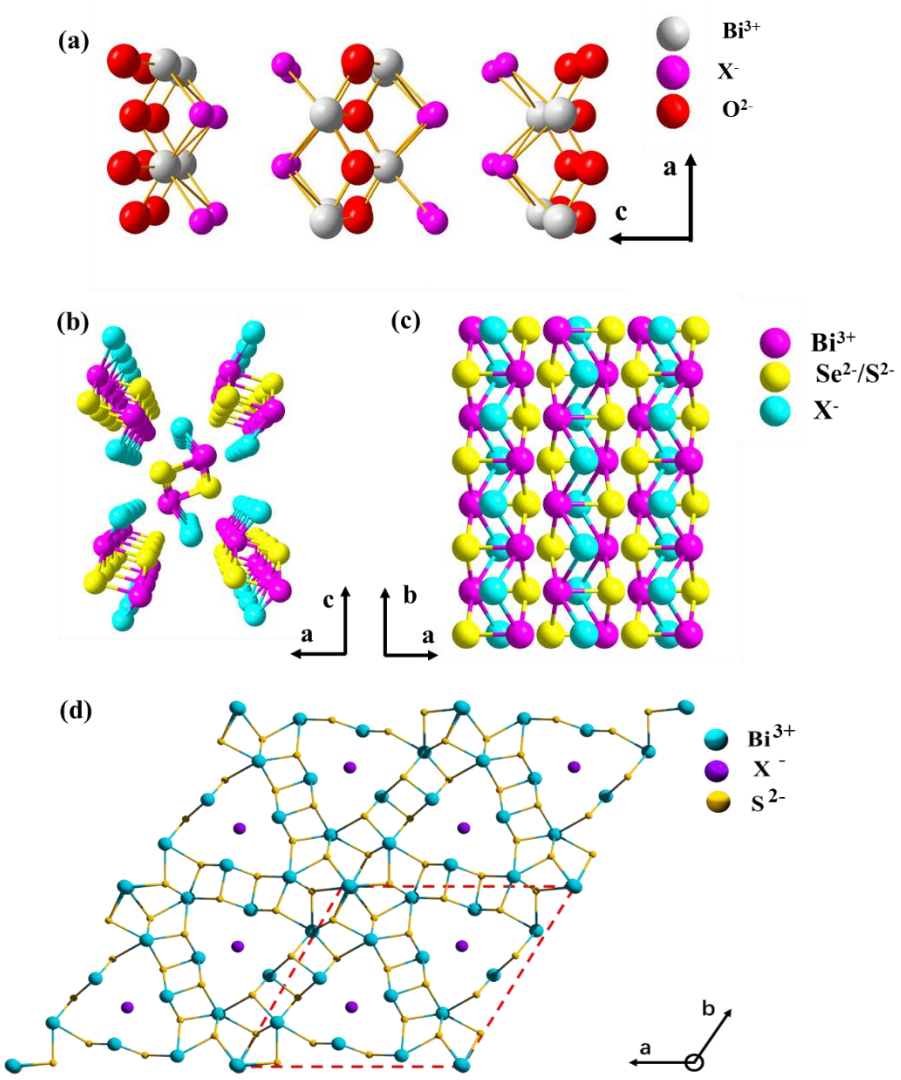

Figure 1.20 The crystal structures of (a) BiOX, (b) three-dimensional view and (c) view along c axis of BiSeX, and (d) $Bi_{13}S_{18}I_2$.

1.6.2 Photoelectric properties

Bi-VI-VII-type compounds contain $6s^2$ electrons similar to Pb(II) in $CH_3NH_3PbX_3$, which has been proved benefited carriers transport efficiency.[67] Heavy post-transition metal of Bi possesses the soft polarizability, which can cause a large dielectric constant and efficient screening of charged defects. Therefore, bismuth oxyhalides and bismuth chalcohalides are expected to possess comparable photoelectric properties with $CH_3NH_3PbX_3$.

The bismuth oxyhalides demonstrate excellent optical, electrical, and photoelectrical properties.[75, 81, 82] BiOX (X = Cl, Br, I) exhibits promising applications in photovoltaics as well as gas sensors, and also in pharmaceuticals, pigments, catalysts.[83-85] In addition, a strong internal electric field is built between X and $[Bi_2O_2]$ layer in the layered BiOX structure, which can reduce the recombination rate of carriers.[86] BiOX are indirect semiconductors.[87] The bandgap of BiOCl has been determined experimentally to be about 3.2 eV located in the ultraviolet light range, and the bandgaps of BiOBr and BiOI were evaluated from their absorption spectra to be about 2.6 and 1.8 eV, respectively, located in the visible-light range.[88] It is noted that with increasing atomic number of halogen, the bandgap of BiOX decreases in an order of BiOCl (~3.2 eV) > BiOBr (~2.7 eV) > BiOI (~1.8 eV). Considering their similar structures and atomic arrangements, solid solutions of $BiO(Cl_xBr_yI_z)$ (where $x+y+z=1$) could be allowed, which can be applied to enhance their photocatalytic activities by control of the bandgap in a range to from UV to visible-light (Figure 1.21).[89] Up to now, the solid solutions of $BiOCl_{1-x}I_x$, $BiOCl_{1-x}Br_x$, and $BiOBr_{1-x}I_x$ have been synthesized by various methods.[72, 73, 90]

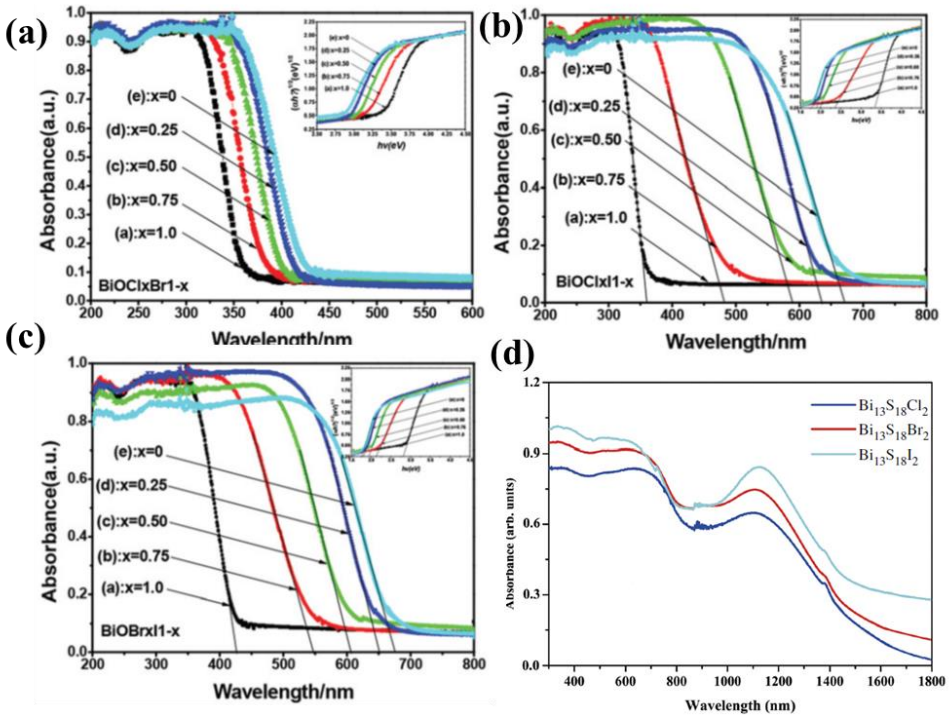

Figure 1.21 UV-Vis absorption spectra of (a) $BiOCl_xBr_{1-x}$, (b) $BiOCl_xI_{1-x}$, (c) $BiOBr_xI_{1-x}$, and (d) UV-Vis-NIR absorption spectra of $Bi_{13}S_{18}X_2$, respectively. Reproduced with permission.[91] Copyright RSC Publishing.

Some other bismuth oxyhalides have been reported also, but received less attention. Oxygen-rich bismuth oxyhalides of $Bi_{12}O_{17}Cl_2$ (Eg = 2.57 eV) and $Bi_{24}O_{31}Cl_{10}$ (Eg = 2.71) possess narrower bandgaps than BiOCl (E_g = 3.2 eV). Moreover, Cl-rich and Br-rich bismuth oxyhalides such as $Bi_{12}O_{15}Cl_{l6}$ (E_g = 2.36 eV) and $Bi_4O_5Br_2$ (E_g = 2.37 eV), also possess narrower bandgap than BiOCl and BiOBr. These compounds showed higher visible light response photocatalytic activities than the correspond bismuth oxyhalides of BiOX.[92]

Bismuth chalcohalides of BiSX and BiSeX (X = Cl, Br, I) are considered to be the most potential useful optical, electric and optoelectronic materials and thus attracted more attention in recent years.[93-95] BiSX are n-type semiconductors. Both of BiSCl and BiSBr are direct semiconductors with almost same bandgaps of 1.93 and 1.95eV, respectively.[96, 97] However, BiSI is an indirect semiconductor with a bandgap of 1.57 eV.[98] Up to now, the reasons of the difference between BiSX (X = Cl, Br) and BiSI are still unclear. BiSI have been extensively investigated as light absorbers for photovoltaic solar cells, photocatalysts, photoconductor and ferroelectrics. But limited studies about

BiSCl and BiSBr mainly focused on theoretical calculation, because they are not easy to be obtained. Ran et al. calculated the electronic structure and suggested that BiSBr may be promising as light absorber for solar cells.[95]

The band structures of BiSeX are similar to those of BiSX, except that the BiSeX have smaller bandgaps and do not show ferroelectric properties.[99] The bandgaps of BiSeX are controllable from 1.69 for BiSeCl to 1.3 eV for BiSeI. Up to now, most of studies on BiSeX are only limited in the theoretical calculation using density functional theory because they are not easy to be synthesized. Density functional calculations suggest they are suitable for optoelectronic applications and light absorber materials for solar cells. For example, Shi et al. studied BiSeBr based on calculation, and suggested that BiSeBr is a suitable material as photovoltaic and radiation detection materials.[67] In addition, anion vacancies in BiSeBr are shallow, which is helpful to efficient electron transport.[94] M. Ganose et al. predicted that BiSI and BiSeI have limited maximum PCE of 22.5, and 25% by theoretical calculations., respectively, which is competitive with $CH_3NH_3PbI_3$ perovskite for PSCs.[100] BiSeX also have high potential for radiation detection materials.[95] However, it is necessary to prove these theoretical predictions by the experimental approaches.

$Bi_{13}S_{18}X_2$ (X = Cl, Br, I) attract an increasing attention in recent years. Interestingly, the bandgaps of $Bi_{13}S_{18}X_2$ demonstrate an uncommon composition-independent bandgaps, which may be due to the minor contributions of the halogens to the valence band maximum and conduction band minimum.[101] The strong light absorbance over a wide wavelength range from UV to NIR suggests a great potential application of $Bi_{13}S_{18}X_2$ in optoelectronic devices.

1.6.3 Applications

In recent years, most of studies on Bi-VI-VII-type semiconductors focus on photocatalytic applications for solar energy utilization and environmental purification because of their optical properties, high chemical stabilities, non-toxicity and low

cost.[92] The wide bandgap Bi-VI-VII-type semiconductors, such as BiOCl, BiOBr, BiSeBr and BiSeCl, which can absorb ultraviolet light, exhibit the high UV light response photocatalytic activities.[102-104] In order to enhanced the photocatalytic activity and extending spectral response, many techniques have been adopted, such as component adjustment, morphology engineering, and heterojunction construction.[104-106]

Component adjustment, including doping, and solid solution preparation, is an efficient way to tune the band structure parameters, such as VB, CB and bandgaps. It has been reported that doping or co-doping of elements such as Co, Fe, La, Zn, C or S forms impurity energy levels in BiOCl band structure, causing the redshift of absorption edge. Br- and I-dopings are effect for the redshift of absorption edge of BiOCl because BiOCl, BiOBr, and BiOI have similar structure and atomic arrangement.[73] The redshift of absorption edge can be used to improve visible light response photocatalytic activities of BiOCl wide bandgap semiconductor. For instance, Liu et al. synthesized BiOCl nanoplates with different I-doping concentrations by hydrothermal method and investigated the degradation performance of rhodamine B and tetracycline hydrochloride under visible light. The results show that I-doping not only redshifts the light absorption range of BiOCl nanoplates, but also enhances the separation ability of photogenerated charges.[107]

Morphology engineering is also an efficient approach to dramatically enhance the photocatalytic activity by increasing surface area and exposing active and effective facet on crystal surface.[108] BiOX with various crystal morphologies, such nanofibers, nanosheets, micro-flowers, lamellas, and hierarchical architectures were prepared to improve the photocatalytic activity for degrading different organic pollutants. Jia et al synthesized flower-like hierarchical BiOBr and found that rhodamine B and colorless salicylic acid were effectively degraded on its surface by photocatalytic reaction.[109] Lei et al. successfully synthesized flower-like BiOI hierarchical structures at room temperature, which showed high photocatalytic activity for Rhodamine B degradation.[110] Single-crystalline $Bi_{13}S_{18}Cl_2$ nanorods via a solvothermal route exhibited high photocatalytic activity for reduction of Cr(VI).[111] Deng et al. developed

a hydrothermal processes to form fabric-like $Bi_{13}S_{18}Br_2$, which shows enhanced visible light response photodegradation of Rhodamine B.[112]

Heterojunction construction is a significant approach to improve the performance of photocatalysts, because the photo-excited electrons and holes can be efficiently separated by the heterojunction.[92] For the most Bi-VI-VII-based photocatalysts, heterojunction construction has been widely applied to reduce the recombination of excited electrons with holes. A lot of BiOBr nanocomposite photocatalysts with p-n junction have been constructed. Jiang et al. constructed BiOBr with nitrogen doped graphene to form a p-n junction, which accelerated charge transfer rates to enhance photoelectrochemical performance.[113] The p-n junction photocatalysts of $BiOBr/Bi_2WO_6$, $BiOBr/C_3N_4$, $BiOBr/Bi_{24}O_{31}Br_{10}$, and $BiOBr/ZnFe_2O_4$ and so on have been also developed.[81, 86] Zhou et al. constructed an n-p-n double heterojunction photocatalyst of $BiSI/MoS_2/CdS$ for photocatalytic hydrogen evolution. The built-in electric field between the BiSI nanorod and MoS_2 interlayer enhances carriers transport efficiency, which resulted in a 46 times increased hydrogen production efficiency.[114] Zhang et al. prepared a double Z-scheme photocatalyst of $BiSI/Bi_2WO_6/g\text{-}C_3N_4$ by hydrothermal reaction. This photocatalyst showed high photocatalytic activity to degradation of rhodamine B, chlortetracycline and tetracycline.[115] In addition, two or three strategies were adopted at the same time to achieve high photochemical performance. Wu et al. reported cactus-like $MoS_2/Bi_{13}S_{18}Cl_2$ heterostructures for efficient photocatalytic hydrogen evolution, where the cactus-like structure enables the heterostructures with highly enhanced light absorption and charge separation. All these studies suggest that heterojunction construction shows an obviously enhanced photocatalytic performance than the individual compounds.

Besides photocatalytic applications, some of Bi-VI-VII-type semiconductors were applied to light absorbers for solar cells, such as BiOI and BiSI.[82, 116] The results suggest that the some of Bi-VI-VII-type semiconductors are potential candidates as the light absorbers for solar cells because of their strong visible light absorption and the suitable bandgaps. Zhang et al. prepared BiOI nanoflake array film on FTO glass as light absorber layer for solar cells in 2010. And the BiOI-based nanoflake array solar cell

showed photovoltaic performance with a PCE of 0.092%.[117] Then, Hahn et al. have reported fabrication of BiOI nanoplatelet photoelectrodes on FTO glass using spray pyrolysis process for solar cells. The optimized BiOI film with thickness of 1 μm exhibited a high incident photon conversion efficiencies above 20%.[118] Sfaelou et al. fabricated a BiOI-based solar cell using BiOI nanoflakes as light absorber on porous TiO_2 film, a Pt/FTO as cathode and I_3^-/I^- redox electrolyte as HTM. The PCE of the solar cell was 1.03%, proving the high potential of BiOI as light absorber for solar cells.[119] These results suggest the high promising photovoltaic application of BiOI and left a lot of ground for further improvement.

Hahn et al. reported the first study on the BiSI-based solar cells using a polycrystalline BiSI film fabricated by a chemical spray pyrolysis technique on FTO glass substrate; this BiSI-based solar cells showed a PCE of 0.25.[120] The poor photovoltaic behavior should be related to the misalignment of band energy level and the present of impurities phase.[6, 121] Xiong et al. fabricated single phase of BiSI nanorod array film on a tungsten substrate as light absorber layer; its solar cell generated a PCE of 0.66% with a high fill factor of 52.81%.[122] Tiwari and co-worker developed a single-precursor solution approach to fabricated a compact and homogeneous flake-shaped BiSI film; its solar cells with a architecture, glass/FTO/SnO_2/BiSI/F8/Au, show the champion PCE of 1.32% for the BiSI-based solar cells.[121] This PCE value is still much lower that the theoretical PCE value of 22.5% for the BiSI-based solar cells.

In addition, some other applications for Bi-VI-VII compounds were also investigated. $Bi_{13}S_{18}I_2$ film were fabricated as supercapacitor electrode and photodetector, proving its promising potential application in optoelectronic devices.[78, 101, 123] It was reported that doped BiSeCl can exhibit Gunn effect that has potential application for microwave oscillators.[94]

Above the discussions, considerable studies on Bi-VI-VII-type semiconductors mainly focus on their photocatalytic performances. The studies on solar cells are limited in BiOI and BiSI, although other Bi-VI-VII-type semiconductors also have potential possibility as light absorbers for solar cells. The applications on other areas are still very limited due to less studies on the development of synthesis techniques for Bi-VI-

VII-type semiconductors. Therefore, some works of Bi-VI-VII-type semiconductors are still at the theoretical level. The studies on Bi-VI-VII-type semiconductors are still in the early stages, and many challenges are necessary, such as the synthesis of BiSeX, BiSCl, and BiSBr, characterization and the photovoltaic evaluation of $Bi_{13}S_{18}X_2$, BiSX, BiSeX.

1.7 Purpose of the present study

As described above, Bi-VI-VII-type compounds exhibit a wide variety of interesting physical properties. Some bismuth chalcohalides have been extensively studied, mainly on their facile synthesis and photocatalytic performances. Some studies on BiSI- and BiOI-based solar cells have been carried out and results reveal their possibilities as light absorber for solar cells. However, only limited studies on $Bi_{13}S_{18}X_2$ and BiSX because these compounds are difficult to be prepared by a facile process, which limited to deeply understand these materials. For example, there are some debates about the crystal structure and bandgap energy on $Bi_{13}S_{18}X_2$. In addition, their films are difficult to be fabricated using the traditional synthesis methods such as vapor-transport and flux process. Their photoelectric behavior and photovoltaic performance are still almost unclear. The fundamental studies focused on bismuth chalcohalides will be beneficial to further understand their photoelectric, photovoltaic, and photocatalytic behaviors, and also to explore their applications in these areas.

In the present dissertation, some facile solvothermal processes were developed for the synthesis of a series of bismuth chalcohalides, including $Bi_{13}S_{18}Cl_2$, $Bi_{13}S_{18}Br_2$, $Bi_{13}S_{18}I_2$, BiSCl and BiSI. The photoelectric behavior as well as structures of these bismuth chalcohalides were systemically studied. Furthermore, the solar cells based on these bismuth chalcohalides as light absorbers were fabricated via some modified solvothermal and physical vapor deposition (PVD) processes to investigate their photovoltaic performances. The results suggest that the bismuth chalcohalides are promising materials as a new type of light absorber material for solar cells.

In Chapter II, the syntheses and formation reactions of $Bi_{13}S_{18}I_2$ and BiSI under solvothermal conditions, photoelectric study on these bismuth chalcohalides as well as $Bi_{13}S_{18}I_2$-based solar cell performance are mentioned. The formations of $Bi_{13}S_{18}I_2$ and BiSI are strongly dependent on the S/Bi mole ratio, reaction temperature, and solvent in the reaction system. The photoelectric study results revealed that $Bi_{13}S_{18}I_2$ is an n-type semiconductor with a narrow bandgap of 0.75 eV, and possesses a strong light absorbance from UV to NIR, suggesting the promising light absorber material for solar cells. Moreover, for the photovoltaic study of $Bi_{13}S_{18}I_2$, a modified solvothermal process was developed to fabricate a uniform $Bi_{13}S_{18}I_2$ film on the porous TiO_2 electrode. The preliminary photovoltaic results demonstrated a PCE of 0.85% of the $Bi_{13}S_{18}I_2$-based solar cells for the first time. The results suggest a potential possibility for the fabrication of solar cells using $Bi_{13}S_{18}I_2$ based on a low-cost solution process.

In chapter III, the studies are carry out on synthesis, photoelectric properties, and photovoltaic performances of $Bi_{13}S_{18}X_2$ (X = Cl, Br, I) compounds as light absorber for solar cells. The chemical composition of $(Bi^{3+})_{12}(B_2^{4+})_{0.5}(S^{2-})_{18}(X^-)_2$ and the triangular tunnel structure were determined by Rietveld refinements. In addition, $Bi_{13}S_{18}X_2$ films fabricated by a facile PVD approach were applied to solar cells as the light absorbers, which demonstrated PCEs of 0.91, 1.12 and 0.75% for $Bi_{13}S_{18}X_2$ (X = Cl, Br, I), respectively. The results suggest that the $Bi_{13}S_{18}Br_2$ is the most promising light absorber in $Bi_{13}S_{18}X_2$ (X = Cl, Br, I) compounds for this new type of solar cell.

In chapter IV, synthesize single crystalline BiSCl nanofibers and photoelectric behavior as a light absorber for solar cells are described. BiSCl is an n-type semiconductor with a direct bandgap of 1.96 eV, where valence band maximum (VBM) and conduction band minimum (CBM) located at 6.04 and 4.08 eV below the vacuum level, respectively. Uniform BiSCl-nanorod array films were fabricated on porous TiO_2 electrode by a modified solvothermal process, where the BiSCl nanorod array is vertically oriented to the TiO_2 electrode surface. A proper band alignment of BiSCl-based solar cells with an architecture of FTO/TiO_2/BiSCl/(I_3^-/I^-)/Pt gave a power conversion efficiency (PCE) of 1.36% and a relatively larger short-circuit photocurrent density (J_{SC}) of 9.87 mA/cm^2 for the first time. The preliminary photovoltaic study

result revealed a potential possibility of BiSCl-nanorod array as a light absorber for solar cells which can be fabricated by the low-cost solution process.

In chapter V, a summary of the present study is given. The contribution of this work to future study on bismuth chalcohalides and their applications to photoelectric and photovoltaic devises are mentioned.

1.8 References

1. Peter, L. M., Towards sustainable photovoltaics: the search for new materials. *Philos Trans A Math Phys Eng Sci* **2011,** *369* (1942), 1840-56.
2. Hermann, W., Quantifying global exergy resources. *Energy* **2006,** *31* (12), 1685-1702.
3. Loschi, H. J.; Iano, Y.; León, J.; Moretti, A.; Conte, F. D.; Braga, H., A Review on Photovoltaic Systems: Mechanisms and Methods for Irradiation Tracking and Prediction. *Smart Grid and Renewable Energy* **2015,** *06* (07), 187-208.
4. Fraas, L. M., History of Solar Cell Development. **2014**, 1-12.
5. Green, M. A.; Dunlop, E. D.; Hohl-Ebinger, J.; Yoshita, M.; Kopidakis, N.; Ho-Baillie, A. W. Y., Solar cell efficiency tables (Version 55). *Progress in Photovoltaics: Research and Applications* **2019,** *28* (1), 3-15.
6. Ganose, A. M.; Butler, K. T.; Walsh, A.; Scanlon, D. O., Relativistic electronic structure and band alignment of BiSI and BiSeI: candidate photovoltaic materials. *Journal of Materials Chemistry A* **2016,** *4* (6), 2060-2068.
7. Slikkerveer, A.; de Wolff, F. A., Pharmacokinetics and toxicity of bismuth compounds. *Med Toxicol Adverse Drug Exp* **1989,** *4* (5), 303-23.
8. Gray, J. L., The Physics of the Solar Cell. **2005**, 61-112.
9. Leising, G., Recombination in semiconductors. ByPeter T. Landsberg, Cambridge University Press, Cambridge 1991, 595 pp., hardcover, £ 95, ISBN 0-521-36122-2. *Advanced Materials* **1993,** *5* (1), 67-67.
10. Brennan, K. F., Generation and Recombination Processes In Semiconductors. *Cambridge University Press* **1999,** *pp 489-543*, 489-543.
11. Yuan, L.-D.; Deng, H.-X.; Li, S.-S.; Wei, S.-H.; Luo, J.-W., Unified theory of direct or indirect band-gap nature of conventional semiconductors. *Physical Review B* **2018,** *98* (24).
12. Davis, E. A.; Mott, N. F., Conduction in non-crystalline systems V. Conductivity, optical absorption and photoconductivity in amorphous semiconductors. *Philosophical Magazine* **1970,** *22* (179), 0903-0922.

13. Cartlidge, E., Bright outlook for solar cells. *Physics World* **2007,** *20* (7), 20-24.
14. Shockley, W.; Queisser, H. J., Detailed Balance Limit of Efficiency of p-n Junction Solar Cells. *Journal of Applied Physics* **1961,** *32* (3), 510-519.
15. NREL, Best-Research-Cell-Efficiencies. *https://www.nrel.gov/pv/cell-efficiency.html* **2020**.
16. Kulkarni, M. S., A Selective Review of the Quantification of Defect Dynamics in Growing Czochralski Silicon Crystals†. *Industrial & Engineering Chemistry Research* **2005,** *44* (16), 6246-6263.
17. Timilsina, G. R.; Kurdgelashvili, L.; Narbel, P. A., Solar energy: Markets, economics and policies. *Renewable and Sustainable Energy Reviews* **2012,** *16* (1), 449-465.
18. Khatri, R.; Goyal, R.; Sharma, R. K., Advances in the developments of solar cooker for sustainable development: A comprehensive review. *Renewable and Sustainable Energy Reviews* **2021,** *145*, 111166.
19. Gaspar, G. M. M.; Autruffe, A.; Pó, J. M., Silicon Growth Technologies for PV Applications. **2017**.
20. H, V., A detailed review on Si, GaAs, and CIGS/CdTe based solar cells and efficiency comparison. *PrzeglĄd Elektrotechniczny* **2020,** *1* (12), 11-20.
21. Muteri, V.; Cellura, M.; Curto, D.; Franzitta, V.; Longo, S.; Mistretta, M.; Parisi, M. L., Review on Life Cycle Assessment of Solar Photovoltaic Panels. *Energies* **2020,** *13* (1), 252.
22. Ginovker, A. S.; Gritsenko, V. A.; Sinitsa, S. P., Two-band conduction of amorphous silicon nitride. *Physica Status Solidi (a)* **1974,** *26* (2), 489-495.
23. Basol, B. M.; McCandless, B., Brief review of cadmium telluride-based photovoltaic technologies. *Journal of Photonics for Energy* **2014,** *4* (1), 040996.
24. Powalla, M.; Paetel, S.; Hariskos, D.; Wuerz, R.; Kessler, F.; Lechner, P.; Wischmann, W.; Friedlmeier, T. M., Advances in Cost-Efficient Thin-Film Photovoltaics Based on Cu(In,Ga)Se 2. *Engineering* **2017,** *3* (4), 445-451.
25. Beard, M. C.; Luther, J. M.; Nozik, A. J., The promise and challenge of nanostructured solar cells. *Nat Nanotechnol* **2014,** *9* (12), 951-4.

26. Ananthakumar, S.; Kumar, J. R.; Babu, S. M., Third-Generation Solar Cells: Concept, Materials and Performance - An Overview. **2019,** *23*, 305-339.
27. Li, Y.; Xu, G.; Cui, C.; Li, Y., Flexible and Semitransparent Organic Solar Cells. *Advanced Energy Materials* **2018,** *8* (7), 1701791.
28. Kojima, A.; Teshima, K.; Shirai, Y.; Miyasaka, T., Organometal halide perovskites as visible-light sensitizers for photovoltaic cells. *J Am Chem Soc* **2009,** *131* (17), 6050-1.
29. O'Regan, B.; Grätzel, M., A low-cost, high-efficiency solar cell based on dye-sensitized colloidal TiO2 films. *Nature* **1991,** *353* (6346), 737-740.
30. Cole, J. M.; Gong, Y.; McCree-Grey, J.; Evans, P. J.; Holt, S. A., Modulation of N3 and N719 dye···TiO2 Interfacial Structures in Dye-Sensitized Solar Cells As Influenced by Dye Counter Ions, Dye Deprotonation Levels, and Sensitizing Solvent. *ACS Applied Energy Materials* **2018,** *1* (6), 2821-2831.
31. Wu, K. L.; Ho, S. T.; Chou, C. C.; Chang, Y. C.; Pan, H. A.; Chi, Y.; Chou, P. T., Engineering of osmium(II)-based light absorbers for dye-sensitized solar cells. *Angew Chem Int Ed Engl* **2012,** *51* (23), 5642-6.
32. Błaszczyk, A., Strategies to improve the performance of metal-free dye-sensitized solar cells. *Dyes and Pigments* **2018,** *149*, 707-718.
33. Wu, J.; Lan, Z.; Lin, J.; Huang, M.; Huang, Y.; Fan, L.; Luo, G., Electrolytes in dye-sensitized solar cells. *Chem Rev* **2015,** *115* (5), 2136-73.
34. Theerthagiri, J.; Senthil, A. R.; Madhavan, J.; Maiyalagan, T., Recent Progress in Non-Platinum Counter Electrode Materials for Dye-Sensitized Solar Cells. *ChemElectroChem* **2015,** *2* (7), 928-945.
35. Faber, M. S.; Jin, S., Earth-abundant inorganic electrocatalysts and their nanostructures for energy conversion applications. *Energy Environ. Sci.* **2014,** *7* (11), 3519-3542.
36. Yun, S.; Hagfeldt, A.; Ma, T., Pt-free counter electrode for dye-sensitized solar cells with high efficiency. *Adv Mater* **2014,** *26* (36), 6210-37.
37. Castro-Hermosa, S.; Yadav, S. K.; Vesce, L.; Guidobaldi, A.; Reale, A.; Di Carlo, A.; Brown, T. M., Stability issues pertaining large area perovskite and dye-

sensitized solar cells and modules. *Journal of Physics D: Applied Physics* **2017,** *50* (3), 033001.

38. Sharma, K.; Sharma, V.; Sharma, S. S., Dye-Sensitized Solar Cells: Fundamentals and Current Status. *Nanoscale Res Lett* **2018,** *13* (1), 381.
39. Jeong, J.; Kim, M.; Seo, J.; Lu, H.; Ahlawat, P.; Mishra, A.; Yang, Y.; Hope, M. A.; Eickemeyer, F. T.; Kim, M.; Yoon, Y. J.; Choi, I. W.; Darwich, B. P.; Choi, S. J.; Jo, Y.; Lee, J. H.; Walker, B.; Zakeeruddin, S. M.; Emsley, L.; Rothlisberger, U.; Hagfeldt, A.; Kim, D. S.; Gratzel, M.; Kim, J. Y., Pseudo-halide anion engineering for alpha-FAPbI3 perovskite solar cells. *Nature* **2021,** *592* (7854), 381-385.
40. Miyasaka, T., Perovskite Photovoltaics: Rare Functions of Organo Lead Halide in Solar Cells and Optoelectronic Devices. *Chemistry Letters* **2015,** *44* (6), 720-729.
41. Snaith, H. J., Perovskites: The Emergence of a New Era for Low-Cost, High-Efficiency Solar Cells. *The Journal of Physical Chemistry Letters* **2013,** *4* (21), 3623-3630.
42. Edri, E.; Kirmayer, S.; Cahen, D.; Hodes, G., High Open-Circuit Voltage Solar Cells Based on Organic-Inorganic Lead Bromide Perovskite. *J Phys Chem Lett* **2013,** *4* (6), 897-902.
43. Liang, Y.; Wang, Y.; Mu, C.; Wang, S.; Wang, X.; Xu, D.; Sun, L., Achieving High Open-Circuit Voltages up to 1.57 V in Hole-Transport-Material-Free MAPbBr3 Solar Cells with Carbon Electrodes. *Advanced Energy Materials* **2018,** *8* (4), 1701159.
44. Li, F.; Ma, C.; Wang, H.; Hu, W.; Yu, W.; Sheikh, A. D.; Wu, T., Ambipolar solution-processed hybrid perovskite phototransistors. *Nat Commun* **2015,** *6*, 8238.
45. Chang, X.; Fan, Y.; Zhao, K.; Fang, J.; Liu, D.; Tang, M. C.; Barrit, D.; Smilgies, D. M.; Li, R.; Lu, J.; Li, J.; Yang, T.; Amassian, A.; Ding, Z.; Chen, Y.; Liu, S. F.; Huang, W., Perovskite Solar Cells toward Eco-Friendly Printing. *Research (Wash D C)* **2021,** *2021*, 9671892.
46. Ko, Y.; Kim, Y.; Lee, C.; Kim, Y.; Jun, Y., Investigation of Hole-Transporting Poly(triarylamine) on Aggregation and Charge Transport for Hysteresisless Scalable Planar Perovskite Solar Cells. *ACS Appl Mater Interfaces* **2018,** *10* (14),

11633-11641.

47. Seok, S. I.; Gratzel, M.; Park, N. G., Methodologies toward Highly Efficient Perovskite Solar Cells. *Small* **2018,** *14* (20), e1704177.
48. Sewvandi, G. A.; Hu, D.; Chen, C.; Ma, H.; Kusunose, T.; Tanaka, Y.; Nakanishi, S.; Feng, Q., Antiferroelectric-to-Ferroelectric Switching inCH3NH3PbI3Perovskite and Its Potential Role in Effective Charge Separation in Perovskite Solar Cells. *Physical Review Applied* **2016,** *6* (2).
49. Li, H.; Zhang, W., Perovskite Tandem Solar Cells: From Fundamentals to Commercial Deployment. *Chem Rev* **2020,** *120* (18), 9835-9950.
50. Li, J.; Duan, J.; Yang, X.; Duan, Y.; Yang, P.; Tang, Q., Review on recent progress of lead-free halide perovskites in optoelectronic applications. *Nano Energy* **2021,** *80*, 105526.
51. Noh, J. H.; Im, S. H.; Heo, J. H.; Mandal, T. N.; Seok, S. I., Chemical management for colorful, efficient, and stable inorganic-organic hybrid nanostructured solar cells. *Nano Lett* **2013,** *13* (4), 1764-9.
52. Venkateswari, R.; Sreejith, S., Factors influencing the efficiency of photovoltaic system. *Renewable and Sustainable Energy Reviews* **2019,** *101*, 376-394.
53. Polman, A.; Knight, M.; Garnett, E. C.; Ehrler, B.; Sinke, W. C., Photovoltaic materials: Present efficiencies and future challenges. *Science* **2016,** *352* (6283), aad4424.
54. Lei, B.; Yao, Y.; Kumar, A.; Yang, Y.; Ozolins, V., Quantifying the relation between the morphology and performance of polymer solar cells using Monte Carlo simulations. *Journal of Applied Physics* **2008,** *104* (2), 024504.
55. Li, Y.; Ji, L.; Liu, R.; Zhang, C.; Mak, C. H.; Zou, X.; Shen, H.-H.; Leu, S.-Y.; Hsu, H.-Y., A review on morphology engineering for highly efficient and stable hybrid perovskite solar cells. *Journal of Materials Chemistry A* **2018,** *6* (27), 12842-12875.
56. Saliba, M.; Matsui, T.; Seo, J. Y.; Domanski, K.; Correa-Baena, J. P.; Nazeeruddin, M. K.; Zakeeruddin, S. M.; Tress, W.; Abate, A.; Hagfeldt, A.; Gratzel, M., Cesium-containing triple cation perovskite solar cells: improved stability, reproducibility and high efficiency. *Energy Environ Sci* **2016,** *9* (6), 1989-1997.

57. Shiu, S.-C.; Chao, J.-J.; Hung, S.-C.; Yeh, C.-L.; Lin, C.-F., Morphology Dependence of Silicon Nanowire/Poly(3,4-ethylenedioxythiophene):Poly(styrenesulfonate) Heterojunction Solar Cells. *Chemistry of Materials* **2010,** *22* (10), 3108-3113.
58. Andreani, L. C.; Bozzola, A.; Kowalczewski, P.; Liscidini, M.; Redorici, L., Silicon solar cells: toward the efficiency limits. *Advances in Physics: X* **2018,** *4* (1), 1548305.
59. Bag, A.; Radhakrishnan, R.; Nekovei, R.; Jeyakumar, R., Effect of absorber layer, hole transport layer thicknesses, and its doping density on the performance of perovskite solar cells by device simulation. *Solar Energy* **2020,** *196*, 177-182.
60. Kirchartz, T.; Agostinelli, T.; Campoy-Quiles, M.; Gong, W.; Nelson, J., Understanding the Thickness-Dependent Performance of Organic Bulk Heterojunction Solar Cells: The Influence of Mobility, Lifetime, and Space Charge. *J Phys Chem Lett* **2012,** *3* (23), 3470-5.
61. Wang, S.; Sakurai, T.; Wen, W.; Qi, Y., Energy Level Alignment at Interfaces in Metal Halide Perovskite Solar Cells. *Advanced Materials Interfaces* **2018,** *5* (22), 1800260.
62. Zhu, L.; Xie, Y.; Zheng, X.; Yin, X.; Tian, X., Growth of Compound BiIII- VIA-VIIACrystals with Special Morphologies under Mild Conditions. *Inorganic Chemistry* **2002,** *41* (17), 4560-4566.
63. Nitsche, R.; Merz, W. J., Photoconduction in ternary V-VI-VII compounds. *Journal of Physics and Chemistry of Solids* **1960,** *13* (1-2), 154-155.
64. Ghosez, P.; Michenaud, J. P.; Gonze, X., Dynamical atomic charges: The case ofABO3compounds. *Physical Review B* **1998,** *58* (10), 6224-6240.
65. Du, M.-H.; Singh, D. J., Enhanced Born charge and proximity to ferroelectricity in thallium halides. *Physical Review B* **2010,** *81* (14).
66. Du, M. H., Efficient carrier transport in halide perovskites: theoretical perspectives. *Journal of Materials Chemistry A* **2014,** *2* (24), 9091-9098.
67. Shi, H.; Ming, W.; Du, M.-H., Bismuth chalcohalides and oxyhalides as optoelectronic materials. *Physical Review B* **2016,** *93* (10), 104108-1.

68. Voutsas, G. P.; Rentzeperis, P. J., The crystal structure of the paraelectric bismuth thiochloride, BiSCl. *Zeitschrift für Kristallographie - Crystalline Materials* **1980,** *152* (1-4).
69. Bletskan, D. I.; Kopinets, I. F.; Rubish, I. D.; Turyanitsa, I. I.; Shtilikha, M. V., Photoconductivity and photoluminescence in BiOCl crystals. *Soviet Physics Journal* **1973,** *16* (5), 646-648.
70. Xiao, B.; Zhu, M.; Ji, L.; Zhang, B.-B.; Dong, J.; Yu, J.; Sun, Q.; Jie, W.; Xu, Y., Centimeter size BiSeI crystal grown by physical vapor transport method. *Journal of Crystal Growth* **2019,** *517*, 7-11.
71. Cheng, H.; Huang, B.; Dai, Y., Engineering BiOX (X = Cl, Br, I) nanostructures for highly efficient photocatalytic applications. *Nanoscale* **2014,** *6* (4), 2009-26.
72. Shenawi-Khalil, S.; Uvarov, V.; Kritsman, Y.; Menes, E.; Popov, I.; Sasson, Y., A new family of BiO(ClxBr1−x) visible light sensitive photocatalysts. *Catalysis Communications* **2011,** *12* (12), 1136-1141.
73. Zhang, X.; Wang, L. W.; Wang, C. Y.; Wang, W. K.; Chen, Y. L.; Huang, Y. X.; Li, W. W.; Feng, Y. J.; Yu, H. Q., Synthesis of BiOClx Br1-x Nanoplate Solid Solutions as a Robust Photocatalyst with Tunable Band Structure. *Chemistry* **2015,** *21* (33), 11872-7.
74. Chen, Y.; Tian, G.; Feng, T.; Zhou, W.; Ren, Z.; Han, T.; Xiao, Y.; Fu, H., Single-crystalline Bi19Br3S27 nanorods with an efficiently improved photocatalytic activity. *CrystEngComm* **2015,** *17* (32), 6120-6126.
75. Zhang, K.; Liu, C.; Huang, F.; Zheng, C.; Wang, W., Study of the electronic structure and photocatalytic activity of the BiOCl photocatalyst. *Applied Catalysis B: Environmental* **2006,** *68* (3-4), 125-129.
76. Miehe, G.; Kupčík, V., Die Kristallstruktur des Bi(Bi2S3)9J3. *Die Naturwissenschaften* **1971,** *58* (4), 219-219.
77. Shen, G.; Chen, D.; Tang, K.; Huang, L.; Qian, Y., Large-scale synthesis of (Bi(Bi2S3)9I3)0.667 submicrometer needle-like crystals via a novel polyol route. *Journal of Crystal Growth* **2003,** *249* (1-2), 331-334.
78. Yan, Y.; Xu, Y.; Lei, S.; Ou, X.; Chen, L.; Xiong, J.; Xiao, Y.; Cheng, B.,

Fabrication of Bi19S27I3 nanorod cluster films for enhanced photodetection performance. *Dalton Transactions* **2018,** *47* (10), 3408-3416.

79. Ho, C. H.; Chen, Y. H.; Kuo, Y. K.; Liu, C. W., The structure and opto-thermo electronic properties of a new (Bi(Bi2S3)9I3)2/3 hexagonal nano-/micro-rod. *Chem Commun (Camb)* **2017,** *53* (26), 3741-3744.
80. Groom, R.; Jacobs, A.; Cepeda, M.; Drummey, R.; Latturner, S. E., Bi13S18I2: (Re)discovery of a Subvalent Bismuth Compound Featuring [Bi2]4+ Dimers Grown in Sulfur/Iodine Flux Mixtures. *Chemistry of Materials* **2017,** *29* (7), 3314-3323.
81. Li, F. T.; Wang, Q.; Ran, J.; Hao, Y. J.; Wang, X. J.; Zhao, D.; Qiao, S. Z., Ionic liquid self-combustion synthesis of BiOBr/Bi24O31Br10 heterojunctions with exceptional visible-light photocatalytic performances. *Nanoscale* **2015,** *7* (3), 1116-26.
82. Hoye, R. L. Z.; Lee, L. C.; Kurchin, R. C.; Huq, T. N.; Zhang, K. H. L.; Sponseller, M.; Nienhaus, L.; Brandt, R. E.; Jean, J.; Polizzotti, J. A.; Kursumovic, A.; Bawendi, M. G.; Bulovic, V.; Stevanovic, V.; Buonassisi, T.; MacManus-Driscoll, J. L., Strongly Enhanced Photovoltaic Performance and Defect Physics of Air-Stable Bismuth Oxyiodide (BiOI). *Adv Mater* **2017,** *29* (36).
83. Briand, G. G.; Burford, N., Bismuth compounds and preparations with biological or medicinal relevance. *Chem Rev* **1999,** *99* (9), 2601-58.
84. Maile, F. J.; Pfaff, G.; Reynders, P., Effect pigments—past, present and future. *Progress in Organic Coatings* **2005,** *54* (3), 150-163.
85. Zhao, K.; Zhang, X.; Zhang, L., The first BiOI-based solar cells. *Electrochemistry Communications* **2009,** *11* (3), 612-615.
86. Ye, L.; Liu, J.; Jiang, Z.; Peng, T.; Zan, L., Facets coupling of BiOBr-g-C3N4 composite photocatalyst for enhanced visible-light-driven photocatalytic activity. *Applied Catalysis B: Environmental* **2013,** *142-143*, 1-7.
87. Huang, W. L.; Zhu, Q., DFT calculations on the electronic structures of BiOX (X = F, Cl, Br, I) photocatalysts with and without semicore Bi 5d states. *J Comput Chem* **2009,** *30* (2), 183-90.

88. Zhang, X.; Ai, Z.; Jia, F.; Zhang, L., Generalized One-Pot Synthesis, Characterization, and Photocatalytic Activity of Hierarchical BiOX (X = Cl, Br, I) Nanoplate Microspheres. *The Journal of Physical Chemistry C* **2008,** *112* (3), 747-753.
89. Kunioku, H.; Higashi, M.; Abe, R., Low-Temperature Synthesis of Bismuth Chalcohalides: Candidate Photovoltaic Materials with Easily, Continuously Controllable Band gap. *Sci Rep* **2016,** *6*, 32664.
90. Gnayem, H.; Sasson, Y., Hierarchical Nanostructured 3D Flowerlike BiOClxBr1–x Semiconductors with Exceptional Visible Light Photocatalytic Activity. *ACS Catalysis* **2013,** *3* (2), 186-191.
91. Ren, K.; Liu, J.; Liang, J.; Zhang, K.; Zheng, X.; Luo, H.; Huang, Y.; Liu, P.; Yu, X., Synthesis of the bismuth oxyhalide solid solutions with tunable band gap and photocatalytic activities. *Dalton Trans* **2013,** *42* (26), 9706-12.
92. He, R.; Xu, D.; Cheng, B.; Yu, J.; Ho, W., Review on nanoscale Bi-based photocatalysts. *Nanoscale Horizons* **2018,** *3* (5), 464-504.
93. Nishimura, N.; Suzuki, H.; Higashi, M.; Abe, R., A pressure-assisted low temperature sintering of particulate bismuth chalcohalides BiSX (X = Br, I) for fabricating efficient photoelectrodes with porous structures. *Journal of Photochemistry and Photobiology A: Chemistry* **2021,** *413*, 113264.
94. Nowak, M.; Jesionek, M.; Mistewicz, K., Applications of group 15 ternary chalcohalide nanomaterials. **2019**, 225-282.
95. Ran, Z.; Wang, X.; Li, Y.; Yang, D.; Zhao, X.-G.; Biswas, K.; Singh, D. J.; Zhang, L., Bismuth and antimony-based oxyhalides and chalcohalides as potential optoelectronic materials. *npj Computational Materials* **2018,** *4* (1).
96. Booth, J. M.; Klymenko, M. V.; Cole, J. H.; Russo, S. P., Accurate calculation of excitonic signatures in the absorption spectrum of BiSBr using semiconductor Bloch equations. *Physical Review B* **2021,** *103* (11).
97. Zhang, H.; Sun, S. H.; Liu, J. C.; Hong, F.; Zhu, Y.; Zhou, B.; Hu, Y. M., A Study on N-Type Bismuth Sulphochloride (BiSCl): Efficient Synthesis and Characterization. *Nano* **2020,** *15* (09), 2050116.

98. Murtaza, S. Z. M.; Vaqueiro, P., Rapid synthesis of chalcohalides by ball milling: Preparation and characterisation of BiSI and BiSeI. *Journal of Solid State Chemistry* **2020,** *291*, 121625.
99. Audzijonis, A.; Gaigalas, G.; Žigas, L.; Sereika, R.; Žaltauskas, R.; Balnionis, D.; Rėza, A., Electronic structure and optical properties of BiSeI crystal. *physica status solidi (b)* **2009,** *246* (7), 1702-1708.
100. Ganose, A. M.; Matsumoto, S.; Buckeridge, J.; Scanlon, D. O., Defect Engineering of Earth-Abundant Solar Absorbers BiSI and BiSeI. *Chem Mater* **2018,** *30* (11), 3827-3835.
101. Wu, Y.; Pan, H.; Zhou, X.; Li, M.; Zhou, B.; Yang, C.; Zhang, W. H.; Jie, J.; Li, C., Shape and composition control of Bi19S27(Br3-x ,I x) alloyed nanowires: the role of metal ions. *Chem Sci* **2015,** *6* (8), 4615-4622.
102. Duan, F.; Wang, X.; Tan, T.; Chen, M., Highly exposed surface area of {001} facets dominated BiOBr nanosheets with enhanced visible light photocatalytic activity. *Phys Chem Chem Phys* **2016,** *18* (8), 6113-21.
103. Shi, X.; Chen, X.; Chen, X.; Zhou, S.; Lou, S.; Wang, Y.; Yuan, L., PVP assisted hydrothermal synthesis of BiOBr hierarchical nanostructures and high photocatalytic capacity. *Chemical Engineering Journal* **2013,** *222*, 120-127.
104. Li, H.; Zhang, L., Photocatalytic performance of different exposed crystal facets of BiOCl. *Current Opinion in Green and Sustainable Chemistry* **2017,** *6*, 48-56.
105. Yin, S.; Di, J.; Li, M.; Sun, Y.; Xia, J.; Xu, H.; Fan, W.; Li, H., Ionic liquid-assisted synthesis and improved photocatalytic activity of p-n junction g-C3N4/BiOCl. *Journal of Materials Science* **2016,** *51* (10), 4769-4777.
106. Hu, J.; Wu, X.; Huang, C.; Fan, W.; Qiu, X., Visible light photocatalytic activity induced by Rh(III) modification on the surface of BiOCl. *Applied Surface Science* **2016,** *387*, 45-50.
107. Liu, W.; Shang, Y.; Zhu, A.; Tan, P.; Liu, Y.; Qiao, L.; Chu, D.; Xiong, X.; Pan, J., Enhanced performance of doped BiOCl nanoplates for photocatalysis: understanding from doping insight into improved spatial carrier separation. *Journal of Materials Chemistry A* **2017,** *5* (24), 12542-12549.

108. Maisano, M.; Dozzi, M. V.; Selli, E., Searching for facet-dependent photoactivity of shape-controlled anatase TiO 2. *Journal of Photochemistry and Photobiology C: Photochemistry Reviews* **2016,** *28*, 29-43.

109. Jia, M.; Hu, X.; Wang, S.; Huang, Y.; Song, L., Photocatalytic properties of hierarchical BiOXs obtained via an ethanol-assisted solvothermal process. *J Environ Sci (China)* **2015,** *35*, 172-180.

110. Lei, Y.; Wang, G.; Song, S.; Fan, W.; Pang, M.; Tang, J.; Zhang, H., Room temperature, template-free synthesis of BiOI hierarchical structures: visible-light photocatalytic and electrochemical hydrogen storage properties. *Dalton Trans* **2010,** *39* (13), 3273-8.

111. Wu, Z.; Jiang, Y.; Xiong, X.; Ding, S.; Shi, Y.; Liu, X.; Liu, Y.; Huang, Z.; Hu, J., Synthesis and characterization of single-crystalline Bi19Cl3S27 nanorods. *Catalysis Science & Technology* **2017,** *7* (16), 3464-3468.

112. Deng, C.; Guan, H.; Tian, X., Novel Bi19S27Br3 superstructures: facile microwave-assisted aqueous synthesis and their visible light photocatalytic performance. *Materials Letters* **2013,** *108*, 17-20.

113. Jiang, D.; Du, X.; Chen, D.; Li, Y.; Hao, N.; Qian, J.; Zhong, H.; You, T.; Wang, K., Facile wet chemical method for fabricating p-type BiOBr/n-type nitrogen doped graphene composites: Efficient visible-excited charge separation, and high-performance photoelectrochemical sensing. *Carbon* **2016,** *102*, 10-17.

114. Zhou, C.; Wang, R.; Jiang, C.; Chen, J.; Wang, G., Dynamically Optimized Multi-interface Novel BiSI-Promoted Redox Sites Spatially Separated n–p–n Double Heterojunctions BiSI/MoS2/CdS for Hydrogen Evolution. *Industrial & Engineering Chemistry Research* **2019,** *58* (19), 7844-7856.

115. Zhang, R.; Zeng, K., A novel flower-like dual Z-scheme BiSI/Bi2WO6/g-C3N4 photocatalyst has excellent photocatalytic activity for the degradation of organic pollutants under visible light. *Diamond and Related Materials* **2021,** *115*, 108343.

116. Hahn, N. T.; Self, J. L.; Mullins, C. B., BiSI Micro-Rod Thin Films: Efficient Solar Absorber Electrodes? *J Phys Chem Lett* **2012,** *3* (11), 1571-6.

117. Wang, K.; Jia, F.; Zheng, Z.; Zhang, L., Crossed BiOI flake array solar cells.

Electrochemistry Communications **2010,** *12* (12), 1764-1767.

118. Hahn, N. T.; Hoang, S.; Self, J. L.; Mullins, C. B., Spray pyrolysis deposition and photoelectrochemical properties of n-type BiOI nanoplatelet thin films. *ACS Nano* **2012,** *6* (9), 7712-22.

119. Sfaelou, S.; Raptis, D.; Dracopoulos, V.; Lianos, P., BiOI solar cells. *RSC Advances* **2015,** *5* (116), 95813-95816.

120. Hahn, N. T.; Rettie, A. J. E.; Beal, S. K.; Fullon, R. R.; Mullins, C. B., n-BiSI Thin Films: Selenium Doping and Solar Cell Behavior. *The Journal of Physical Chemistry C* **2012,** *116* (47), 24878-24886.

121. Tiwari, D.; Cardoso-Delgado, F.; Alibhai, D.; Mombrú, M.; Fermín, D. J., Photovoltaic Performance of Phase-Pure Orthorhombic BiSI Thin-Films. *ACS Applied Energy Materials* **2019,** *2* (5), 3878-3885.

122. Xiong, J.; You, Z.; Lei, S.; Zhao, K.; Bian, Q.; Xiao, Y.; Cheng, B., Solution Growth of BiSI Nanorod Arrays on a Tungsten Substrate for Solar Cell Application. *ACS Sustainable Chemistry & Engineering* **2020,** *8* (35), 13488-13496.

123. Adams, K.; González, A. F.; Mallows, J.; Li, T.; Thijssen, J. H. J.; Robertson, N., Facile synthesis and characterization of Bi13S18I2 films as a stable supercapacitor electrode material. *Journal of Materials Chemistry A* **2019,** *7* (4), 1638-1646.

Chapter II

Bismuth Chalcogenide Iodides of $Bi_{13}S_{18}I_2$ and BiSI: Solvothermal Synthesis, Photoelectric Behavior, and Photovoltaic Performance

2.1 Introduction

As the global demand for energy is expected to grow rapidly, the securing of clean energy is essential for sustainable economic growth. The solar energy is the most promising clean energy source for the next-generation.[1, 2] At present, the photovoltaic (PV) market is dominated by crystalline silicon panels which possess relatively high efficiency, but the high cost has prompted the development of low cost high performance PVs.[3] Some new types of PVs, such as the thin film type of $CuIn_{1-x}Ga_xSe_2$ (CIGS) and CdTe PVs, have been developed to reduce the cost and increase power conversion efficiency (PCE). Although the PCE of these PVs having recently reached 22%, their potential and future prospect are limited by the high cost of indium and scarcity of tellurium.[4,5]

Recently the Pb-based hybrid halide perovskites, such as $CH_3NH_3PbI_3$ (MAPI), have attracted much attention as a promising solar light absorbers for PV due to the high PCE and the low cost of the solution fabrication process.[6, 7] Although it was first reported only 10 years ago, the PCE of the PVs using a hybrid perovskite as a light absorber has reached to 24.2%,[8] surpassing all other third-generation PVs, and this fast-growing PCE is a new record in the history of PV technology.[9] Unfortunately, in addition to humidity and thermal instability, the Pb-based hybrid halide perovskites pose a potential environmental risk due to leaching of toxic Pb.[10-12] In order to solve these problems, there is an urgent need to explore alternative light absorber materials consisting of nontoxic

elements. The substitution of Pb(II) with Bi(III) in the hybrid perovskites is attractive because both Bi(III) and Pb(II) have the same $6s^2 6p^0$ electronic configuration, thus ensuring that their compounds will share similar properties. Some studies suggest that Bi-based hybrid perovskites are promising as the PV light absorber, but the success on the synthesis of Bi-based hybrid perovskites has not been reported.[13-16] A non-toxic bismuth-halide double perovskite $A_3Bi_2X_9$ ($A = Cs^+$, Ag, $CH_3NH_3^+$ and $HC(NH_2)^{2+}$; $X = I^-$, Br^-, Cl^-) has been much investigated and employed for solar cells,[16] just possessing a PCE of 3.2% up to now.[17]

Recently, some V-VI-VII compounds (V=Sb, Bi, VI=O, S, Se, VII= Cl,Br, I), have attracted much attention as potential electronic materials. These compounds exhibit a variety of physical characteristics, including high photoconductivity, ferroelectric photovoltaic effect,[18] piezoelectricity, electrooptical effect[19, 20] and structural diversity.[13, 14] BiSX compounds have attracted significant attention as PV materials because of their excellent semiconducting properties and narrow bandgaps, which enables the absorption of the solar spectrum in a wide wavelength range.[21, 22] Another important advantage is that the bandgaps are tunable via substitution between halogens each other, such as $BiSBr_{1-x}I_x$ solid solutions.[23] Recently, Hahn et al. have described a solar cell using a BiSI semiconductor thin film as a lighter-absorber, which yielded a PCE of 0.25%.[24] Tiwari et al. described solution based way to fabricate a BiSI-based solar cell, employing poly as hole transport material, showing a record PCE of 1.32%.[25] BiOX compounds possess tunable bandgaps from 3.46 eV for BiOCl to 1.77 eV for BiOI, and exhibit superior photocatalytic activities.[21, 26] BiSX compounds are synthesized generally using a vapor transport process at high temperature above 400 °C in a vacuum tube.[27] BiSI can also be obtained through a solvothermal process and melt growth process by the Bridgeman-Stockbarger technique.[20, 28]

Fewer studies have been reported on $Bi_{19}S_{27}X_3$ (X=Cl, Br, I) compounds. Traditionally, these bismuth sulfohalogenides are synthesized using a vapor

transport process and flux process under high temperature conditions over 600°C.[29, 30] A solvothermal process has also been employed to obtain $Bi_{19}S_{27}X_3$ nanocrystals.[31-33] The $Bi_{19}S_{27}Br_3$ and $Bi_{19}S_{27}Cl_3$ nanocrystals exhibit efficient photocatalytic degradation of 2,4-dichorophenol and the reduction of Cr(VI).[32, 33] The characteristics and structure of $Bi_{19}S_{27}I_3$ remain unclear. Ho et al. have reported that this compound possesses an indirect bandgap at 0.80 eV and a direct bandgap at 1.08 eV, respectively.[30] However, Groom et al. have reported that this compound is an indirect bandgap semiconductor based on the single crystal structure study and electronic structure calculations, furthermore, the result also revealed that this compound can be expressed as a new composition formula of $Bi_{13}S_{18}I_2$.[29] Very recently, Yan et al. have fabricated the $Bi_{19}S_{27}I_3$ nanorod cluster films through a solvothermal process and it was applied to a photodetector.[34] However, to the best of our knowledge, there have been no published reports of $Bi_{13}S_{18}I_2$-based solar cells.

Herein, we creatively employed a facile solvothermal process for the synthesis of bismuth chalcogenide iodides of $Bi_{13}S_{18}I_2$ and BiSI and systematical characterization of their photoelectric behavior as a light absorber for solar cells. A possible formation mechanism for $Bi_{13}S_{18}I_2$ and BiSI under the solvothermal conditions is proposed. Both $Bi_{13}S_{18}I_2$ and BiSI are n-type of semiconductors with the bandgaps of 0.80 and 1.57 eV, respectively. We modified the solvothermal process to fabricate $Bi_{13}S_{18}I_2$ nanorod film on a porous TiO_2 nanocrystal film for a new type of $Bi_{13}S_{18}I_2$-based solar cells. The preliminary PV study produced a PCE of 0.85%, suggesting the potential of the $Bi_{13}S_{18}I_2$-based solar cells which can be fabricated by the low-cost solution process.

2.2 Experimental details

2.2.1 Synthesis of bismuth chalcogenide iodide powder samples and fabrication of their pellet samples.

CH_3NH_3I (MAI) was synthesized by the reaction of 24 mL of methylamine and 10 mL of HI solution at 0 °C for 2 h in a rotary evaporator at 120 rpm, and then evaporated at 80 °C. The precipitate was washed three times with ethanol and then diethyl at room temperature and then dried at 60 °C for 24 h. For the synthesis of a bismuth chalcogenide iodide powder sample, BiI_3 (2 mmol), MAI (3 mmol), and a desired amount of CH_4N_2S were added into 5 mL of ethylene glycol solvent. The mixture was solvothermally treated at a desired temperature for 12 h under stirring conditions. The obtained sample was filtrated, washed with ethyl alcohol, and then dried in a drying oven at 60 ^oC for 12 h.

Synthesized bismuth chalcogenide iodide powder sample was gently ground into fine powder. This powder sample was then pressed using a pallet press mold with a diameter of 10 mm at 30 MPa for 3 min. Subsequently, cold isostatic press (CIP) treatment was employed on the pellet sample with a pressure of 200 MPa for 5 min to increase sample density. The thickness of the pellet was about 1 mm.

2.2.2 Fabrication and characterization of solar cells.

A TiO_2 nanocrystal paste was prepared by mixing a P25 TiO_2 nanocrystal sample (0.5 g), ethanol (2.5 g), α-terpineol (2.0 g), a 10 wt % solution of ethyl-cellulose 10 (1.4 g), and a 10 wt % solution of ethyl-cellulose 45 (1.1 g). The mixture was dispersed by ultrasonication for 30 min and then ball-milling for 72 h. After ball-milling, the ethanol was removed from the mixture using a rotary evaporator.[35]

The TiO_2 electrode was prepared in the following manner.[36] The fluorine-doped tin oxide (FTO) conducting glass plate was cleaned in distilled water and acetone by ultrasonication for 10 min, consecutively. Then the FTO glass plate was dipped in 0.1 M titanium tetraisopropoxide (TTIP) solution for 1 min and washed with distilled water

and ethanol, dried at room temperature, and calcined at 480 °C for 1 h to coat the FTO glass surface with a dense TiO_2 thin film. The prepared TiO_2 paste was then coated on the dense TiO_2 thin film on the FTO glass plate by a screen printing technique and dried at 120 °C for 10 min. This process was repeated to obtain TiO_2 nanocrystal film of about 10μm in thickness. After the TiO_2 paste coating, the TiO_2 film was calcined at 450 °C for 30 min to obtain a TiO_2 nanoporous electrode. The TiO_2 nanoporous electrode was dipped in the 0.1 M TTIP solution for 1 min, washed with distilled water and ethanol, dried at room temperature, and calcined at 480 °C for 1 h again.

$Bi_{13}S_{18}I_2$ film prepared by the following manner: 0.4 mmol BiI_3 (0.2359 g), 0.6 mmol MAI (0.0954 g), and 1.6 mmol CH_4N_2S (1.2179 g) were dissolved in 1 mL ethylene glycol solvent by stirring for 1 h, and then a red BiI_3-MAI-CH_4N_2S mixed solution was obtained. The mixed solution was coated on the TiO_2 nanoporous electrode surface. After standing for 2 h, the coated TiO_2 nanoporous electrode was placed on a shelf set in a Teflon-lined stainless steel autoclave with an internal volume of 80 mL. After adding 1 mL ethylene glycol solvent to the autoclave bottom, the autoclave was sealed and solvothermally treated at 195 ºC for 12 h. Upon cooling to room temperature, a black $Bi_{13}S_{18}I_2$-coated TiO_2 electrode was obtained. The $Bi_{13}S_{18}I_2$-coated TiO_2 electrode was washed with ethanol and then dried at 60 ºC for 12 h in a drying oven.

The $Bi_{13}S_{18}I_2$-solar cell was comprised of the $Bi_{13}S_{18}I_2$-coated TiO_2 electrode as an anode, Pt-coated FTO glass as a cathode, and an electrolyte solution between the anode and the cathode. The electrolyte solution contained 0.1 M LiI, 0.01 M I_2, 0.6 M 1-butyl-3-n-propylimidazolium iodide (BMII), 0.4 M 4-tert-butylpyridine (TBP), and 0.1 M guanidine thiocyanate (GT) in a mixed solvent of acetonitrile and valeronitrile (v/v = 85:15). The photocurrent−voltage characteristic curve for the $Bi_{13}S_{18}I_2$-solar cell was measured using a Hokuto-Denko BAS100B electrochemical analyzer under irradiation with simulated sunlight of AM 1.5 (100 mW/cm^2), using a sunlight simulator (YSS-E40, Yamashita Denso). A light-passing mask was fixed on the surface of the FTO glass of the anode to set the effectively irradiating area on the cell at 0.25 cm^2.

2.2.3 Physical analysis.

The crystal structures of the samples were investigated using a powder X-ray diffractometer (Shimadzu, model XRD-6100) with Cu Kα (λ= 0.1542 nm) radiation. The morphology of the samples was observed using field emission scanning electron microscopy (FE-SEM) (JEOL, ISM-7001F) and the chemical composition was measured using energy dispersive X-ray spectroscopy (EDX) attached to the FE-SEM at 15 kV acceleration voltage. Transmission electron microscopy (TEM) and high-resolution TEM (HR-TEM) observations were performed on a JEOL Model JEM-3010 system at 300 kV. The mott-Schottky plots and transient photocurrent responses were performed using CHI660E electrochemical station (Shanghai Chenhua, China). The ultraviolet-visible-near infrared(UV-Vis-NIR) absorption spectrum was obtained on a Shimadzu solidspec-3700 UV-Vis-NIR spectrophotometer at room temperature. The TG-DTA analysis was carried out using a thermal analyzer (Shimadzu, DTG-60H) at a heating rate of 10 ºC/min. For the conductivity measurement, a voltage of 100 V was applied to the pellet sample, and the current was measured using a ferroelectric testing system (Toyo Corporation, FCE3-4KVSYS) at room temperature. X-ray photoelectron spectroscopy (XPS) was performed using a Kratos AXIS SUPRA X-ray photo-electron spectrometer. The XPS spectra were calibrated to the adventitious carbon peak at 284.8 eV.

2.3 Results and discussion

2.3.1 Solvothermal synthesis of bismuth chalcogenide iodide compounds.

The bismuth chalcogenide iodide compounds of $Bi_{13}S_{18}I_2$ and BiSI were synthesized by solvothermal treatment of a mixture of BiI_3, CH_4N_2S, and CH_3NH_3I (MAI) in an ethylene glycol solvent. The formation of the bismuth chalcogenide iodide compounds is strongly dependent on the CH_4N_2S/BiI_3/MAI mole ratio and reaction temperature. Figure 2.1 shows the XRD patterns of the samples synthesized under the conditions of different CH_4N_2S/BiI_3 mole ratio at 195 ºC, where the BiI_3/MAI mole

ratio was fixed at 2:3. In this reaction system, the iodine amount was excessive for the formation of $Bi_{13}S_{18}I_2$ and BiSI because the mole ratios of Bi/S/I is 13:18:2 in $Bi_{13}S_{18}I_2$ and 1:1:1 in BiSI. The XRD pattern of the sample prepared at a CH_4N_2S/BiI_3 mole ratio of 1:2 can be well indexed to an orthorhombic BiSI phase with a space group of *Pnma* and lattice constants of a = 0.8519, b = 1.0177 and c = 0.4172 nm (JCPDS File No.73-1171). By increasing CH_4N_2S/BiI_3 mole ratio, the $Bi_{13}S_{18}I_2$ phase (JCPDS File No. 73-1157) was formed and became main phase with small amount of metal Bi phase at CH_4N_2S/BiI_3 = 3:2, and then the single $Bi_{13}S_{18}I_2$ phase was formed at CH_4N_2S/BiI_3 = 4:2. The structure of the $Bi_{13}S_{18}I_2$ phase belongs to a hexagonal system with a space group of $P6_3$ and lattice parameters of a = 1.5612 and c = 0.4017 nm.[29] When the CH_4N_2S/BiI_3 mole ratio was increased to 8:2, the $Bi_{13}S_{18}I_2$ phase disappeared, where a Bi_2S_3 single phase was formed. The above results reveal that the products are sensitive to the Bi/S mole ratio in this solvothermal reaction system.

To provide a phase diagram for the BiI_3-CH_4N_2S-MAI solvothermal reaction system, the same reaction was carried out at different temperatures and the XRD patterns of the products are shown in Figure 2.2 (A-C). Based on the XRD results, the phase diagram for the BiI_3-CH_4N_2S-MAI solvothermal reaction system is illustrated in Figure 2.1(D). BiSI is preferably formed at low S/Bi mole ratio range below 1.5, namely the Area-I. By increasing the S/Bi mole ratio, a mixture of the BiSI, $Bi_{13}S_{18}I_2$, small amount of metal Bi, and an unknown phase is formed in Area-II. The single $Bi_{13}S_{18}I_2$ phase can be obtained in Area-III. By further increasing the S/Bi mole ratio, Bi_2S_3 is formed in Area-IV, and the single Bi_2S_3 phase is formed in Area-V, suggesting that $Bi_{13}S_{18}I_2$ is unstable under the high S/Bi mole ratio conditions in the BiI_3-CH_4N_2S-MAI solvothermal reaction system.

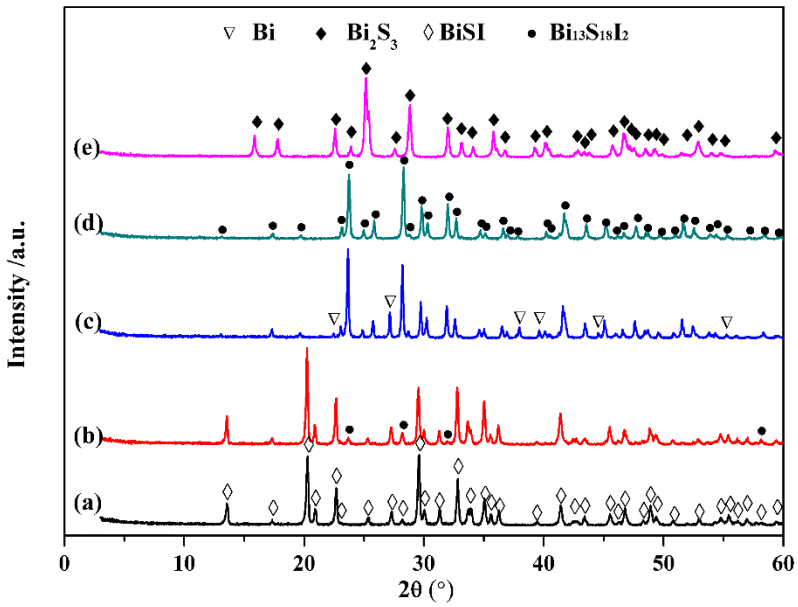

Figure 2.1 XRD patterns of products obtained by solvothermal treatment of solutions with CH_4N_2S/BiI_3/MAI mole ratios of (a) 1:2:3, (b) 2:2:3, (c) 3:2:3, (d) 4:2:3, and (e) 8:2:3 at 195 °C for 12h, respectively.

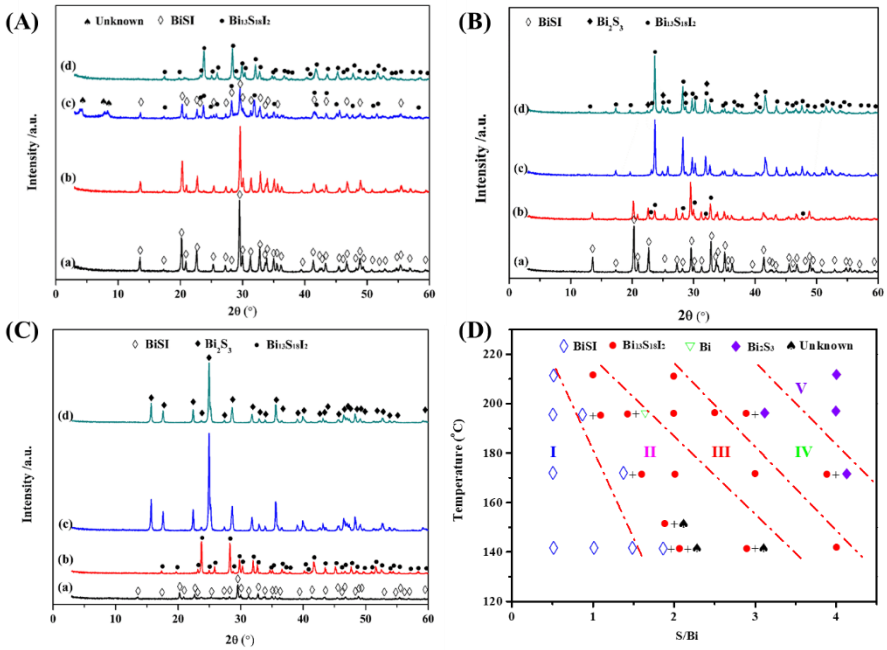

Figure 2.2 XRD patterns of products synthesized by solvothermal treatments of MAI-BiI_3-CH_4N_2S mixtures with CH_4N_2S/BiI_3/MAI mole ratios of (a) 1:2:3, (b) 2:2:3, (c) 4:2:3, (d) 8:2:3 at (A) 140, (B) 170, (C) 210°C for 12 h, respectively. (D) Phase diagram for BiI_3-CH_4N_2S-MAI solvothermal reaction system in ethylene glycol solution with a mole ratio of BiI_3/MAI = 2:3.

Area-I: BiSI; Area-II: mixture of BiSI, $Bi_{13}S_{18}I_2$, Bi and unknown phase; Area-III: $Bi_{13}S_{18}I_2$; Area-IV: mixture of $Bi_{13}S_{18}I_2$ and Bi_2S_3; Area-V: Bi_2S_3.

We also tried to synthesize bismuth chalcogenide iodide compounds in other solvents, such as acetone, DMF, and DMSO. The XRD patterns of the solvothermal products prepared at CH_4N_2S/BiI_3/MAI = 4:2:3 (S/Bi = 2:1) mole ratio and 195 °C are shown in Figure 2.3. Although the single phase of $Bi_{13}S_{18}I_2$ can be formed in acetone solvent, the yield of $Bi_{13}S_{18}I_2$ is disappointing, due to the low reactivity in this solvent. In the DMF solvent, a mixture of the $Bi_{13}S_{18}I_2$ phase and metal Bi phase is formed. However, an unknown phase without $Bi_{13}S_{18}I_2$ is formed in the DMSO solvent. These results suggest that the solvothermal formations of bismuth chalcogenide iodine compounds are sensitive to the solvents. Compared with the high temperature reaction process,[29, 30] the solvothermal process described above is a facile method for the synthesis of the bismuth chalcogenide iodide compounds.

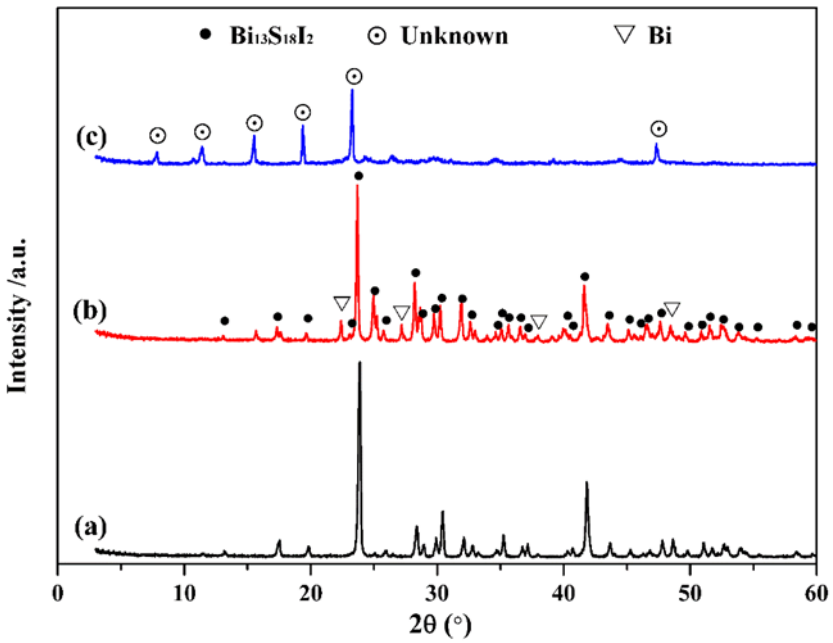

Figure 2.3 XRD patterns of products synthesized by solvothermal treatments CH_4N_2S-BiI_3-MAI mixture with CH_4N_2S/BiI_3/MAI mole ratio of 4:2:3 in (a) acetone, (b) DMF and (c) DMSO solvents at 195 °C for 12 h, respectively.

FE-SEM was employed to investigate the morphology of products obtained

by the solvothermal reaction and the results for the samples prepared at 195 °C are shown in Figure 2.4. The sample obtained at a mole ratio of CH_4N_2S/BiI_3 = 1:2 possesses a fibrous particle morphology with a diameter of about 500 nm and a length of about 20 μm (Figure 2.4(a)). The fibrous particles correspond to BiSI because this sample is a single BiSI phase (Figure 2.1(a)). The fibrous particles and urchin-like particles are observed in the sample of mixed BiSI and $Bi_{13}S_{18}I_2$ phases obtained at a mole ratio of CH_4N_2S/BiI_3 = 2:2 (Figure 2.4(b)), where the fibrous particles can be attributed to the BiSI phase and the urchin-like particles to the $Bi_{13}S_{18}I_2$ phase (Figure 2.1(b)). The $Bi_{13}S_{18}I_2$ single phase sample obtained at a mole ratio of CH_4N_2S/BiI_3 = 4:2 exhibits a rod-like particle morphology with a diameter of about 400 nm and a length of about 5 μm (Figure 2.4(c)). The Bi_2S_3 single phase sample obtained at a mole ratio of CH_4N_2S/BiI_3 = 8:2 shows fibrous and rod-like particle morphologies (Figure 2.4(d)).

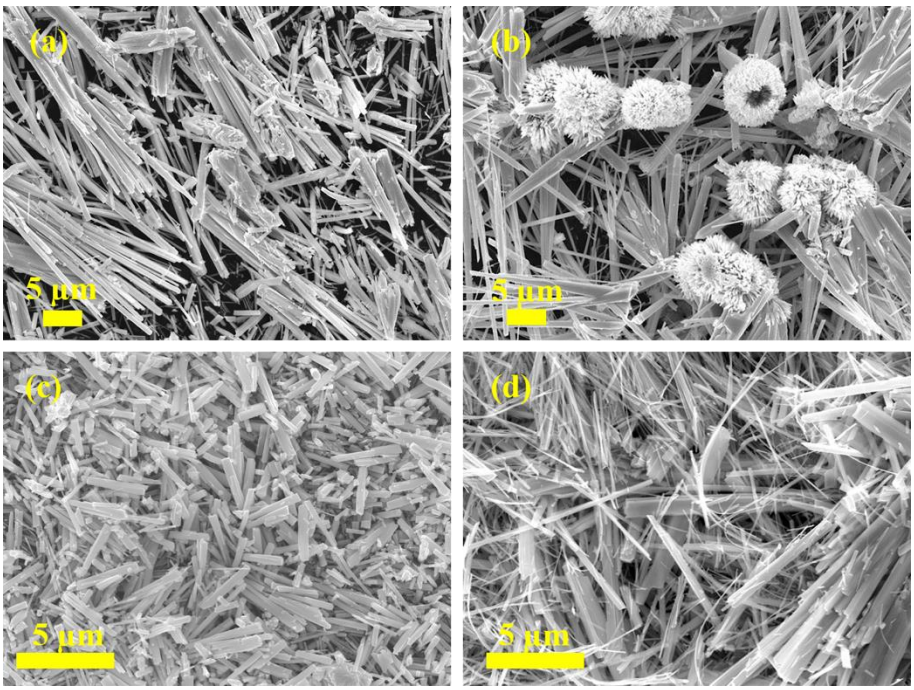

Figure 2.4 FE-SEM images of products synthesized by solvothermal treatment of solutions with CH_4N_2S/BiI_3/MAI mole ratios of (a) 1:2:3, (b) 2:2:3, (c) 4:2:3, (d) 8:2:3 at 195 °C for 12 h, respectively.

The $Bi_{13}S_{18}I_2$ possesses an interesting structure, as shown in Figure 2.5(a).[27] In this

structure, ribbon-like subunits of [Bi_4S_6] form six spokes around a central hexagonal channel at the corners of the unite cell. The [Bi_4S_6]-ribbons spokes are connected together to form a triangular tunnel structure in the direction of c-axial, where I^- located in the tunnel site of the $Bi_{13}S_{18}I_2$ structure. TEM and HRTEM results revealed that the rod-like $Bi_{13}S_{18}I_2$ particles were single crystals, where the rod-like crystal axis direction corresponds to [001] (Figure 2.6); in other words, $Bi_{13}S_{18}I_2$ crystals grow in the direction c-axial. Zhou et al. have proposed that such ribbon structural geometry can exhibit a high conductivity along covalently bonded [Bi_4S_6]-ribbons direction, i.e., the direction of the c-axis, which gives several advantages as light absorbers for solar cells.[37]

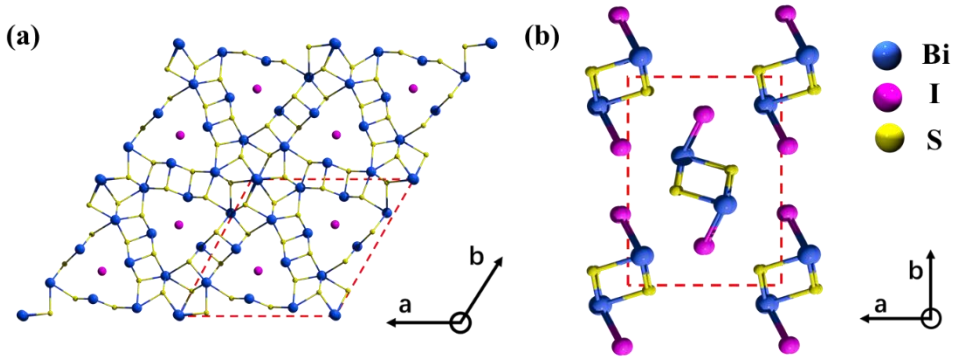

Figure 2.5 Structures of (a) hexagonal $Bi_{13}S_{18}I_2$ and (b) orthorhombic BiSI.

In the BiSI structure, double chain subunit of [$(BiSI)_2$] is formed by linking Bi with S and I together by strong Bi-S and Bi-I bonds along the direction of c-axis, and the [$(BiSI)_2$]-chains are held together by weak Van der Waals type bonds, as shown in Figure 2.5(b).[38] TEM and HRTEM results reveal that rod-like BiSI particles were also single crystals and the rod-like crystals grew in the direction of c-axial in the similar manner as the $Bi_{13}S_{18}I_2$ structure (Figure 2.6).

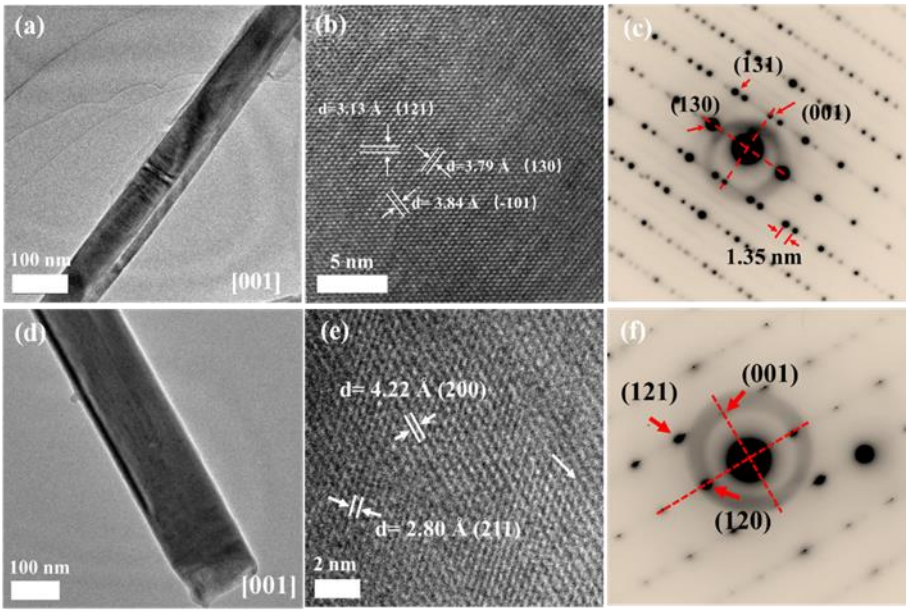

Figure 2.6 (a, d) TEM, (b, e) HRTEM and (c, f) SAED patterns of (a, b, c) $Bi_{13}S_{18}I_2$ and (d, e, f) BiSI nanorods, respectively.

2.3.2 Formation reactions of bismuth chalcogenide iodide compounds

The BiI_3-CH_4N_2S-MAI mixed solution with a mole ratio of 2:4:3 CH_4N_2S/BiI_3/MAI was solvothermally treated at 195 °C for different reaction times to investigate the formation process of bismuth chalcogenide iodide compounds. XRD results indicate that a binary mixture of BiSI and $Bi_{13}S_{18}I_2$ was formed after the reaction occurred for 0.5 h reaction (Figure 2.7). By prolonging the reaction time, the fraction of BiSI decreases and that of $Bi_{13}S_{18}I_2$ increased, then the BiSI disappeared completely after 6 h reaction, and finally the single $Bi_{13}S_{18}I_2$ phase was formed after 12 h reaction. This result suggests that first BiSI is formed, which then converts to $Bi_{13}S_{18}I_2$ under the solvothermal reaction conditions.

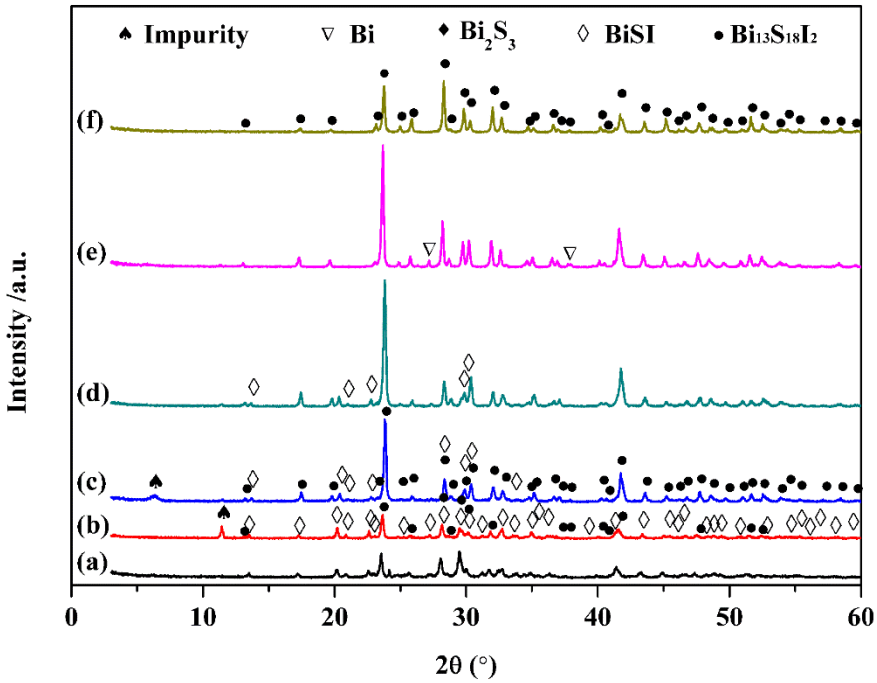

Figure 2.7 XRD patterns of products synthesized by solvothermal treatment of solution with CH_4N_2S/BiI_3/MAI mole ratios of 4:2:3 at 195 ºC for (a) 0.5, (b) 1, (c) 2, (d) 4, (e) 6, (f) 12 h, respectively.

The conversion reaction of BiSI to $Bi_{13}S_{18}I_2$ was investigated by FE-SEM observation (Figure 2.8(A)). In the sample obtained after 0.5 h reaction, large fibrous particles and small urchin-like particles are observed simultaneously. Energy dispersive X-Ray spectroscopy (EDS) analysis reveals that the large fibrous particles and small urchin-like particles have element compositions close to the stoichiometric compositions of BiSI (Bi/S/I =1:1:1) and $Bi_{13}S_{18}I_2$ (Bi/S/I =13:18:2), respectively (Figure 2.9 and Table 1); that is to say, they corresponded to the BiSI phase and $Bi_{13}S_{18}I_2$ phase, respectively. By increasing the reaction time up to 4 h, the urchin-like $Bi_{13}S_{18}I_2$ particles grow in size and their fraction in the product increased, accompanied by the consumption of the fibrous BiSI particles. After 6 h reaction, the urchin-like $Bi_{13}S_{18}I_2$ particles became to rod-like in shape and the fibrous BiSI particles disappeared completely. This reaction process was confirmed by element composition analysis results of SEM-EDS in Figure 2.9 and Table 1, and also corresponds to the XRD results in Figure 2.7.

Based on the results described above, we deduced a reaction mechanism for the

formation of BiSI and $Bi_{13}S_{18}I_2$ in the solvothermal reaction system, as shown in Figure 2.8(B). In the first step, S^{2-} is formed by the decomposition reaction of CH_4N_2S under solvothermal conditions and then BiSI is formed by the solution reaction of Bi(III), S^{2-} and I^-, resulting in the fibrous BiSI particles. In the second step, the crystal nuclei of $Bi_{13}S_{18}I_2$ are formed on surface of the fibrous BiSI particles (Figure 2.8 (A)-(a)) and then increase in size to small urchin-like $Bi_{13}S_{18}I_2$ particles through a BiSI-dissolution reaction and a $Bi_{13}S_{18}I_2$-deposition reaction. In the third step, the small urchin-like $Bi_{13}S_{18}I_2$ particles grow further and finally collapse, becoming the individual rod-like $Bi_{13}S_{18}I_2$ particles through the BiSI-dissolution reaction and the $Bi_{13}S_{18}I_2$-deposition reaction. Thus, the BiSI phase is converted to the $Bi_{13}S_{18}I_2$ phase in this reaction system.

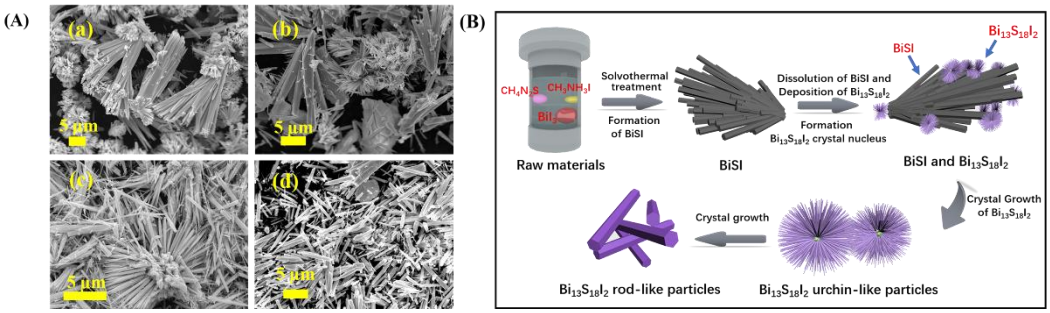

Figure 2.8 (A). FE-SEM images of products synthesized by solvothermal treatment of solution with CH_4N_2S/BiI_3 /MAI mole ratios of 4:2:3 at 195 °C for (a) 0.5, (b) 1, (c) 2, (e) 6 h respectively. (B). Schematic illustration of formation reaction mechanism of BiSI and $Bi_{13}S_{18}I_2$.

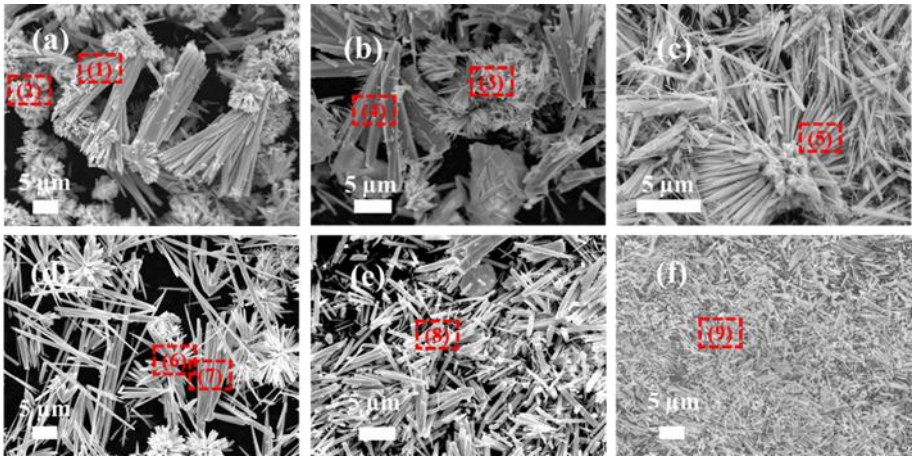

Figure 2.9-A FE-SEM images of products synthesized by solvothermal treatment of solution with CH_4N_2S/ BiI_3/MAI mole ratio of 4:2:3 at 195 °C for (a) 0.5, (b) 1, (c) 2, (d) 4, (e) 6, (f) 12 h,

respectively. Selected Energy Dispersive X-ray spectroscopy (EDS) analysis positions marked with red boxes.

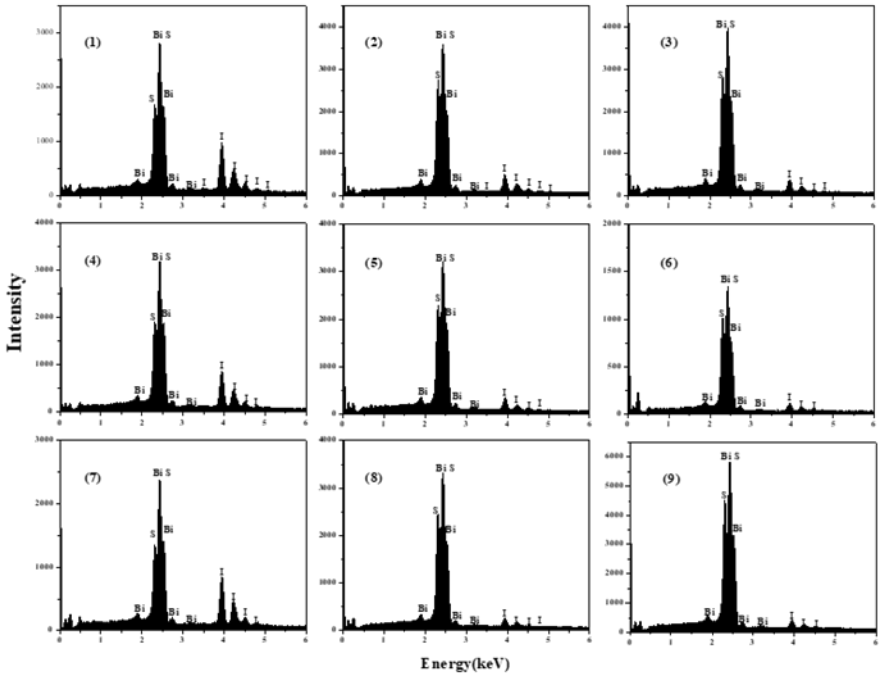

Figure 2.9-B EDS spectra of synthesized products at positions marked in Figure 2.9-A. Numbers correspond to positions marked in FE-SEM images of Figure 2.9-A.

Table 1. EDS analysis results of atonic percentages of samples at positions of marked red boxes in Figure 2.9-A.

Position	**Bi%**	**S %**	**I%**
(1)	33.38	33.81	32.81
(2)	36.60	49.47	13.93
(3)	39.37	50.89	9.73
(4)	35.50	36.68	27.82
(5)	39.78	50.21	10.00
(6)	38.42	53.17	8.41
(7)	33.29	32.07	34.64
(8)	39.39	53.20	7.41
(9)	39.09	54.35	6.56

Expected BiSI	33.3%	33.3%	33.3%
Expected $Bi_{13}S_{18}I_2$	39.4%	54.5%	6.06%

2.3.3 Formation reactions of bismuth chalcogenide iodide compounds

It has been reported that BiSI can be used as a light absorber for solar cells.[4] In the present study, therefore, we investigated the thermostabilities and photoelectric properties of $Bi_{13}S_{18}I_2$ and BiSI to examine the potential of $Bi_{13}S_{18}I_2$ as a light absorber for a new type of solar cells. The $Bi_{13}S_{18}I_2$ and BiSI samples synthesized by solvothermal treatment of the CH_4N_2S-BiI_3-MAI mixed solution with CH_4N_2S/BiI_3/MAI mole ratios of 4:2:3 and 1:2:3 at 195 °C for 12 h, respectively, were used for the characterization. The TG-DTA analysis and XRD results (Figure2.10 and 2.11) suggest that $Bi_{13}S_{18}I_2$ is stable up to 350 °C, and decomposes to BiOI at around 380 °C, and then to Bi_2O_3 at over 500 °C. Like $Bi_{13}S_{18}I_2$, BiSI is stable up to 400 °C, decomposes to a BiOI at around 400 °C and to a Bi_2O_3 at around 500 °C. BiSI exhibits a slightly higher stability than $Bi_{13}S_{18}I_2$ in air.

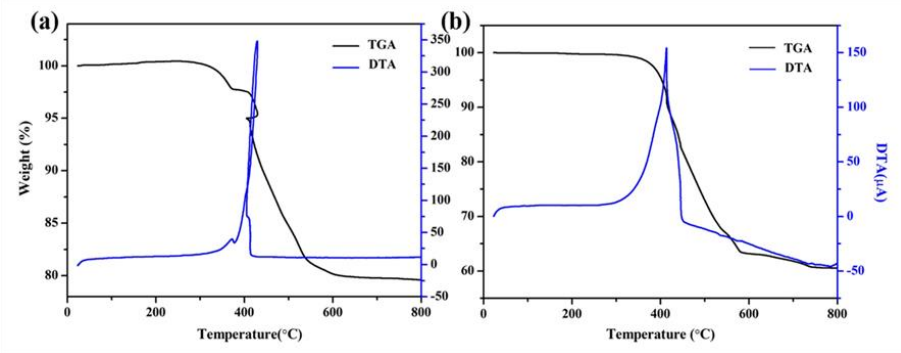

Figure 2.10 TGA-DTA curves for (a) $Bi_{13}S_{18}I_2$ and (b) BiSI samples.

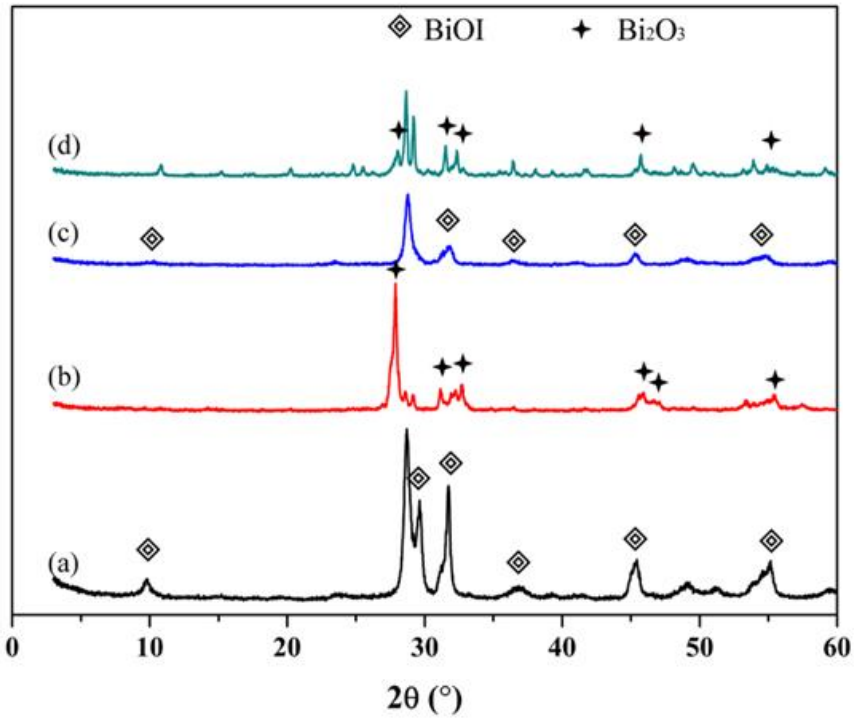

Figure 2.11 XRD patterns of $Bi_{13}S_{18}I_2$ sample after heated at (a) 380 °C and (b) 500 °C, and BiSI sample after heated at (c) 400 °C and (d)500 °C for 2 h, respectively.

The pellet samples of $Bi_{13}S_{18}I_2$ and BiSI were used for the conductivity measurement at room temperature (Figure 2.12). The electrical conductivity (σ) was calculated from the applied voltage (V), measured current (I), thickness of pellet (L), and area (S) of the pellet sample using formula (1).

$$\boldsymbol{\sigma = \frac{I*L}{V*S}} \qquad (1)$$

The calculated electrical conductivity of the $Bi_{13}S_{18}I_2$ pellet sample is 8.85×10^{-7} S/cm, which is much lower than the reported value of 9×10^{-4} S/cm for a single crystal sample.[30] The lower conductivity of the $Bi_{13}S_{18}I_2$ pellet sample can be attributed to the low density of the pellet sample and the grain boundaries because of the rod-like particle morphology of $Bi_{13}S_{18}I_2$, which can be confirmed in its FE-SEM image (Figure 2.12(b)). The BiSI pellet sample has an electrical conductivity of 6.24×10^{-7} S/cm.

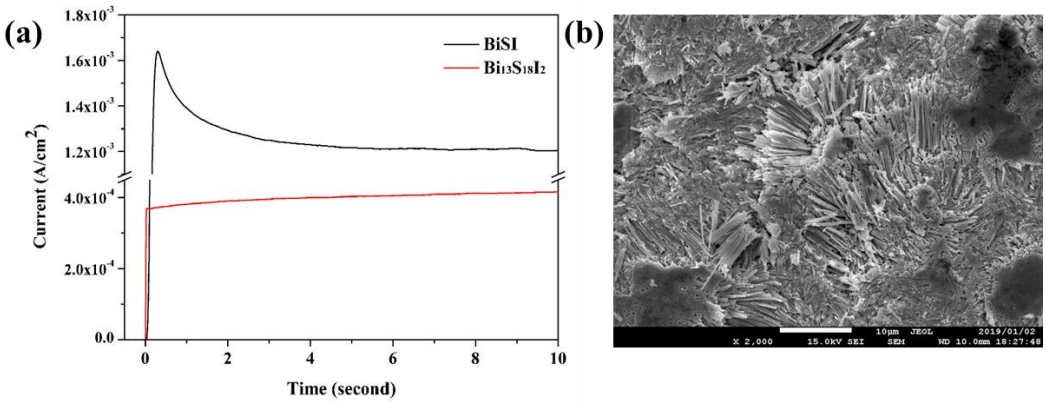

Figure 2.12 (a) Dependences of current density of $Bi_{13}S_{18}I_2$ and BiSI pellet samples on time under applied voltage of 100 V, respectively. (b) FE-SEM image of $Bi_{13}S_{18}I_2$ pellet sample fabricated by pressing powder sample.

The $Bi_{13}S_{18}I_2$ and BiSI samples are black crystals. The UV-Vis-NIR absorption spectra of $Bi_{13}S_{18}I_2$ and BiSI are shown in Figure 2.13. Strong and broad absorption peak around 500 nm in the visible light wavelength range and another strong peak at 1115 nm in the near-IR wavelength range are observed in the $Bi_{13}S_{18}I_2$ absorption spectrum. A flat absorbance in the wavelength range of 300 to 800 nm was observed in the BiSI absorption spectrum. The absorption spectra findings reveal that $Bi_{13}S_{18}I_2$ has smaller bandgap energy than that of BiSI and is thus a promising light absorber for solar cells.

The bandgap energy (E_g) of a semiconductor can be estimated using Tauc's formula $(Ah\nu)^{1/n} = B(h\nu - E_g)$, where A, B, and *hν* are the absorption coefficient, a constant, and the incident photon energy, and the exponent n is equal to 1/2 or 2 for the allowed direct or indirect transitions, respectively.[39] Because $Bi_{13}S_{18}I_2$ and BiSI are indirect semiconductors,[29, 38, 40] Taus's formula can be represented as the Kubelka–Munk function $A = C(h\nu - E_g)^2/h\nu$, where C is the absorption constant.[19, 41] The bandgap energy can be estimated from the transformed Kubelka–Munk function versus the photon energy (Figure 2.13 (b) and (d)). The estimated bandgap energy of the $Bi_{13}S_{18}I_2$ sample was 0.80 eV by extrapolating the straight line to zero absorption intercepting the (hν) axis, which is correspondence with Groom's speculation that the true band gap occurs at lower energies below 0.8 eV.[29] This value corresponds that reported by Ho et

al's.[30] Yan et al. reported a direct band gap of 0.83 eV that is slightly larger than our result.[34] The BiSI sample has a bandgap energy of 1.57 eV, which agrees with reported values of 1.57-1.59 eV.[4, 22, 40]

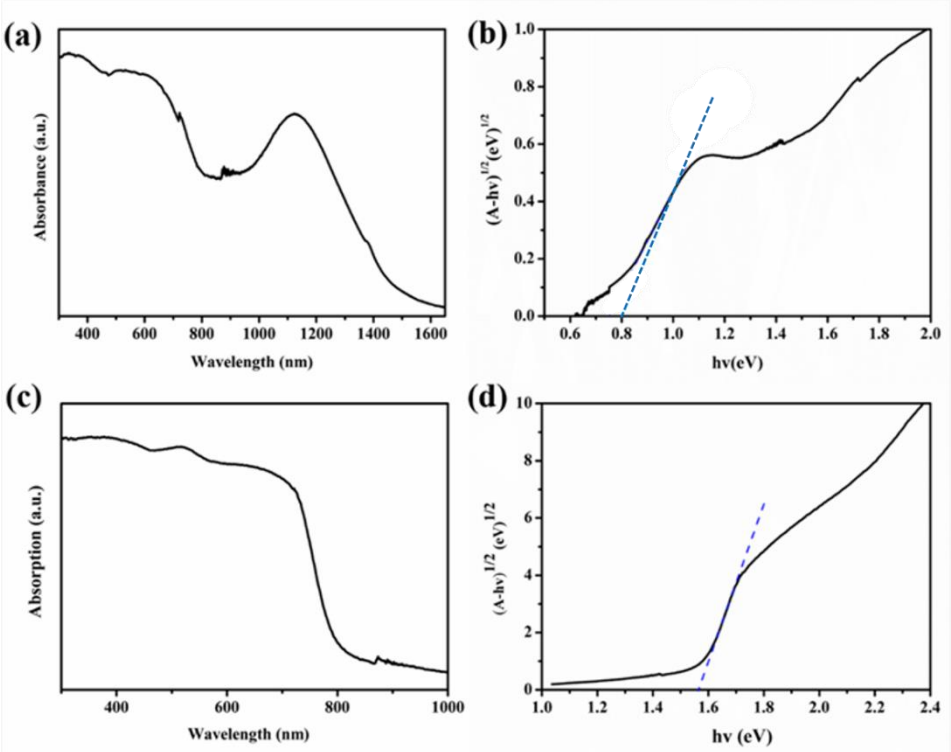

Figure 2.13 UV-Vis-NIR absorption spectra and corresponding plots of transformed Kubelka-Munk function versus *hv* for (a, b) $Bi_{13}S_{18}I_2$ and (c, d) BiSI powder samples, respectively.

X-ray photoelectron spectroscopy (XPS) was used to investigate the surface valence state and the chemical composition of the $Bi_{13}S_{18}I_2$ and BiSI samples. The XPS survey spectrum revealed the predominant presence of sulfur, bismuth and iodine, as well as a small amount of carbon and oxygen impurities in both $Bi_{13}S_{18}I_2$ and BiSI samples (Figure 2.14). The carbon and oxygen may correspond to the residual orgonic precursor and adsorbed oxygen molecules on the particle surface. The Bi spin-orbit doublet peaks of BiSI is consistent with the XPS result of BiSI reported by Grigas et al, where all Bi are trivalent in BiSI.[42] The Bi-$4f_{7/2}$ and Bi $4f_{5/2}$ peaks are observed at 158.7 and 164.0 eV for BiSI and at 158.0 and 163.3 eV for $Bi_{13}S_{18}I_2$. The different binding

energies between $Bi_{13}S_{18}I_2$ and BiSI may account for the existence of bivalent Bi(II) in $Bi_{13}S_{18}I_2$. It has been reported that the bivalent Bi(II) as Bi_2^{4+} dimers is possible in $Bi_{13}S_{18}I_2$, which results in the formation of $(Bi^{3+})_{12}(Bi_2^{4+})_{0.5}(S^{2-})_{18}(I^-)_2$ rather than $Bi_{19}S_{27}I_3$ or $(Bi(Bi_2S_3)_9I_3)_{2/3}$.[29] The XPS result indicates that the atomic ratio of I/Bi/S in the $Bi_{13}S_{18}I_2$ sample is 1:6.5:8.9, which is very close to the stoichiometric mole ratio of 1:6.5:9.0 of $(Bi^{3+})_{12}(Bi_2^{4+})_{0.5}(S^{2-})_{18}(I^-)_2$. A single peak of S-2s is observed at 225.0 and 225.2 eV for $Bi_{13}S_{18}I_2$ and BiSI, respectively. The I-$3d_{3/2}$ and I-$3d_{5/2}$ spin-orbit spin components are observed at 630.1 and 618.6 eV for $Bi_{13}S_{18}I_2$ and 630.2 and 618.7 eV for BiSI, respectively. The binding energies of S-2s, I-$3d_{3/2}$ and I-$3d_{5/2}$ of $Bi_{13}S_{18}I_2$ are very close to those of BiSI.

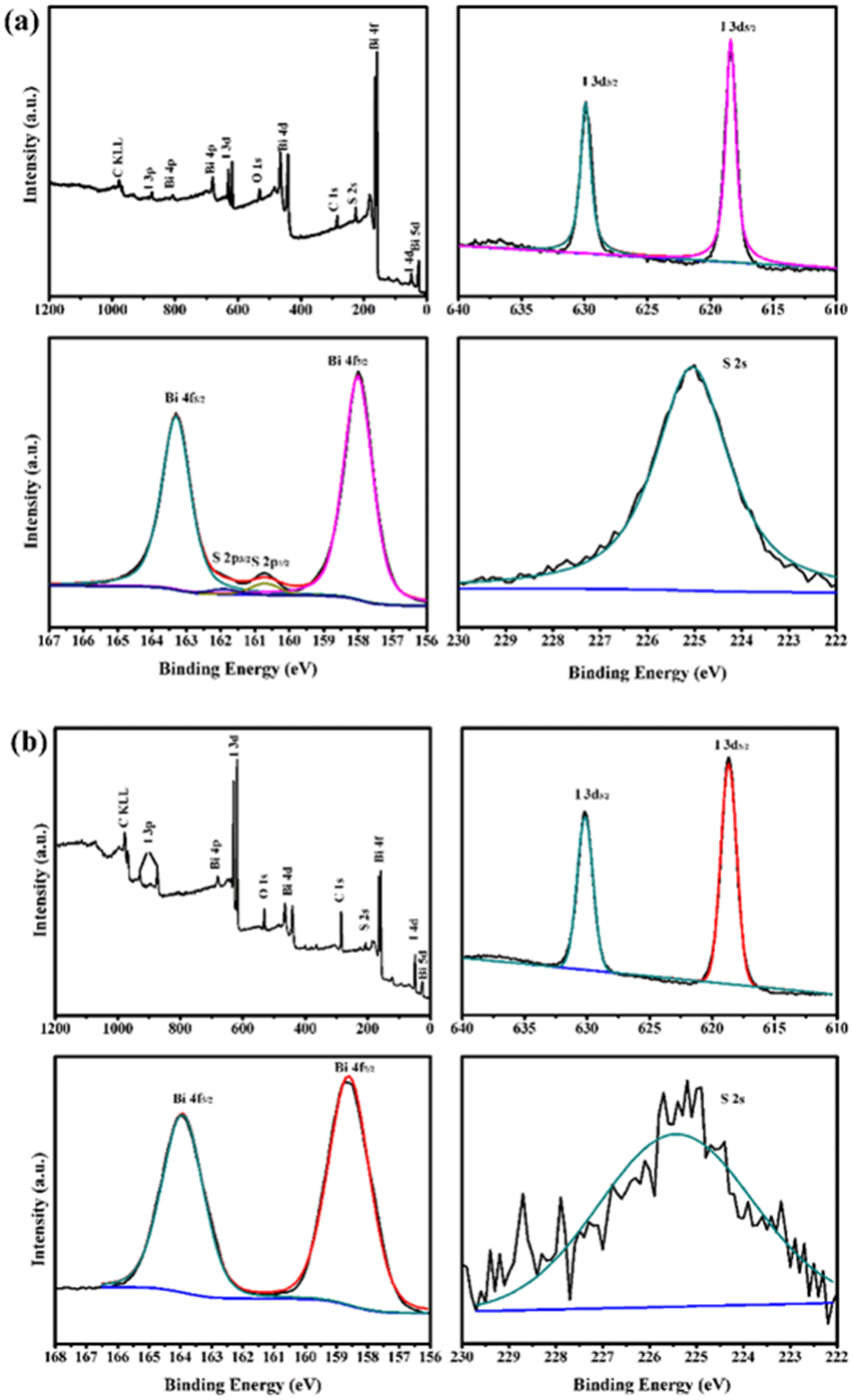

Figure 2.14 XPS survey spectra and high-resolution XPS scan spectra of (a) $Bi_{13}S_{18}I_2$ and (b) BiSI samples.

There is also an argument about $Bi_{13}S_{18}I_2$ is an indirect bandgap semiconductor or a direct bandgap semiconductor.[29, 30] These arguments suggest that the properties of $Bi_{13}S_{18}I_2$ are strongly dependent on its synthesis conditions, maybe slightly different in the chemical composites, due to formation of the bivalent $[Bi_2]^{4+}$ dimer. Therefore,

$Bi_{13}S_{18}I_2$ may be a tunable semiconducting material. On the other hand, the conduction band minimum of BiSI will be located at 0.68 eV above the fermi level because its bandgap energy is 1.57 eV. Therefore, BiSI should be also an n-type semiconductor because the Femi level was close to the conduction band minimum, which is agreement with the results reported.[4]

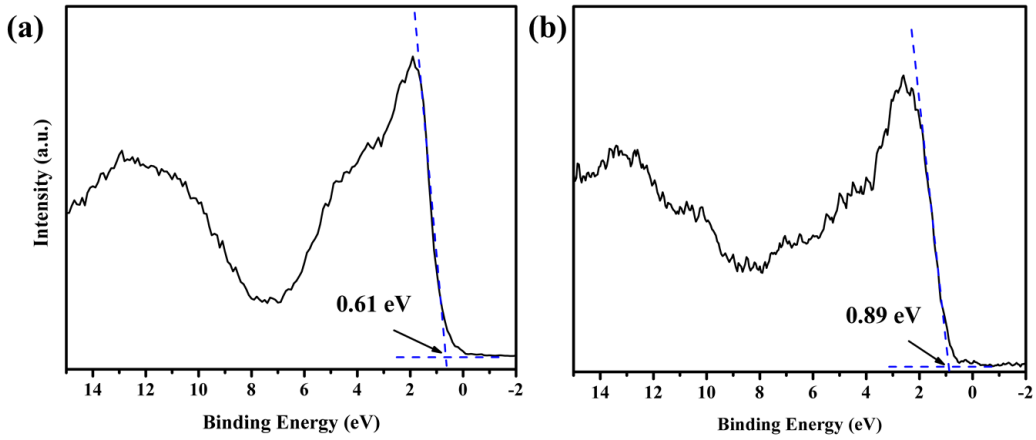

Figure 2.15 Valance-band XPS spectra of (a) $Bi_{13}S_{18}I_2$ and (b) BiSI.

Figure 2.15 shows the valance-band spectra of $Bi_{13}S_{18}I_2$ and BiSI. The valence band maximum is located at 0.61 and 0.89 eV below the Fermi level for $Bi_{13}S_{18}I_2$ and BiSI, respectively. Therefore, the conduction band minimum of $Bi_{13}S_{18}I_2$ will be located at 0.19 eV above the Fermi level because the band gap of $Bi_{13}S_{18}I_2$ is 0.80 eV. As the Femi level is close to the conduction band minimum, $Bi_{13}S_{18}I_2$ should be an n-type semiconductor.[43] This is different from the result that $Bi_{13}S_{18}I_2$ shows a p-type behavior reported by Ho et al. based on a Hot-probe measurement.[30] ported by Ho et al. based on a Hot-probe measurement.[30] The n-type and p-type semiconductors can be distinguished also by Mott-Schottky plot, where n-type semiconductor shows positive slope value and p-type semiconductor shows a negative slope value.[45] The Mott-Schottky plot of $Bi_{13}S_{18}I_2$ shows a positive slope value, as shown in Figure 2.16, namely it is an n-type semiconductor.

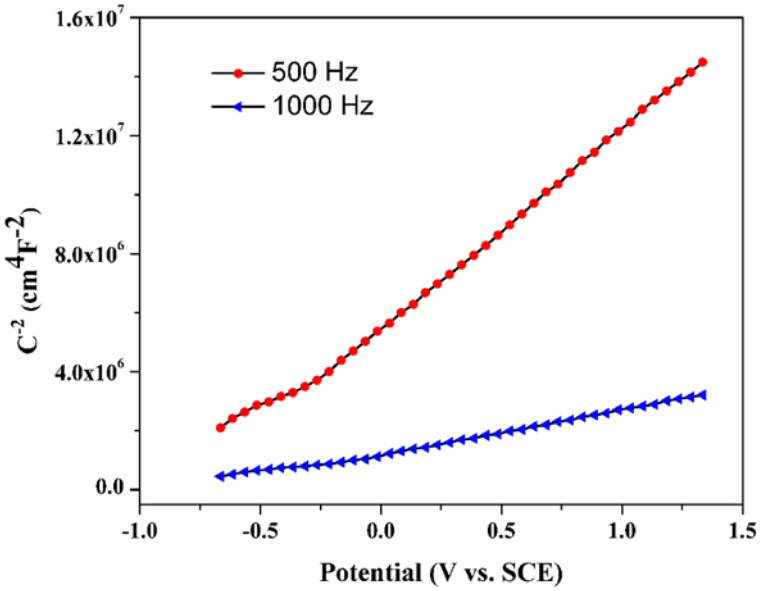

Figure 2.16 Mott-Schottky plot of $Bi_{13}S_{18}I_2$ with frequencies of 500 and 1000 Hz.

There is also an argument about $Bi_{13}S_{18}I_2$ is an indirect bandgap semiconductor or a direct bandgap semiconductor.[29, 30] These arguments suggest that the properties of $Bi_{13}S_{18}I_2$ are strongly dependent on its synthesis conditions, maybe slightly different in the chemical composites, due to formation of the bivalent $[Bi_2]^{4+}$ dimer. Therefore, $Bi_{13}S_{18}I_2$ may be a tunable semiconducting material. On the other hand, the conduction band minimum of BiSI will be located at 0.68 eV above the fermi level because its bandgap energy is 1.57 eV. Therefore, BiSI should be also an n-type semiconductor because the Femi level was close to the conduction band minimum, which is agreement with the results reported.[4]

2.3.3 Solar cell performance of $Bi_{13}S_{18}I_2$ as light absorber

$Bi_{13}S_{18}I_2$ holds much promise as a light absorber for solar cells because it exhibits strong light absorption in the whole visible light wavelength range as shown in Figure 2.13(a). However, to the best of our knowledge, no studies have reported on the use of $Bi_{13}S_{18}I_2$ as a light absorber for solar cells. Therefore, we carried out a preliminary PV study using $Bi_{13}S_{18}I_2$ as a light absorber to confirm its possibility. First, $Bi_{13}S_{18}I_2$ solar cells with a cell structure as shown in Figure 2.17 were fabricated. In the solar cell, a

TiO_2 dense film was coated on the surface of FTO conducting glass as a hole blocking layer and a TiO_2 porous film was coated on the TiO_2 dense film. A $Bi_{13}S_{18}I_2$ film was fabricated on the TiO_2 porous film through a modified solvothermal process. An electrolyte solution of I_3^-/I^- redox couple was used as the hole-transporting material and a Pt-coated FTO conducting glass was used as a counter-electrode similar to the dye-sensitized solar cells.

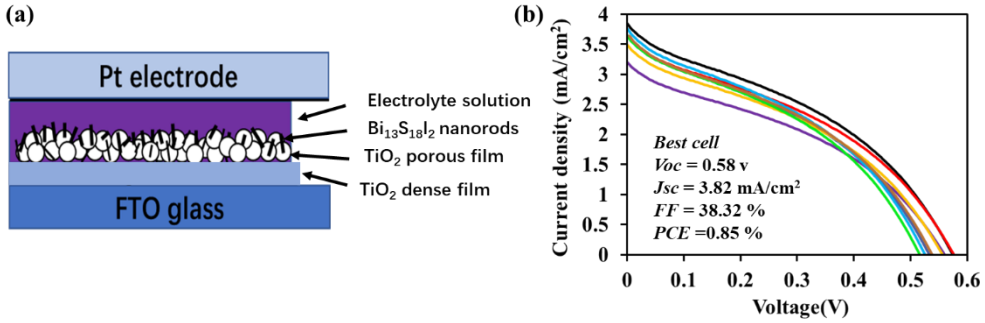

Figure 2.17 (a) Schematic diagram of $Bi_{13}S_{18}I_2$ solar cell structure and (b) I-V curves of eight $Bi_{13}S_{18}I_2$-based solar cells.

Table 2. PV performance parameters of 8 devices with architecture FTO/TiO2/$Bi_{13}S_{18}I_2$/Electrolyte solution/Pt under AM1.5G illumination.

Cell number	**Voc(V)**	**Jsc(mA/cm^2)**	**FF(%)**	**η(%)**
1	0.58	3.82	38.32	0.85
2	0.58	3.52	36.51	0.75
3	0.56	3.48	33.42	0.65
4	0.56	3.22	31.12	0.56
5	0.54	3.71	33.42	0.67
6	0.53	3.70	33.55	0.66
7	0.52	3.80	33.87	0.67
8	0.51	3.52	29.25	0.53

The FE-SEM images of FTO/TiO_2/$Bi_{13}S_{18}I_2$ electrodes reveal that the thickness of

the porous TiO_2 film is about 10 μm (Figure 2.18(a)). A uniform black $Bi_{13}S_{18}I_2$ film is formed on the porous TiO_2 film after solvothermal treatment (Figure 2.18(d)). Rod-like $Bi_{13}S_{18}I_2$ nanocrystals are formed in the nanopores and surface of the porous TiO_2 film (Figure 2.18(b, c)). The diameter of the $Bi_{13}S_{18}I_2$ nanorods in the nanopores was about 50 nm, which is slightly smaller than those on the surface, indicating that the crystal size in the nanopores is controlled by the pore size.

Figure 2.17 shows the photocurrent-voltage (*I-V*) characteristic curves of eight solar cells under simulated AM 1.5G spectrum. The cell performance parameters of energy conversion efficiency (η), short-circuit photocurrent density (J_{sc}), open-circuit voltage (V_{oc}), and fill factor (*FF*) evaluated from the *I-V* curves were summarised in Table 2. These cells exhibited η, J_{sc}, V_{oc}, and *FF* values in the ranges of 0.53 to 0.85 %, 3.22 to 3.82 mA/cm^2, 0.51 to 0.58 V, and 29.3 to 38.3 %, respectively. The relatively high repeatability of the cell performance can be attributed to the high stability of $Bi_{13}S_{18}I_2$. The highest η value is 0.85 % with cell parameters of J_{sc}=3.82 mA/cm^2, V_{oc}=0.58 V, and *FF*=38.3 %. Although the PCE of this preliminary solar cell is still low, these results reveal the potential of $Bi_{13}S_{18}I_2$ as a light absorber for photovoltaics and photo electronic devices. The low PCE can be attributed mainly to low J_{sc} and *FF* values of the cell. Many factors, such as the cell structure, the thickness of the $Bi_{13}S_{18}I_2$ and TiO_2 films, crystallinity of the $Bi_{13}S_{18}I_2$ can affect the J_{sc} and *FF* values. The optimization of these factors will further improve the solar cell performance. Moreover, the $Bi_{13}S_{18}I_2$ band gap of 0.80 eV is smaller than the ideal bandgap of 1.4 eV for a single p-n junction solar cell,[46] which also limits the maximum PCE value. To give the precise evaluation of the ultimate potential of $Bi_{13}S_{18}I_2$ as light absorber for the photovoltaics, the further detailed studies, such as the lifetime, photoluminescence quantum efficiency, and Urbach energy, are expected.

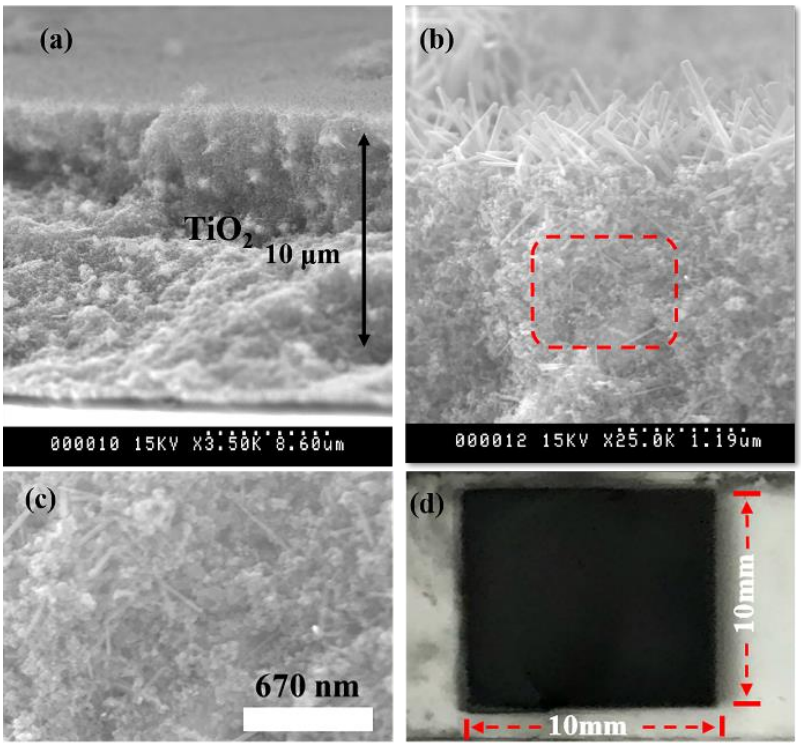

Figure 2.18 (a, b) Cross-sectional FE-SEM images, and (d) photograph of FTO/TiO_2/$Bi_{13}S_{18}I_2$ electrode. (c) is enlarge red square in (b).

2.4 Conclusions

The solvothermal process is a facile method for the synthesis of bismuth chalcogenide iodide compounds of $Bi_{13}S_{18}I_2$ and BiSI. The formations of $Bi_{13}S_{18}I_2$ and BiSI are strongly dependent on the S/Bi mole ratio, reaction temperature and solvent. BiSI can be formed under low S/Bi mole ratio conditions, but it is unstable and easily converts to $Bi_{13}S_{18}I_2$ under higher S/Bi mole ratio conditions. Both $Bi_{13}S_{18}I_2$ and BiSI have a similar rod-like crystal morphology due to their ribbon-like and chain structure. $Bi_{13}S_{18}I_2$ is an n-type semiconductor with a narrow bandgap of 0.80 eV. The strong light absorbance of $Bi_{13}S_{18}I_2$ in a wide wavelength range from UV to NIR suggests that it is a promising light absorber material for solar cells. Uniform $Bi_{13}S_{18}I_2$ nanorod film can be fabricated on the porous TiO_2 electrode by a modified solvothermal process. This

preliminary PV study produces a PCE of 0.85%, revealing the potential of the $Bi_{13}S_{18}I_2$ light absorber for a new type of solar cell that can be fabricated by low-cost solution process.

2.5 References

1. L. M. Peter, *Philos Trans A Math Phys Eng Sci*, 2011, **369**, 1840-1856.
2. W. Hermann, *Energy*, 2006, **31**, 1685-1702.
3. J. Peng, L. Lu and H. Yang, *Renewable and Sustainable Energy Reviews*, 2013, **19**, 255-274.
4. M. Powalla, S. Paetel, E. Ahlswede, R. Wuerz, C. D. Wessendorf and T. Magorian Friedlmeier, *Applied Physics Reviews*, 2018, **5**, 041602.
5. H. Morrow, 2010, DOI: 10.1002/0471238961.0301041303011818.a01.pub3.
6. M. A. Green, A. Ho-Baillie and H. J. Snaith, *Nature Photonics*, 2014, **8**, 506-514.
7. M. Gratzel, *Nat Mater*, 2014, **13**, 838-842.
8. NREL Efficiency Chart. This Plot is Courtesy of the National Renewable Energy Laboratory, Golden, CO. Available online: https://www.nrel.gov/pv/assets/pdfs/best-reserch-cell-e_ciencies.20190411.pdf (accessed on 14 April 2019).
9. L. Meng, J. You and Y. Yang, *Nat Commun*, 2018, **9**, 5265.
10. Z. Xiao, W. Meng, J. Wang and Y. Yan, *ChemSusChem*, 2016, **9**, 2628-2633.
11. Y. Zhang, J. Yin, M. R. Parida, G. H. Ahmed, J. Pan, O. M. Bakr, J. L. Bredas and O. F. Mohammed, *J Phys Chem Lett*, 2017, **8**, 3173-3177.
12. P. Wang, X. Zhang, Y. Zhou, Q. Jiang, Q. Ye, Z. Chu, X. Li, X. Yang, Z. Yin and J. You, *Nat Commun*, 2018, **9**, 2225.
13. L.-M. Wu, X.-T. Wu and L. Chen, *Coordination Chemistry Reviews*, 2009, **253**, 2787-2804.
14. A. Walsh, D. J. Payne, R. G. Egdell and G. W. Watson, *Chem Soc Rev*, 2011, **40**, 4455-4463.
15. F. Giustino and H. J. Snaith, *ACS Energy Letters*, 2016, **1**, 1233-1240.

16. Y. Y. Sun, J. Shi, J. Lian, W. Gao, M. L. Agiorgousis, P. Zhang and S. Zhang, *Nanoscale*, 2016, **8**, 6284-6289.
17. F. Bai, Y. Hu, Y. Hu, T. Qiu, X. Miao and S. Zhang, *Solar Energy Materials and Solar Cells*, 2018, **184**, 15-21.
18. K. Mistewicz, M. Nowak and D. Stroz, *Nanomaterials (Basel)*, 2019, **9**.
19. C. Deng, H. Guan and X. Tian, *Materials Letters*, 2013, **108**, 17-20.
20. L. Zhu, Y. Xie, X. Zheng, X. Yin and X. Tian, *Inorganic Chemistry*, 2002, **41**, 4560-4566.
21. H. Shi, W. Ming and M.-H. Du, *Physical Review B*, 2016, **93**.
22. A. M. Ganose, K. T. Butler, A. Walsh and D. O. Scanlon, *Journal of Materials Chemistry A*, 2016, **4**, 2060-2068.
23. H. Kunioku, M. Higashi and R. Abe, *Sci Rep*, 2016, **6**, 32664.
24. N. T. Hahn, A. J. E. Rettie, S. K. Beal, R. R. Fullon and C. B. Mullins, *The Journal of Physical Chemistry C*, 2012, **116**, 24878-24886.
25. D. Tiwari, F. Cardoso-Delgado, D. Alibhai, M. Mombrú and D. J. Fermín, *ACS Applied Energy Materials*, 2019, **2**, 3878-3885.
26. W. L. Huang and Q. Zhu, *J Comput Chem*, 2009, **30**, 183-190.
27. D. Arivuoli, F. D. Gnanam and P. Ramasamy, *Journal of Materials Science*, 1986, **21**, 2835-2838.
28. W. J. Fa, P. J. Li, Y. G. Zhang, L. L. Guo, J. F. Guo and F. L. Yang, *Advanced Materials Research*, 2011, **236-238**, 1919-1922.
29. R. Groom, A. Jacobs, M. Cepeda, R. Drummey and S. E. Latturner, *Chemistry of Materials*, 2017, **29**, 3314-3323.
30. C. H. Ho, Y. H. Chen, Y. K. Kuo and C. W. Liu, *Chem Commun (Camb)*, 2017, **53**, 3741-3744.
31. G. Shen, D. Chen, K. Tang, L. Huang and Y. Qian, *Journal of Crystal Growth*, 2003, **249**, 331-334.
32. Y. Chen, G. Tian, T. Feng, W. Zhou, Z. Ren, T. Han, Y. Xiao and H. Fu, *CrystEngComm*, 2015, **17**, 6120-6126.

33. Z. Wu, Y. Jiang, X. Xiong, S. Ding, Y. Shi, X. Liu, Y. Liu, Z. Huang and J. Hu, *Catalysis Science & Technology*, 2017, **7**, 3464-3468.
34. Y. Yan, Y. Xu, S. Lei, X. Ou, L. Chen, J. Xiong, Y. Xiao and B. Cheng, *Dalton Transactions*, 2018, **47**, 3408-3416.
35. C. Chen, G. A. Sewvandi, T. Kusunose, Y. Tanaka, S. Nakanishi and Q. Feng, *CrystEngComm*, 2014, **16**, 8885.
36. C. Chen, L. Xu, G. A. Sewvandi, T. Kusunose, Y. Tanaka, S. Nakanishi and Q. Feng, *Crystal Growth & Design*, 2014, **14**, 5801-5811.
37. Y. Zhou, L. Wang, S. Chen, S. Qin, X. Liu, J. Chen, D.-J. Xue, M. Luo, Y. Cao, Y. Cheng, E. H. Sargent and J. Tang, *Nature Photonics*, 2015, **9**, 409-415.
38. A. Audzijonis, R. Žaltauskas, R. Sereika, L. Žigas and A. Rėza, *Journal of Physics and Chemistry of Solids*, 2010, **71**, 884-891.
39. G. E. Jellison and F. A. Modine, *Applied Physics Letters*, 1996, **69**, 2137-2137.
40. M.-Y. K. Sang-An Park, Ji-Yong Lim, Byong-Seo Park, Jeong-Dae Koh, and Wea-Tek Kim, 1995.
41. M. A. Butler, *Journal of Applied Physics*, 1977, **48**, 1914-1920.
42. R. C. Newman, *Reports on Progress in Physics*, 1982, **45**, 1163-1210.
43. J. Grigas, E. Talik, M. Adamiec, V. Lazauskas and V. Nelkinas, *Journal of Electron Spectroscopy and Related Phenomena*, 2006, **153**, 22-29.
44. J. You, Z. Hong, Y. M. Yang, Q. Chen, M. Cai, T. B. Song, C. C. Chen, S. Lu, Y. Liu, H. Zhou and Y. Yang, *ACS Nano*, 2014, **8**, 1674-1680.
45. A. W. Bott, *Current Separations*, 1998, 87-91.
46. W. Shockley and H. J. Queisser, *Journal of Applied Physics*, 1961, **32**, 510-519.

Chapter III

Possibility of $Bi_{13}S_{18}X_2$-Based Solar Cells (X = Cl, Br, I): Photoelectric Behavior and Photovoltaic Performance

3.1 Introduction

Recently novel binary, ternary and quaternary compounds of non-toxic elements are becoming the protagonist for development of photoelectric materials.[1] Bismuth is a non-toxic element and also relatively low price element due to its quite abundant in the earth's crust.[2-5] Among the bismuth-based ternary compounds, Bi-VI-VII compounds have evoked an enormous interest as functional electronic materials owing to their interesting photoelectric, electromechanical, electrooptical, ferroelectric, piezoelectric, and electromechanical properties, and a large temperature dependence of the bandgap.[6-9] Bismuth oxyhalides (BiOX, where X = Cl, Br, I), possessing a layered structure, have drawn much attention as visible light response photocatalyst.[10-13] Furthermore, the bandgaps of their solid solutions, such as $BiOBr_xI_{1-x}$, can be changed continually with changing chemical compositions.[14, 15] Bismuth chalcogenide halides (BiSX, where X = Cl, Br, I) have great potential applications in visible light response photocatalysts and photovoltaics due to their attractive photoelectric performance.[7, 16, 17] BiSeX (X= Cl, Br, I) compounds exhibit a photoelectric response in the region from the visible to near infrared wavelength, suggesting possibility of photovoltaic applications.[18-20]

The Bi-VI-VII compounds are promising light absorber materials for photovoltaics because their similar properties to lead-based halide perovskites, i.e. Bi(III) and Pb(II) have the same stable electronic configuration of $d^{10}s^2p^0$, similar ionic radii and electronegativities.[18] In this sense, Bi-VI-VII compounds are expected alternatives for the lead-based halide perovskites as photovoltaic materials to solve the toxic and unstable problems of the lead-based halide perovskites in the perovskite solar

cells. In the Bi-VI-VII compounds, $Bi_{13}S_{18}X_2$ (X= Cl, Br, I) compounds are one of the most promising photovoltaic material due to their broad photoelectric responses in the region from the visible to near infrared wavelength. However, only limited studies have been reported on $Bi_{13}S_{18}X_2$ compounds because the stoichiometric $Bi_{13}S_{18}X_2$ compounds are difficult to be synthesized.

Traditionally, the bismuth chalcohalides are synthesized using a vapor transport process and flux process under high temperature condition over 600 ^oC.[21-24] Recently, syntheses of $Bi_{13}S_{18}X_2$ by employing solution processes have been reported. $Bi_{13}S_{18}I_2$ can be synthesized by solvothermal process.[25-27] $Bi_{13}S_{18}Br_2$ can be synthesized by hydrothermal and solvothermal processes.[28, 29] $Bi_{13}S_{18}Cl_2$ can be also obtained by using solvothermal route.[30] There are some arguments on the structures and chemical compositions of $Bi_{13}S_{18}X_2$ compounds. Miehe and Kupčík reported first study on $Bi_{13}S_{18}I_2$ compound in 1971 and concluded that it belongs to the hexagonal crystal system with the space group of $P6_3$ and a chemical formula of $Bi(Bi_2S_3)_9I_3$.[31] Other studies reported that $Bi_{13}S_{18}I_2$ compound belongs to the hexagonal system with space group of $P6_3/m$ or $P6_3$ and a chemical formula of $Bi_{19}S_{27}I_3$ or $(Bi(Bi_2S_3)_9I_3)_{2/3}$.[21, 32, 33] Recently, Groom et al. rediscovered the $Bi_{13}S_{18}I_2$ structure by single crystal XRD and powder synchrotron XRD, resulting in a stoichiometry of $Bi_{13}S_{18}I_2$ with space group of P3 due to formation of bivalent Bi(II) dimer of (Bi_2^{4+}) in this compound.[22] Lesser studies reported on $Bi_{13}S_{18}Br_2$ and $Bi_{13}S_{18}Cl_2$ compounds than that of $Bi_{13}S_{18}I_2$. These studies commonly resulted the hexagonal crystal system with the space group of $P6_3$ and chemical formulas of $Bi_{19}S_{27}Br_3$ and $Bi_{19}S_{27}Cl_3$, where all Bi are trivalence.[23, 24, 29, 34] Although the formations of Bi(II) dimer of (Bi_2^{4+}) in $Bi_{13}S_{18}Br_2$ and $Bi_{13}S_{18}Cl_2$ are also possible similar to $Bi_{13}S_{18}I_2$, but it is unclear.[22]

Another argument about $Bi_{13}S_{18}X_2$ is that it is a direct semiconductor or an indirect semiconductor.[21, 22] Yan et al. reported that $Bi_{13}S_{18}I_2$ shows a direct transition bandgap of 0.83 eV.[25] However, Groom et al. reported an indirect transition bandgap of 0.82 eV for $Bi_{13}S_{18}I_2$.[22] It has been reported that $Bi_{13}S_{18}Cl_2$ and $Bi_{13}S_{18}Br_2$ are direct semiconductors with bandgaps of 1.6 and 1.42 eV, respectively.[28, 30] Photoelectric studies revealed that $Bi_{13}S_{18}I_2$ demonstrates a broad photoelectric response ranging

from ultraviolet to near infrared wavelength and can be applied as light absorber for photodetector device with high stability and reproducibility.[25-27] In chapter II, we fabricated $Bi_{13}S_{18}I_2$-based solar cell by a solution process, demonstrating a power conversion efficiency (PCE) of 0.85%. Only a few of studies have reported on the photoelectric behavior of $Bi_{13}S_{18}Br_2$ and $Bi_{13}S_{18}Cl_2$ based on their visible light response photocatalytic performances.[28-30] To the best of our knowledge, no any study has been reported on $Bi_{13}S_{18}Br_2$- and $Bi_{13}S_{18}Cl_2$-based solar cells.

As described above, in this chapter, a detailed study on the photoelectric behavior of $Bi_{13}S_{18}X_2$ (X=Cl, Br, I) is necessary for the applications of $Bi_{13}S_{18}X_2$ compounds to photovoltaic and other photoelectric materials. Herein, we describe a solvothermal processes for the syntheses of $Bi_{13}S_{18}Cl_2$ and $Bi_{13}S_{18}Br_2$, and systematically characterized photoelectric behavior of $Bi_{13}S_{18}X_2$ as light absorbers for solar cells. We gave the evidences of $Bi_{13}S_{18}Cl_2$ and $Bi_{13}S_{18}Br_2$ adopting a similar structure as $Bi_{13}S_{18}I_2$ with space group of P3 and chemical formula of $Bi_{13}S_{18}X_2$ rather than previously reported space group of $P6_3$ and chemical formula of $Bi_{19}S_{27}X_3$ by Rietveld refinements of XRD results. $Bi_{13}S_{18}Cl_2$, $Bi_{13}S_{18}Br_2$ and $Bi_{13}S_{18}I_2$ are indirect n-type semiconductors, displaying a strong and broad light absorption in the range from ultraviolet to near-IR light with narrow bandgaps. Uniform $Bi_{13}S_{18}X_2$ thin films were fabricated using a facile PVD method for the first time for the fabrication of solar cells. The photovoltaic study demonstrated that $Bi_{13}S_{18}X_2$ compounds are promising light absorber for solar cells. $Bi_{13}S_{18}Br_2$ exhibits the best photovoltaic performance in $Bi_{13}S_{18}X_2$ compounds. This work opens up importance insights for development of non-toxic and low cost $Bi_{13}S_{18}X_2$-based solar cells.

3.2 Experimental

3.2.1 Sample Preparation

Synthesis of bismuth chalcogenide halides powder samples

CH_3NH_3I (MAI) was synthesized by reaction of methylamine (24 mL) with HI

solution (10 mL) at 0 ºC for 2 h in a rotary evaporator at 120 rpm, and then evaporated at 80 ºC. The precipitate was washed three times with ethanol and then diethyl ether at room temperature and then dried at 60 ºC for 24 h. CH_3NH_3Br (MABr) was synthesized by reaction of methylamine (27.86 mL) with HBr solution (40 mL) by similar manner to the case of MAI. For the synthesis of $Bi_{13}S_{18}Br_2$ powder sample, $BiBr_3$ (2 mmol), MABr (3 mmol), and a desired amount of CH_4N_2S were solvothermally treated in 5 mL of ethylene glycol solvent at a desire temperature for 12 h under stirring conditions. $Bi_{13}S_{18}I_2$ sample was synthesized by the same method using BiI_3, MAI, and CH_4N_2S as starting materials. $Bi_{13}S_{18}Cl_2$ sample was synthesized by solvothermal treatment of $BiCl_3$ (5 mmol) and a desired amount of CH_4N_2S in 5 mL of acetone solvent at a desired temperature for 12 h under stirring conditions. The obtained powder samples were filtered, washed with ethanol or acetone, and dried in a drying oven at 60 ºC for 12 h.

Fabrication of bismuth chalcogenide halides pellet samples

The synthesized bismuth chalcogenide halide powder samples were gently ground into fine powder. The powder samples were then pressed using a pellet press mold with a diameter of 10 mm at 30 MPa for 3 min. Subsequently, cold isostatic press treatment was employed on the pellet sample with a pressure of 200 MPa for 5 min to increase sample density. The thickness of the pellets was controlled at about 1 mm.

Fabrication of a TiO_2 electrode and $Bi_{13}S_{18}X_2$ films

The TiO_2 electrode was prepared in the following manner.[35] A fluorine-doped tin oxide (FTO) conducting glass plate was cleaned in distilled water and acetone by ultrasonication for 10 min, consecutively. Then the FTO glass plate was dipped in 0.1 M titanium tetraisopropoxide solution for 1 min and washed with distilled water and ethanol, dried at room temperature, and calcined at 480 ºC for 1 h to coat the FTO glass surface with a dense TiO_2 thin film. A desired amount of $Bi_{13}S_{18}X_2$ bulk sample was transferred into a tungsten basket attached to copper feedthroughs inside a thermal evaporator (Vacuum Device, VE-2012). TiO_2 electrode was placed at 7 cm below the tungsten basket. After vacuum of 2×10^{-5} Pa was established, an electric current of 20 A was applied and kept for about 5 min evaporation time. Then, $Bi_{13}S_{18}X_2$-deposited TiO_2

electrodes were transferred to a furnace and heated in N_2 atmosphere at a desired temperature for 12h. The thickness of $Bi_{13}S_{18}X_2$ thin film was estimated from added $Bi_{13}S_{18}X_2$ amount and the distance between the tungsten basket and the TiO_2 electrode. The broken $Bi_{13}S_{18}X_2$ pellet was used for bulk sample.

Fabrication and characterization of solar cells

$Bi_{13}S_{18}X_2$-solar cells were comprised of the $Bi_{13}S_{18}X_2$-coated TiO_2 electrode as an anode, Pt-coated FTO glass as a cathode, and an electrolyte solution between the anode and the cathode. The electrolyte solution contained 0.1 M LiI, 0.01 M I_2, 0.6 M 1-butyl-3-n-propylimidazolium iodide (BMII), 0.4 M 4-tert-butylpyridine (TBP), and 0.1 M guanidine thiocyanate (GT) in a mixed solvent of acetonitrile and valeronitrile (v/v= 85:15). The photocurrent–voltage characteristic curves for the $Bi_{13}S_{18}X_2$-based solar cells were measured using a Hokuto-Denko BAS100B electrochemical analyzer under irradiation with AM 1.5 simulated sunlight (100 mW/cm^2), using a sunlight simulator (Yamashita Denso, YSS-E40). A light-passing mask was fixed on the surface of the FTO glass of the anode to set the effective irradiation area on the cell at 0.25 cm^2.

3.2.2 Physical analysis

The crystal structures of the samples were investigated using a powder X-ray diffractometer (Shimadzu, model XRD-6100) with Cu Kα (l = 0.1542 nm) radiation. The morphologies of the samples were observed using a field emission scanning electron microscopy (FE-SEM) (JEOL, ISM-7001F) and their chemical compositions were measured using an energy dispersive X-ray spectrometer (EDX) attached to the FE-SEM at an accelerating voltage of 15 kV. Transmission electron microscopy (TEM) and high-resolution TEM (HR-TEM) observations were performed on a JEOL Model JEM-3010 system at 300 kV. Atomic force microscope (AFM) images were acquired in contact mode on a Dimensions Hybrid Nanoscope system (NanoTechnology, SPA-400/Nano Navi Station, SII). Mott–Schottky plots were measured using an electrochemical analyzer (Shanghai Chenhua, CHI660E). Ultraviolet-visible-near infrared (UV-Vis-NIR) absorption spectra were obtained on a Shimadzu SolidSpec-

3700 UV-Vis-NIR Spectro-photometer at room temperature. The TG-DTA analysis was carried out using a thermal analyzer (Shimadzu, DTG-60H) at a heating rate of 10 $^{o}C \cdot min^{-1}$. For the conductivity measurement, a voltage of 100 V was applied to the $Bi_{13}S_{18}X_2$ pellet samples, and the current was measured using a ferroelectric testing system (Toyo Corporation, FCE3-4KVSYS) at room temperature. X-ray photoelectron spectroscopy (XPS) was performed using a Kratos Axis Supra X-ray photo-electron spectrometer. The XPS spectra were calibrated to an adventitious carbon peak at 284.8 eV. All the binding energy (BE) values were calibrated by the C 1s peaks at 284.6 eV of the surface adventitious carbon. Ultraviolet photoelectron spectroscopy (UPS) was carried out using a Thermo Fisher ESCALAB 250Xi with helium lamp radiation (21.22 eV) as excitation source, and Fermi level was calibrated by Au. The relationship of work function (Φ), lamp radiation ($h\nu$), second electron cutoff energy (E_{Cutoff}), and Fermi energy (E_F) can be illustrated using equation (1):

$$\Phi = h\nu - (E_{Cutoff} - E_F) \quad (1)$$

Where $\Phi = E_{vac}$ (vacuum level) - E_F, therefore, E_F can be evaluated from hν and E_{Cutoff}. (Φ).[36]

3.3 Results and discussion

3.3.1 Solvothermal synthesis of bismuth chalcogenide halide compounds

In chapter II, we have developed a solvothermal reaction system of BiI_3-CH_4N_2S-MAI in ethylene glycol solvent for synthesis of $Bi_{13}S_{18}I_2$. In the present study, a solvothermal reaction system of $BiBr_3$-CH_4N_2S-MABr in ethylene glycol solvent was used for synthesis of $Bi_{13}S_{18}Br_2$ and a solvothermal reaction system of $BiCl_3$-CH_4N_2S in acetone solvent was used for the synthesis of $Bi_{13}S_{18}Cl_2$. Similar to case of $Bi_{13}S_{18}I_2$, the formations of the products are strongly dependent on the mole ratios of starting materials and reaction temperature. Figure 3.1 shows the XRD patterns of products synthesized using the solvothermal reaction system of $BiBr_3$-CH_4N_2S-MABr, where the

$BiBr_3$/MABr mole ratio was fixed at 2:3. Based on the XRD results, a phase diagram for $BiBr_3$-CH_4N_2S-MABr solvothermal reaction system was obtained, as shown in Figure 3.3(a). Single phase of $Bi_{13}S_{18}Br_2$ is preferably formed in a S/Bi mole ratio range of 0.5 to 3 and higher temperature than 140 ºC (Figure 3.3(a)-Area-A). The $Bi_{13}S_{18}Br_2$ with highest crystallinity can be obtained at 200 ºC and S/Bi mole ratio of 2. Bi_2S_3 phase (JCPDS File No. 17-0320) is formed under the conditions of higher S/Bi mole ratio than 3 and higher temperature than 160 ºC (Figure 3.3(a)-Area-B). The formation of a small amount of BiOBr phase was observed at lower temperature than 150 ºC (Figure 3.3(a)-Area-C). $BiBr_3$-CH_4N_2S-MABr solvothermal reaction system is different from BiI_3-CH_4N_2S-MAI system. BiSI phase is formed in BiI_3-CH_4N_2S-MAI system but without BiSBr phase is formed in $BiBr_3$-CH_4N_2S-MABr system. This result suggests that $Bi_{13}S_{18}Br_2$ phase is more stable than $Bi_{13}S_{18}I_2$ phase.

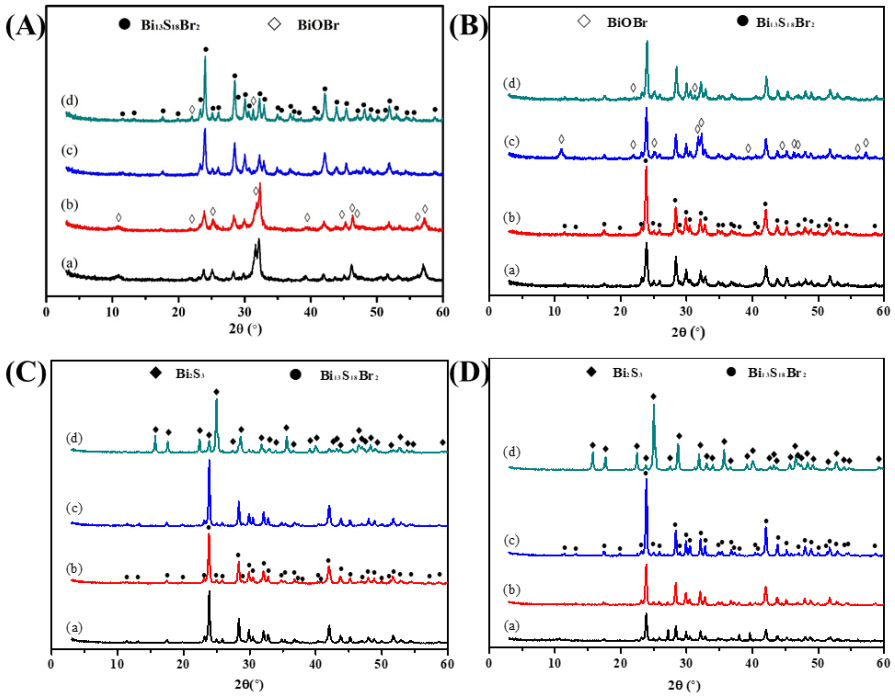

Figure 3.1 XRD patterns of products obtained by $BiBr_3$-CH_4N_2S-MABr solvothermal reaction system with CH_4N_2S/$BiBr_3$/MABr mole ratios of (a) 1:2:3, (b) 2:2:3, (c) 4:2:3 and (d) 8:2:3 , respectively, in ethylene glycol solvent at (A) 130, (B) 150, (C) 170 and (D) 200ºC for 12h, respectively.

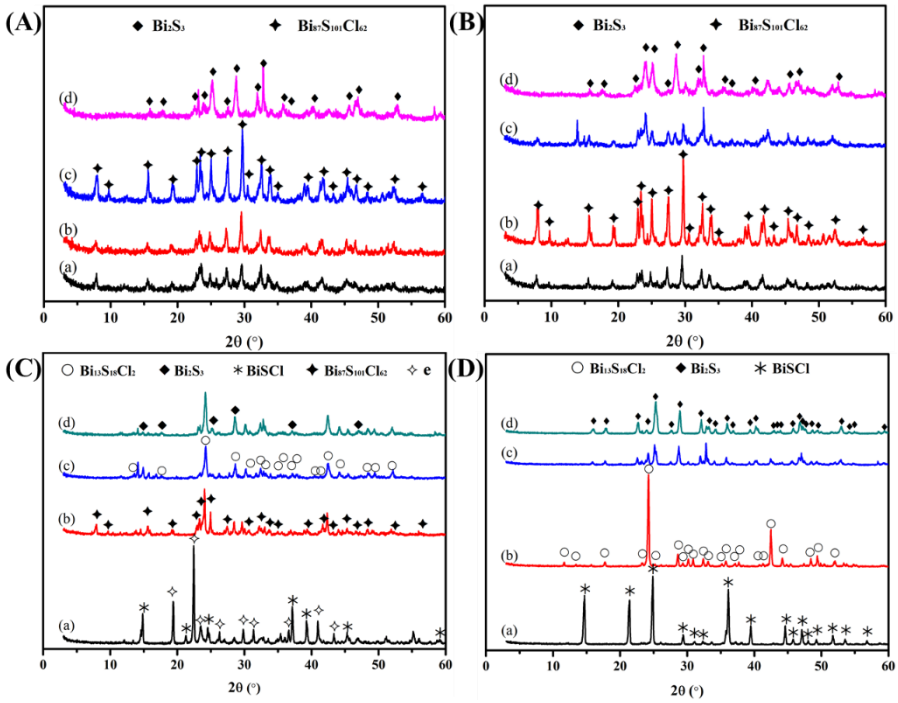

Figure 3.2 XRD patterns of products obtained by CH_4N_2S-$BiCl_3$ solvothermal system with $CH_4N_2S/BiCl_3$ mole ratios of (a) 2:5, (b) 4:5, (c) 8:5 and (d) 16:5, respectively, in acetone solvent at (A) 140, (B) 160, (C) 180, and (D) 200 °C for 12h, respectively.

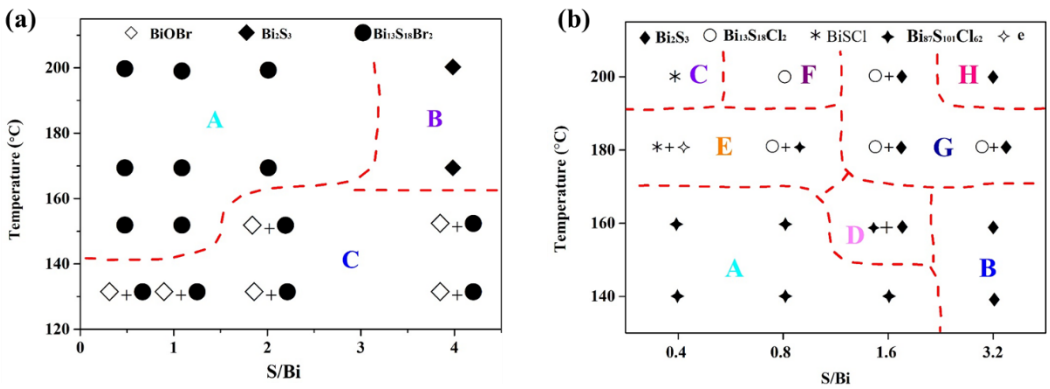

Figure 3.3 Phase diagrams for (a) $BiBr_3$-CH_4N_2S-MABr solvothermal reaction system in ethylene glycol solvent and (b) $BiCl_3$-CH_4N_2S solvothermal reaction system in acetone solvent.

$Bi_{13}S_{18}Cl_2$ cannot be obtained by using a solvothermal reaction system of $BiCl_3$-CH_4N_2S-MACl. Therefore, a new solvothermal reaction system of $BiCl_3$-CH_4N_2S in acetone solvent was developed to synthesize $Bi_{13}S_{18}Cl_2$. Figure 3.2 exhibits the XRD patterns of products synthesized using the solvothermal reaction system. A phase diagram based on the XRD results for $BiCl_3$-CH_4N_2S reaction system reveals that

$Bi_{13}S_{18}Cl_2$ single phase can be obtained in the limited conditions of S/Bi mole ratio around 0.8 and above 180 ºC (Figure 3.3(b)-Area-F), suggesting $Bi_{13}S_{18}Cl_2$ phase is more unstable than $Bi_{13}S_{18}Br_2$ and $Bi_{13}S_{18}I_2$ phase. BiSCl phase (JCPDS File No. 44-0255) is formed at S/Bi mole ratio of 0.4 above 180 ºC (Figure 3.3(b)-Area-C), and Bi_2S_3 phase is formed under the conditions of higher S/Bi mole ratio than 1.6 (Figure 3.3(b)-Area-B, G, H). A new phase was confirmed under the conditions of lower S/Bi mole ratio than 1.6 and lower temperature than 160 ºC (Figure 3.3(b)-Area-A). A EDS analysis result (Figure 3.4) indicated that this new phase has a chemical composition of $Bi_{87}S_{101}Cl_{62}$.

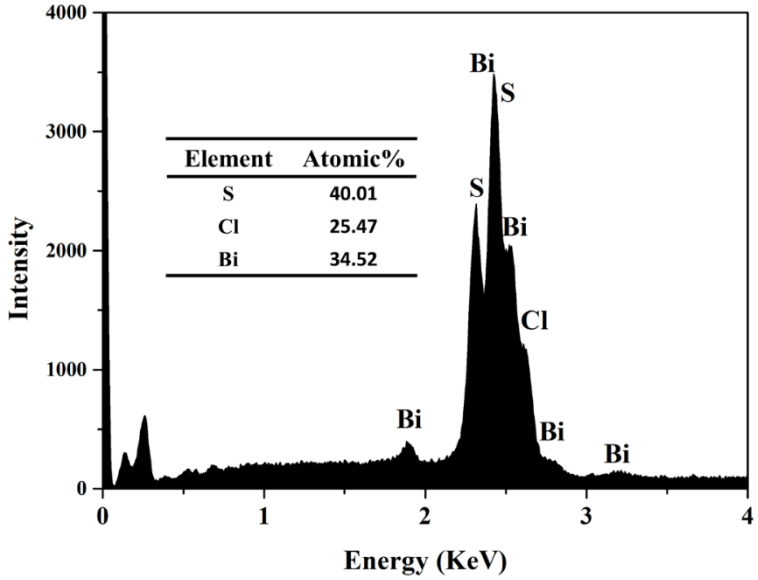

Figure 3.4 EDS spectrum of new phase synthesized by CH_4N_2S-$BiCl_3$ solvothermal system with $CH_4N_2S/BiCl_3$ mole ratios of 4:5 at 160 ºC for 12h. The insert table shows an analysis result of atonic percentages.

The morphologies of the products prepared at 200 ºC were investigated by using FE-SEM, as shown in Figure 3.5. The samples of $Bi_{13}S_{18}Br_2$ obtained at S/Bi mole ratio of 4:2 (Figure 3.5(c)) and $Bi_{13}S_{18}Cl_2$ obtained at S/Bi mole ratio of 5:4 (Figure. 3.5(f)) possess homogeneous fibrous morphologies with a diameter of about 100 nm and a length of about 10 μm, which are similar to $Bi_{13}S_{18}I_2$ with a rod-like morphology in chapter II. the BiSCl also has fibrous morphology similar to BiSI (Figure 3.5(e)). Furthermore, the Bi_2S_3 crystals synthesized by these three solvothermal reaction

systems shows similar fibrous and rod-like particle morphologies (Figure 3.5 (d) and (h)).

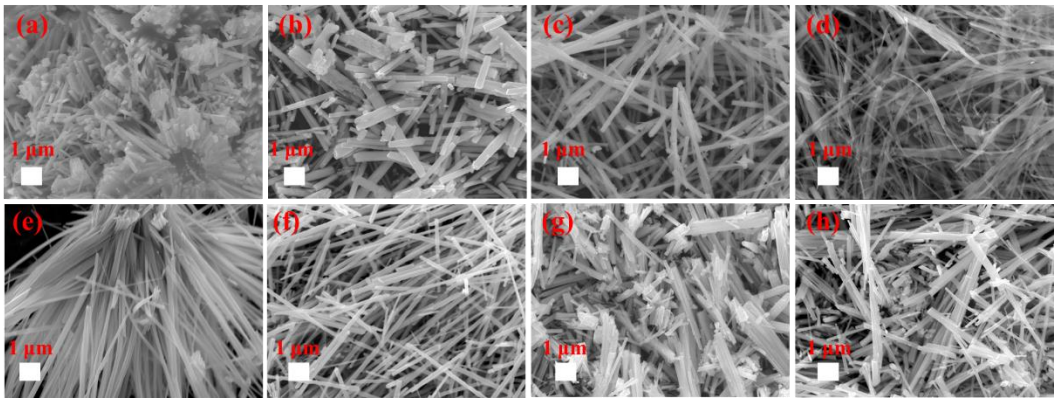

Figure 3.5 FE-SEM images of products synthesized by CH_4N_2S-BiI_3-MABr solvothermal reaction system in ethylene glycol solvent with CH_4N_2S/BiI_3/MABr mole ratio of (a) 1:2:3, (b) 2:2:3, (c) 4:2:3 and (d) 8:2:3 at 200 ºC for 12h, respectively; and the products synthesized by CH_4N_2S-BiI_3 solvothermal reaction system in acetone solvent with CH_4N_2S/BiI_3 mole ratio of (e) 2:5, (f) 4:5, (g) 8:5 and (h) 16:5 at 200 ºC for 12h, respectively.

The thermostabilities of $Bi_{13}S_{18}X_2$ was investigated using TG-DTA, as shown in Figure 3.6(a) ~ (c). The $Bi_{13}S_{18}I_2$ is stable up to 350 ºC, decomposes to BiOI at around 380 ºC, and then to Bi_2O_3 at over 500 ºC (Chapter II). $Bi_{13}S_{18}Cl_2$ and $Bi_{13}S_{18}Br_2$ exhibit similar TG-DTA curves. The first tiny mass losses with exothermic peaks around 230 and 280 ºC for $Bi_{13}S_{18}Cl_2$ and $Bi_{13}S_{18}Br_2$, respectively, can be attributed to the decomposition of organic compounds absorbed on the particle surface. The large mass losses with exothermic peaks around 435 and 460 ºC correspond to destructions of $Bi_{13}S_{18}Cl_2$ and $Bi_{13}S_{18}Br_2$ accompanying formation of BiOCl and $Bi_{24}O_{31}Br_{10}$, respectively. The mass losses above 600 ºC can be attributed to decompositions of BiOCl and $Bi_{24}O_{31}Br_{10}$ to Bi_2O_3 (Figure 3.6(d)). The results reveal that thermostabilities of $Bi_{13}S_{18}X_2$ increase in an order of $Bi_{13}S_{18}I_2 < Bi_{13}S_{18}Cl_2 < Bi_{13}S_{18}Br_2$.

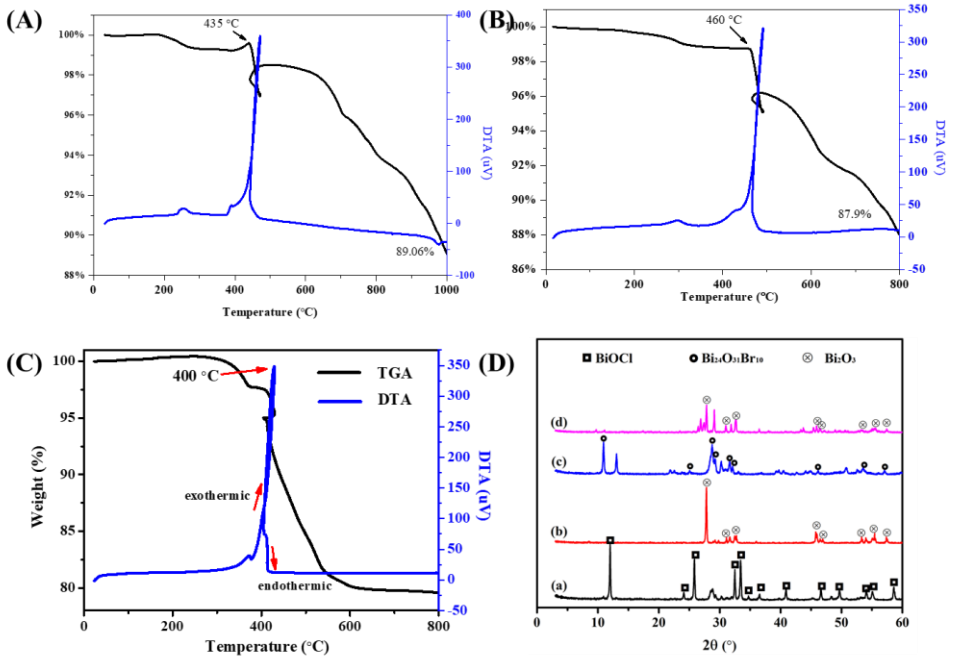

Figure 3.6 TGA-DTA curves for (A) $Bi_{13}S_{18}Cl_2$, (B) $Bi_{13}S_{18}Br_2$ and (C) $Bi_{13}S_{18}I_2$ samples. (D) XRD patterns of $Bi_{13}S_{18}Cl_2$ sample after heated at (a) 440 °C and (b) 600 °C, and $Bi_{13}S_{18}Br_2$ sample after heated at (c) 460 °C and (d) 600 °C for 4 h, respectively.

3.3.2 Structure of bismuth chalcogenide halide compounds

The structure of $Bi_{13}S_{18}I_2$ was initially reported as a hexagonal system with space group of $P6_3$ and composition formula of $Bi(Bi_2S_3)_9I_3$ in 1971.[31] Thereafter, some studies also reported that the $Bi_{13}S_{18}I_2$ belongs to hexagonal system with space group of $P6_3/m$ or $P6_3$ and composition formula of $Bi_{19}S_{27}I_3$ that is same as $Bi(Bi_2S_3)_9I_3$, where all Bi are trivalent Bi(III).[25, 32, 33, 37] Recently, Groom et. rediscovered the structure by studying the single crystal and proved a hexagonal system with space group of P3 rather than $P6_3$ or $P6_3/m$ and a composition formula of $Bi_{13}S_{18}I_2$ rather than $Bi_{19}S_{27}I_3$. Bi(III) and Bi(II) coexist in $Bi_{13}S_{18}I_2$ as $(Bi^{3+})_{12}(Bi_2^{4+})_{0.5}(S^{2-})_{18}(I^-)_2$ where bivalent Bi(II) dimer of (Bi_2^{4+}) is formed.[22] Kramer firstly reported $Bi_{13}S_{18}Br_2$ and its structure similar to $Bi_{13}S_{18}I_2$, hexagonal system with space group of $P6_3$ and composition of the formula of $Bi(Bi_2S_3)_9Br_3$ in 1976.[34, 37] $Bi_{13}S_{18}Br_2$ with space group of $P6_3/m$ and composition formula of $Bi_{19}S_{27}Br_3$ has been reported also.[28, 29, 38] Only a few studies have been reported on $Bi_{13}S_{18}Cl_2$ and suggested that $Bi_{13}S_{18}Cl_2$ belongs to hexagonal system with

space group of $P6_3$ or $P6_3/m$ similar to $Bi_{13}S_{18}Br_2$.[24, 30, 39, 40] We think the formation of Bi(II) dimer (BI_2^{4+}) is also possible in $Bi_{13}S_{18}Br_2$ and $Bi_{13}S_{18}Cl_2$ similar to $Bi_{13}S_{18}I_2$. Therefore, space group of P3 and compositions of $(Bi^{3+})_{12}(Bi_2^{4+})_{0.5}(S^{2-})_{18}(X^-)_2$ (X = Br and Cl) are also possible, which inspired us to refine the structures of $Bi_{13}S_{18}X_2$.

The structures of $Bi_{13}S_{18}X_2$ were refined by using Rietveld profile refinement method for two space groups of P3 and $P6_3$, respectively, and the results are shown in Table 1. Since fractional atonic coordinates for $Bi_{13}S_{18}Br_2$ and $Bi_{13}S_{18}Cl_2$ with space group of $P6_3/m$ has not been reported, $P6_3/m$ was not used in the structural refinements. The structure models for $Bi_{13}S_{18}Br_2$ and $Bi_{13}S_{18}Cl_2$ with space group of P3 were built on the basis of fractional atomic coordinate of $Bi_{13}S_{18}I_2$ by substituting I^- lattice positions with Br^- and Cl^-, respectively, because the fractional atomic coordinate for $Bi_{13}S_{18}Cl_2$ and $Bi_{13}S_{18}Br_2$ with space group of P3 were not included in the crystal structure database. Rietveld refinement results revealed that the space group of P3 give much less weighted profile residual errors (R_{wp}) and expected weighted profile factor (R_{exp}) for $Bi_{13}S_{18}Cl_2$, $Bi_{13}S_{18}Br_2$, and $Bi_{13}S_{18}I_2$ than those of space group of $P6_3$. Overall chi-square ($\chi^2=(R_{wp}/R_{exp})^2$) were 1.550, 1.910, and 1.402 for $Bi_{13}S_{18}Cl_2$, $Bi_{13}S_{18}Br_2$ and $Bi_{13}S_{18}I_2$ with space group of P3, respectively. The small R_{wp} and R_p values correspond high quality of the refinement fitting results.[41] Usually Rietveld refinement results are reliable when $R_{wp} < 10\%$ and χ^2 between 1 and 2%.[42] Therefore, we can conclude that the structures of $Bi_{13}S_{18}X_2$ belong to the hexagonal system with space group of P3 because the R-values for space group of P3 are less than those for space group of $P6_3$ and satisfy that conditions of $R_{wp} < 10\%$ and χ^2 = 1-2%. Rietveld fitting results using space group of P3 are shown in Figure 3.7. The plots of difference between XRD date and refined results indicates excellent fitting using space group of P3. The refined structural parameters including the atomic positions are provided in Table 2-4.

Table 1. Refined structure parameters and R-factors for $Bi_{13}S_{18}X_2$ using space groups of P3 and $P6_3$, respectively.

Formula	Space group	Lattice parameters	Cell volume (Å^3)	R-factors (%)	χ2
$Bi_{13}S_{18}Cl_2$	P3	a=b=15.4081(4)	825.058(48)	Rwp=9.921	1.550
		c=4.0128 (1)		Rp=6.362	
		α=β=90° γ = 120°		Rexp=7.661	
$Bi_{19}S_{27}Cl_3$	$P6_3$	a=b=15.4057(4)	823.395(50)	Rwp=12.723	1.999
		c=4.009 (1)		Rp=9.746	
		α=β=90° γ = 120°		Rexp=6.366	
$Bi_{13}S_{18}Br_2$	P3	a=b=15.5074(1)	835.759(50)	Rwp=8.390	1.910
		c=4.0130(1)		Rp=6.160	
		α=β=90° γ = 120°		Rexp=4.370	
$Bi_{19}S_{27}Br_3$	$P6_3$	a=b=15.5047(3)	835.363(43)	Rwp=13.419	3.075
		c=4.0125 (1)		Rp=10.390	
		α=β=90° γ = 120°		Rexp=4.364	
$Bi_{13}S_{18}I_2$	P3	a=b=15.6421(1)	851.935(14)	Rwp=9.052	1.402
		c=4.0205 (1)		Rp=6.794	
		α=β=90° γ = 120°		Rexp=6.458	
$Bi_{19}S_{27}I_3$	$P6_3$	a=b=15.6412(3)	851.781(33)	Rwp=11.877	1.838
		c=4.0203 (1)		Rp=9.029	
		α=β=90° γ = 120°		Rexp=6.460	

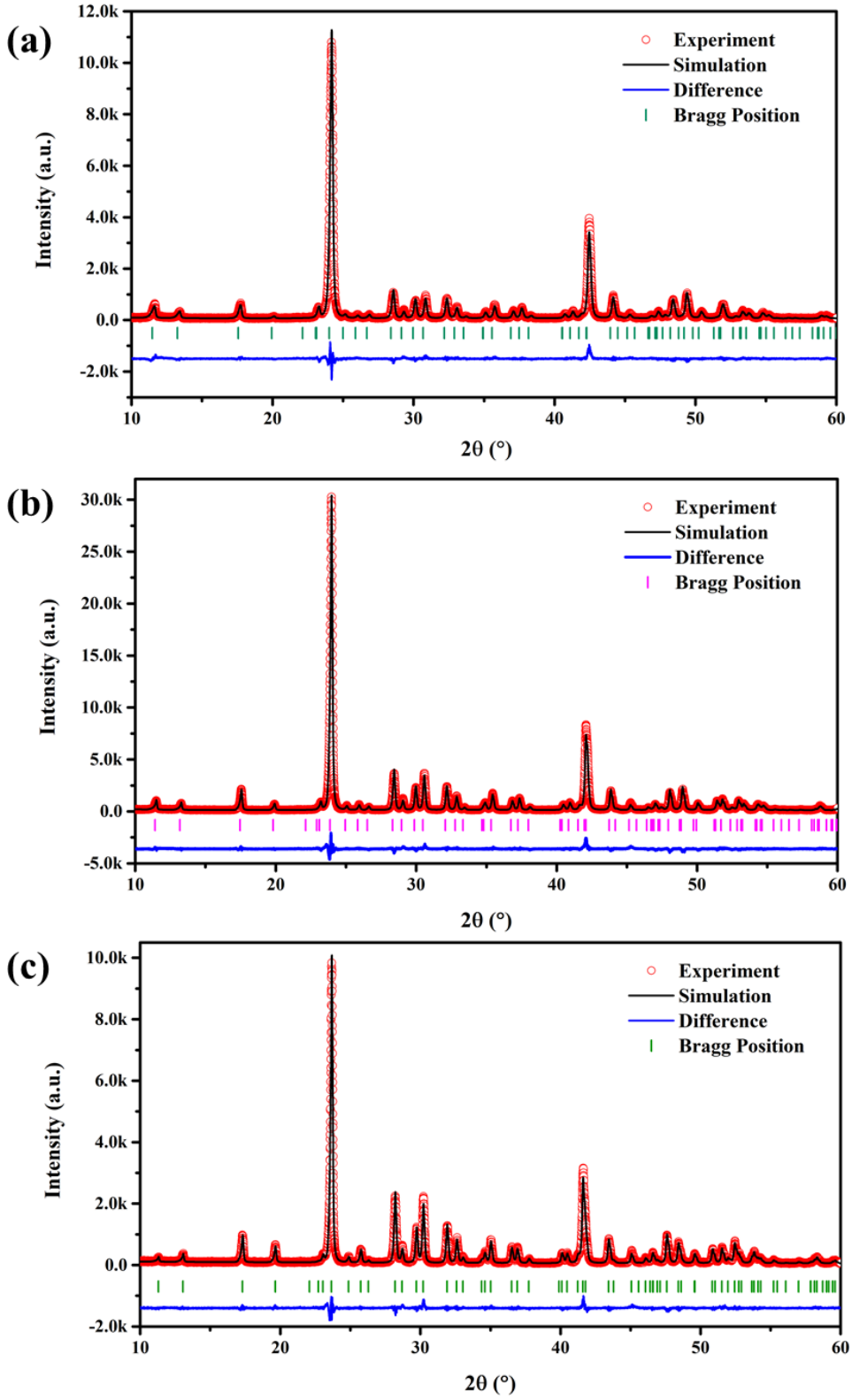

Figure 3.7 XRD patterns and Rietveld refinement fitting results for (a) $Bi_{13}S_{18}Cl_2$, (b) $Bi_{13}S_{18}Br_2$ and (c) $Bi_{13}S_{18}I_2$ using hexagonal system with space group of P3.

Table 2. Fractional atomic coordinates and equivalent isotropic displacement parameters for $Bi_{13}S_{18}Cl_2$ structure with space group P3 from structural refinement using fine scan XRD data.

	x	y	z	B	Occupancy
Bi(II)1	0.333333	0.666667	0.9266	0.465(67)	0.25
Bi(II)2	0.333333	0.666667	0.1721	0.465(67)	0.25
Bi(II)3	0.333333	0.666667	0.3860	0.465(67)	0.25
Bi(II)4	0.333333	0.666667	0.6309	0.465(67)	0.25
Bi(III)1	0.81776(43)	0.28280(34)	0.29(3)	0.465(67)	1
Bi(III)2	0.85869(48)	0.06179(34)	0.78(3)	0.465(67)	1
Bi(III)3	0.08708(50)	0.35982(35)	0.73(3)	0.465(67)	1
Bi(III)4	0.38433(36)	0.43217(32)	0.26(3)	0.465(67)	1
Cl1	0.6666667	0.3333333	0.97(3)	0.2(12)	1
Cl2	0	0	0.83(3)	0.2(12)	1
S1	0.2025(21)	0.2774(22)	0.45(3)	0.20(29)	1
S2	0.1542(16)	0.5245(16)	0.26(3)	0.20(29)	1
S3	0.3105(17)	0.4526(17)	0.75(3)	0.20(29)	1
S4	0.9486(22)	0.4271(25)	0.79(3)	0.20(29)	1
S5	0.7254(17)	0.1160(20)	0.80(3)	0.20(29)	1
S6	0.9440(17)	0.2183(23)	0.28(3)	0.20(29)	1

Table 3. Fractional atomic coordinates and equivalent isotropic displacement parameters for $Bi_{13}S_{18}Br_2$ structure with space group P3 from structural refinement using fine scan XRD data.

	x	y	z	B	Occupancy
Bi(II)1	0.333333	0.666667	0.92658	1.000(63)	0.25
Bi(II)2	0.333333	0.666667	0.1721	1.000(63)	0.25
Bi(II)3	0.333333	0.666667	0.38604	1.000(63)	0.25
Bi(II)4	0.333333	0.666667	0.63088	1.000(63)	0.25
Bi(III)1	0.82025(37)	0.28285(30)	0.31(1)	1.000(63)	1
Bi(III)2	0.85442(35)	0.06226(30)	0.82(1)	1.000(63)	1
Bi(III)3	0.09410(46)	0.36613(37)	0.82(1)	1.000(63)	1
Bi(III)4	0.38289(34)	0.42659(40)	0.30(1)	1.000(63)	1
Br1	0.6666667	0.3333333	0.85(14)	0.30(33)	1
Br2	0	0	0.46(1)	0.30(33)	1
S1	0.2056(15)	0.2754(20)	0.38(1)	0.20(21)	1
S2	0.1586(11)	0.5285(13)	0.33(1)	0.20(21)	1
S3	0.3197(13)	0.4559(13)	0.84(1)	0.20(21)	1
S4	0.9481(19)	0.4231(18)	0.82(1)	0.20(21)	1
S5	0.7249(17)	0.1165(19)	0.83(1)	0.20(21)	1
S6	0.9534(15)	0.2150(21)	0.33(1)	0.20(21)	1

Table 4. Fractional atomic coordinates and equivalent isotropic displacement parameters for $Bi_{13}S_{18}I_2$ structure with space group P3 from structural refinement using fine scan XRD data.

	x	y	z	B	Occupancy
Bi(II)1	0.333333	0.666667	0.92658	0.2040	0.25
Bi(II)2	0.333333	0.666667	0.1721	0.4674	0.25
Bi(II)3	0.333333	0.666667	0.38604	0.4731	0.25
Bi(II)4	0.333333	0.666667	0.63088	0.2047	0.25
Bi(III)1	0.82205(76)	0.27948(58)	0.27(1)	0.8524	1
Bi(III)2	0.84527(80)	0.05952(60)	0.78(1)	0.9790	1
Bi(III)3	0.09539(67)	0.37094(87)	0.79(1)	0.9805	1
Bi(III)4	0.38695(81)	0.42347(73)	0.27(1)	0.9862	1
I1	0.6666667	0.3333333	0.77(1)	0.2047	1
I2	0	0	0.34(1)	0.5175	1
S1	0.2043(46)	0.2780(51)	0.35(1)	0.2047	1
S2	0.1467(48)	0.5026(57)	0.27(1)	0.2047	1
S3	0.3088(58)	0.4783(48)	0.82(1)	0.2047	1
S4	0.9448(49)	0.4112(49)	0.78(1)	0.2047	1
S5	0.7158(41)	0.1166(40)	0.79(1)	0.2047	1
S6	0.9506(41)	0.2119(43)	0.29(1)	0.2047	1

Based on the structure refinement results, we think the structures of $Bi_{13}S_{18}X_2$ compounds belong to hexagonal system with space group of P3 and chemical formula of $Bi_{13}S_{18}X_2$, as shown in Figure 3.8. This structure is interesting, in which a unique triangular tunnel structure is formed by $[Bi_4S_6]$-ribbon spokes in c-axial direction, X^- are located in the tunnel sites, and Bi(II) dimers of (Bi_2^{4+}) are located at hexagonal center. TEM and HRTEM results suggested that fibrous $Bi_{13}S_{18}Br_2$ and $Bi_{13}S_{18}Cl_2$ particles were single crystals which grow in the c-axial direction, namely tunnel direction (Figure 3.9).

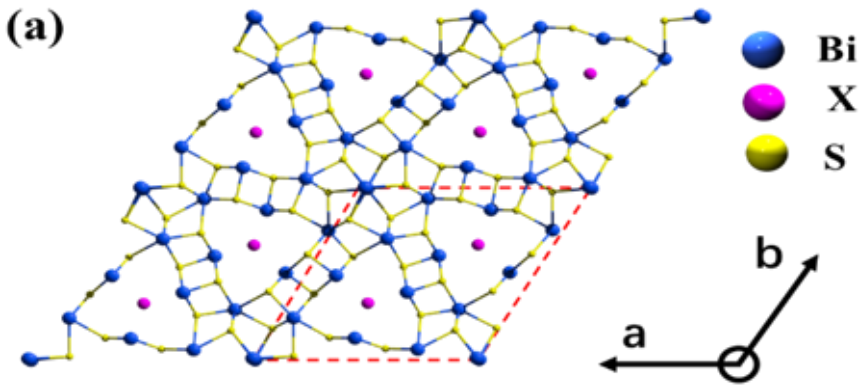

Figure 3.8 Structure of hexagonal $Bi_{13}S_{18}X_2$ with space group of P3.

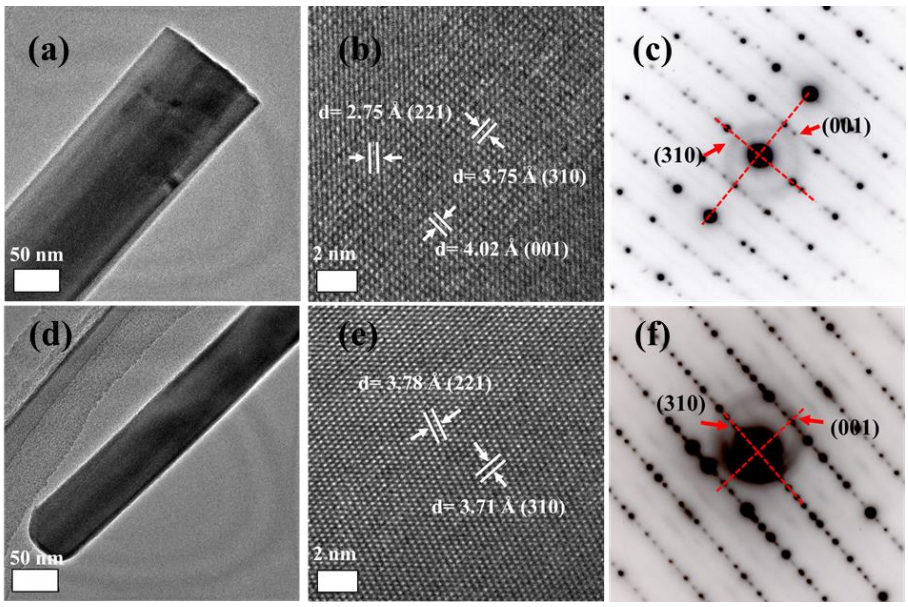

Figure 3.9 (a, d) TEM, (b, e) HRTEM images, and (c, f) SAED patterns of (a, b, c)

$Bi_{13}S_{18}Br_2$ and (d, e, f) $Bi_{13}S_{18}Cl_2$ nanofibrous crystals, respectively

3.3.3 Photoelectric behavior of bismuth chalcogenide halide compounds

The pellet samples of $Bi_{13}S_{18}X_2$ were used for the conductivity measurements at room temperature (Figure 3.10). The electrical conductivity (σ) was calculated from the applied voltage (V), measured current (I), thickness of pellet (L), and area (S) of the pellet sample using formula (2).

$$\sigma = \frac{I * L}{V * S} \qquad (2)$$

The calculated electrical conductivities of the $Bi_{13}S_{18}Cl_2$, $Bi_{13}S_{18}Br_2$ and $Bi_{13}S_{18}I_2$ pellet samples are 1.07×10^{-5}, 2.58 x 10^{-6} and 8.85 x 10^{-7} $S\cdot cm^{-1}$, respectively. We can see the electrical conductivity decreased in an order of $Bi_{13}S_{18}Cl_2$ > $Bi_{13}S_{18}Br_2$ > $Bi_{13}S_{18}I_2$ by around 1 order of magnitude with increases of the atomic radius of halogen. It has been reported that the conductivity of $Bi_{13}S_{18}I_2$ single crystal is 9×10^{-4} $S\cdot cm^{-1}$, which is much higher than the value of the pellet sample of present study.[21] It may be due to the large resistance between grain boundaries for the polycrystal pellet sample.[43, 44] As far as we know, this is the first time of report on electrical conductivities of $Bi_{13}S_{18}Cl_2$ and $Bi_{13}S_{18}Br_2$. We can speculate that single crystals of $Bi_{13}S_{18}Cl_2$ and $Bi_{13}S_{18}Br_2$ possess the higher electrical conductivities than those of the polycrystal pellet samples reported in the present study. The cross-sectional FE-SEM images of $Bi_{13}S_{18}X_2$ pellets show similar morphology and comparable density (Figure. 3.11). The large difference on electrical conductivities of $Bi_{13}S_{18}X_2$ pellet samples should be attributed to intrinsic effects caused by different halogens.

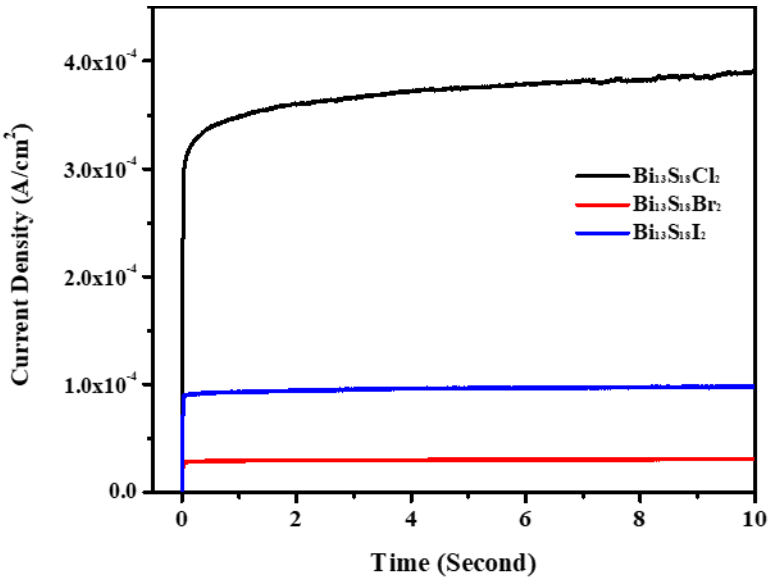

Figure 3.10 Dependences of current density of $Bi_{13}S_{18}Cl_2$, $Bi_{13}S_{18}Br_2$ and $Bi_{13}S_{18}I_2$ pellet samples on time under applied voltage of 100 V, respectively.

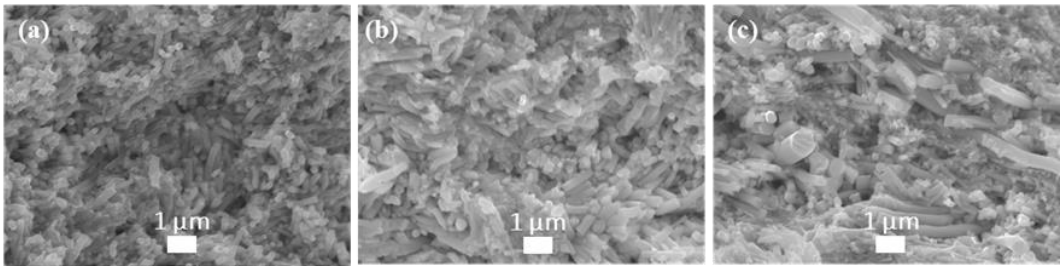

Figure 3.11 Cross-sectional FE-SEM images of (a) $Bi_{13}S_{18}Cl_2$, (b) $Bi_{13}S_{18}Br_2$ and (c) $Bi_{13}S_{18}I_2$ pellet samples fabricated by cold isostatic pressing powder sample.

Since only limited studies were reported on $Bi_{13}S_{18}X_2$ compounds, there is an argument on their bandgaps. Wu et al. reported a direct transition bandgap of 1.6 eV for $Bi_{13}S_{18}Cl_2$ calculated from the first strong cut off in visible light range.[30] Similarly, Deng et al. also get a direct transition bandgap of 1.42 for $Bi_{13}S_{18}Br_2$ from the first strong cut off in visible light range.[28] Differently, Ho et al. reported an indirect transition bandgap of 0.73 and direct transition bandgap of 1.08 eV for $Bi_{13}S_{18}I_2$ based on transmittance and thermoreflectance measurements, respectively.[21] Groom et al. rediscovered $Bi_{13}S_{18}I_2$ by studying single crystal and combined with electronic structure calculation, gave an indirect transition bandgap of 0.82 eV from the second strong cut

off in NIR range.[22] These results suggest that the first strong cut off in visible light range is the direct transition and the second strong cut off in NIR range is the indirect transition.

The bandgap energy (E_g) of a semiconductor can be estimated using Tauc's formula $(Ah\nu)^{1/n} = B(h\nu\text{-}Eg)$, where A, B, and $h\nu$ are the absorption coefficient, a constant, and the incident photon energy, and the exponent n is equal to 1/2 or 2 for the allowed direct or indirect transition, respectively.[45] Tauc's formula can be represented as the transformed Kubelka–Munk function $(Ah\nu)^{1/2} = C(h\nu\text{-}E_g)$ for the indirect transition and $(Ahv)^2 = C(hv\text{-}E_g)$ for the direct transition.[46] The bandgap energy of the second strong cut off in NIR range for the $Bi_{13}S_{18}X_2$ can be estimated from the transformed Kubelka–Munk function versus the photon energy (Figure 3.12 (b)). The estimated indirect transition bandgap energies of $Bi_{13}S_{18}Cl_2$, $Bi_{13}S_{18}Br_2$ and $Bi_{13}S_{18}I_2$ samples were 0.76, 0.80 and 0.81 eV, respectively. These results are close to bandgap energy of $Bi_{13}S_{18}I_2$ reported by Groom et al.[22] In addition, plots of $(Ah\nu)^2$ versus the photon energy for the first strong cut off in visible light range are shown in Figure 3.12 (c), exhibiting the similar direct transition bandgap energies of 1.34, 1.32 and 1.30 eV for $Bi_{13}S_{18}Cl_2$, $Bi_{13}S_{18}Br_2$ and $Bi_{13}S_{18}I_2$, respectively.

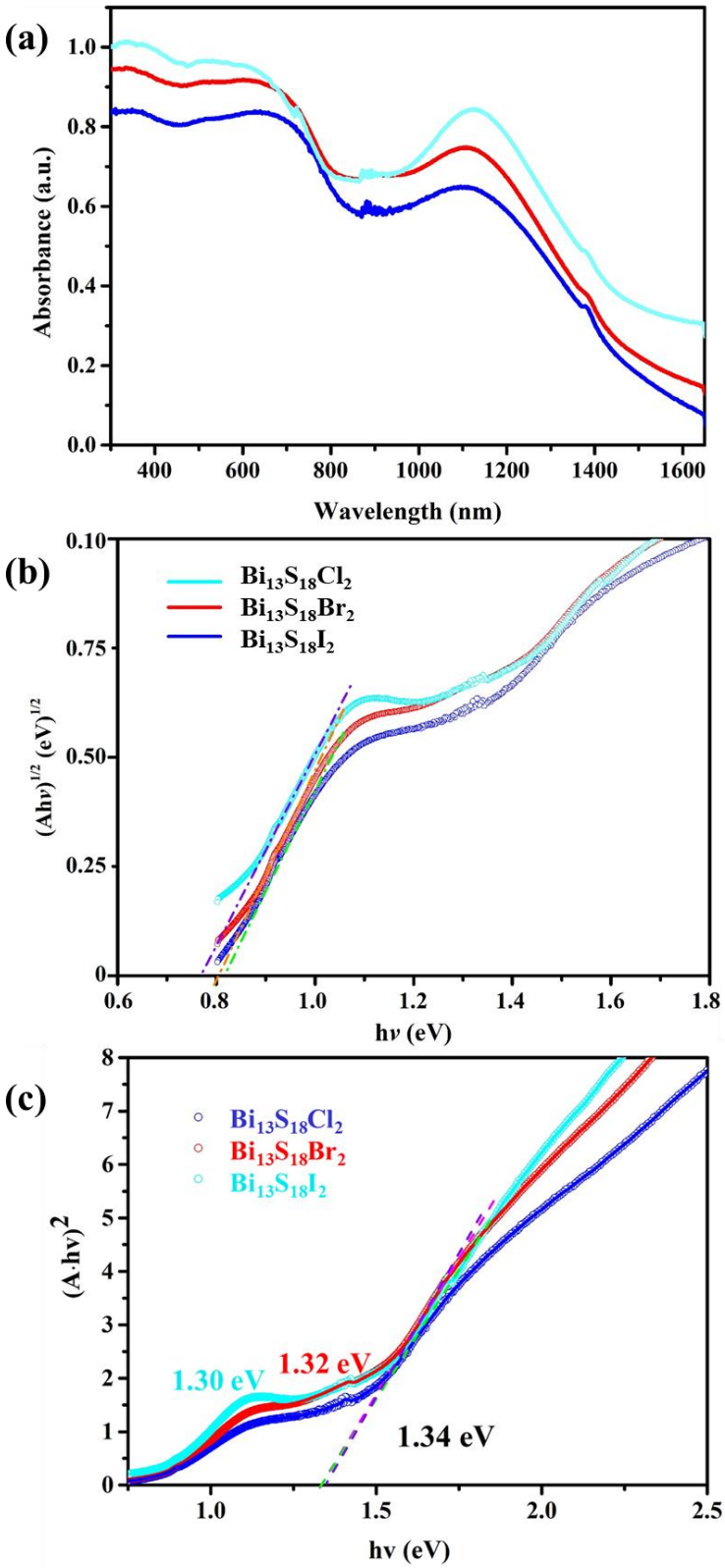

Figure 3.12 (a) UV-Vis-NIR absorption spectra and the corresponding plots of (b) the transformed Kubelka-Munk function and (c) Tauc's plot of $(Ahν)^2$ versus hν of $Bi_{13}S_{18}X_2$ powder samples, respectively.

The band structure, Fermi level, and work function are greatly important

parameters for photoelectric materials. [36] The Fermi level and valence band maximums (VBMs) of $Bi_{13}S_{18}X_2$ were examined by using UPS spectroscopy. The $Bi_{13}S_{18}X_2$ samples show similar UPS spectra with the second electron cut off energies (E_{cutoff}) of 17.77, 17.50, and 17.25 eV for $Bi_{13}S_{18}Cl_2$, $Bi_{13}S_{18}Br_2$, and $Bi_{13}S_{18}I_2$, respectively, as shown in Figure 3.13(a). The Fermi levels of $Bi_{13}S_{18}Cl_2$, $Bi_{13}S_{18}Br_2$ and $Bi_{13}S_{18}I_2$ can be evaluated as -3.97, -3.72, and -3.45 eV, respectively, from equation (1). The insert Figure of Figure 3.13(a) shows an enlargement of UPS spectra near Fermi edge; the VBMs of $Bi_{13}S_{18}Cl_2$, $Bi_{13}S_{18}Br_2$ and $Bi_{13}S_{18}I_2$ are located at 0.52, 0.47 and 0.63 eV below Fermi level, respectively. Therefore, the conduction band minimums will be located at 0.29, 0.33, and 0.13 eV above Fermi level for $Bi_{13}S_{18}Cl_2$, $Bi_{13}S_{18}Br_2$, and $Bi_{13}S_{18}I_2$, respectively; as their bandgaps (E_g) are 0.76, 0.80, and 0.81 eV, respectively, Therefore, we can give the energy band structures for $Bi_{13}S_{18}X_2$, as shown in Figure 3.13(b).

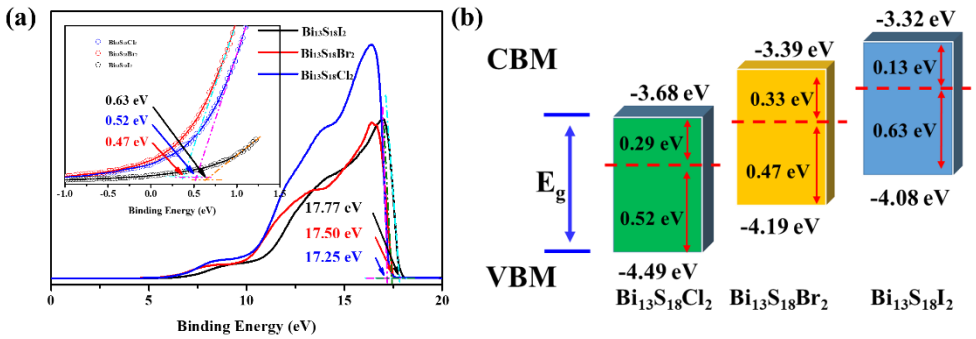

Figure 3.13 UPS spectrum of $Bi_{13}S_{18}X_2$ and (b) energy band structures of $Bi_{13}S_{18}X_2$. The inset in (a) shows an enlargement figure of red-circled part.

The VBMs for $Bi_{13}S_{18}Cl_2$ and $Bi_{13}S_{18}Br_2$ were also examined from their valence-band XPS spectra as shown in Figure 3.14. The VBMs are located at 0.52 and 0.48 eV below the Fermi level for $Bi_{13}S_{18}Cl_2$ and $Bi_{13}S_{18}Br_2$, respectively, which are very close to the results of UPS spectra. $Bi_{13}S_{18}Cl_2$ and $Bi_{13}S_{18}Br_2$ should be also an n-type semiconductor like $Bi_{13}S_{18}I_2$ because their Fermi levels are close to the conduction band minimum, respectively. [47] The results of Mott-Schottky plot also proved that $Bi_{13}S_{18}Cl_2$, $Bi_{13}S_{18}Br_2$, and $Bi_{13}S_{18}I_2$ are n-type semiconductor (Figure 3.15). The n-type

semiconductor shows positive slope value and p-type semiconductor shows a negative slope value in Mott-Schottky plot.[48] The positive slope value of $Bi_{13}S_{18}X_2$ suggest they are n-type semiconductor.

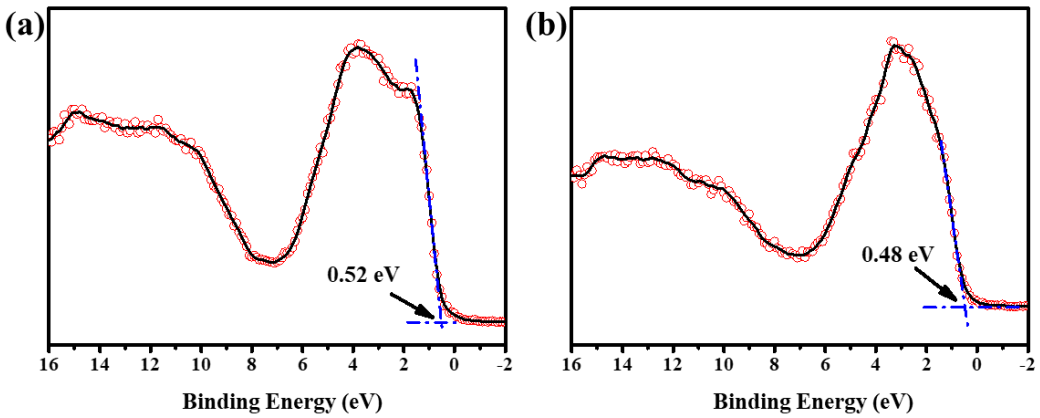

Figure 3.14 Valance-band XPS spectra of (a) $Bi_{13}S_{18}Cl_2$ and (b) $Bi_{13}S_{18}Br_2$.

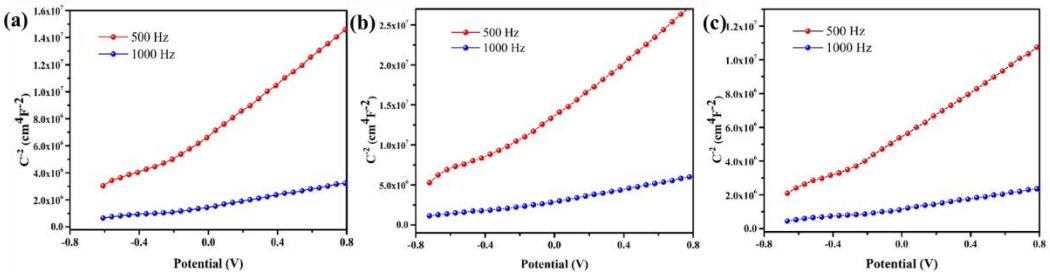

Figure 3.15 Mott-Schottky plots of (a) $Bi_{13}S_{18}Cl_2$, (b) $Bi_{13}S_{18}Br_2$ and (c) $Bi_{13}S_{18}I_2$ at frequencies of 500 and 1000 Hz, respectively.

The surface valences state and chemical compositions of the $Bi_{13}S_{18}Cl_2$ and $Bi_{13}S_{18}Br_2$ samples were examined by X-ray photoelectron spectroscopy (XPS). The XPS survey spectra reveal the predominant present of sulfur, bismuth and chlorine for $Bi_{13}S_{18}Cl_2$, and sulfur, bismuth and bromine for $Bi_{13}S_{18}Br_2$; all of the $Bi_{13}S_{18}X_2$ samples present small amounts of carbon and oxygen impurities (Figure 3.16). Carbon and oxygen should be originated from the residual organic precursor and adsorbed oxygen or water molecules on the particle surface. The Bi-$4f_{7/2}$ and Bi-$4f_{5/2}$ peaks were observed at 158.0 and 163.3 eV for $Bi_{13}S_{18}Cl_2$ and 157.9 and 163.2 eV for $Bi_{13}S_{18}Br_2$;

these values corresponds to those of 158.0 and 163.3 eV for $Bi_{13}S_{18}I_2$. Notably, the observed chemical shift for values Bi-4f of $Bi_{13}S_{18}X_2$ are little different (about 0.7 eV) from trivalent Bi(III) of 158.7 and 164.0 eV in BiSI.[49] This difference should be attributed to the coexistence of bivalent Bi (II) and trivalent Bi (III) in $Bi_{13}S_{18}X_2$ but only trivalent Bi(III) in BiSI. The XPS results support our structural study results that $Bi_{13}S_{18}X_2$ should adopt the structure with space group of P3 and chemical formula of $(Bi^{3+})_{12}(Bi_2^{4+})_{0.5}(S^{2-})_{18}(X^-)_2$ ($Bi_{13}S_{18}X_2$) with the bivalent (Bi_2^{4+}) dimers rather than space group of $P6_3$ and chemical formula of $Bi_{19}S_{27}X_3$ or $(Bi(Bi_2S_3)_9X_3)_{2/3}$. A single peak of S-2s was observed at 225.1 and 225.2 eV for $Bi_{13}S_{18}Cl_2$ and $Bi_{13}S_{18}Br_2$, respectively. The Cl-$3p_{3/2}$ and Cl-$3p_{5/2}$ spin-orbit spin components were observed at 199.0 and 197.4 eV for $Bi_{13}S_{18}Cl_2$, respectively. The two peaks located at 68.8 and 67.8 eV can be attributed to Br-$3d_{3/2}$ and Br-$3d_{5/2}$ spin-orbit spin components of Br^- in $Bi_{13}S_{18}Br_2$, respectively. The XPS quantitative analysis results suggest that the atomic ratios of X/Bi/S are 1:6.4:8.9 and 1:6.4:9.0 in the $Bi_{13}S_{18}Cl_2$ and $Bi_{13}S_{18}Br_2$ samples, respectively, which are very close to the stoichiometric mole ratio of 1:6.5:9.0 of $(Bi^{3+})_{12}(Bi_2^{4+})_{0.5}(S^{2-})_{18}(X^-)_2$, indicating successful preparation of $Bi_{13}S_{18}Cl_2$ and $Bi_{13}S_{18}Br_2$ phases.

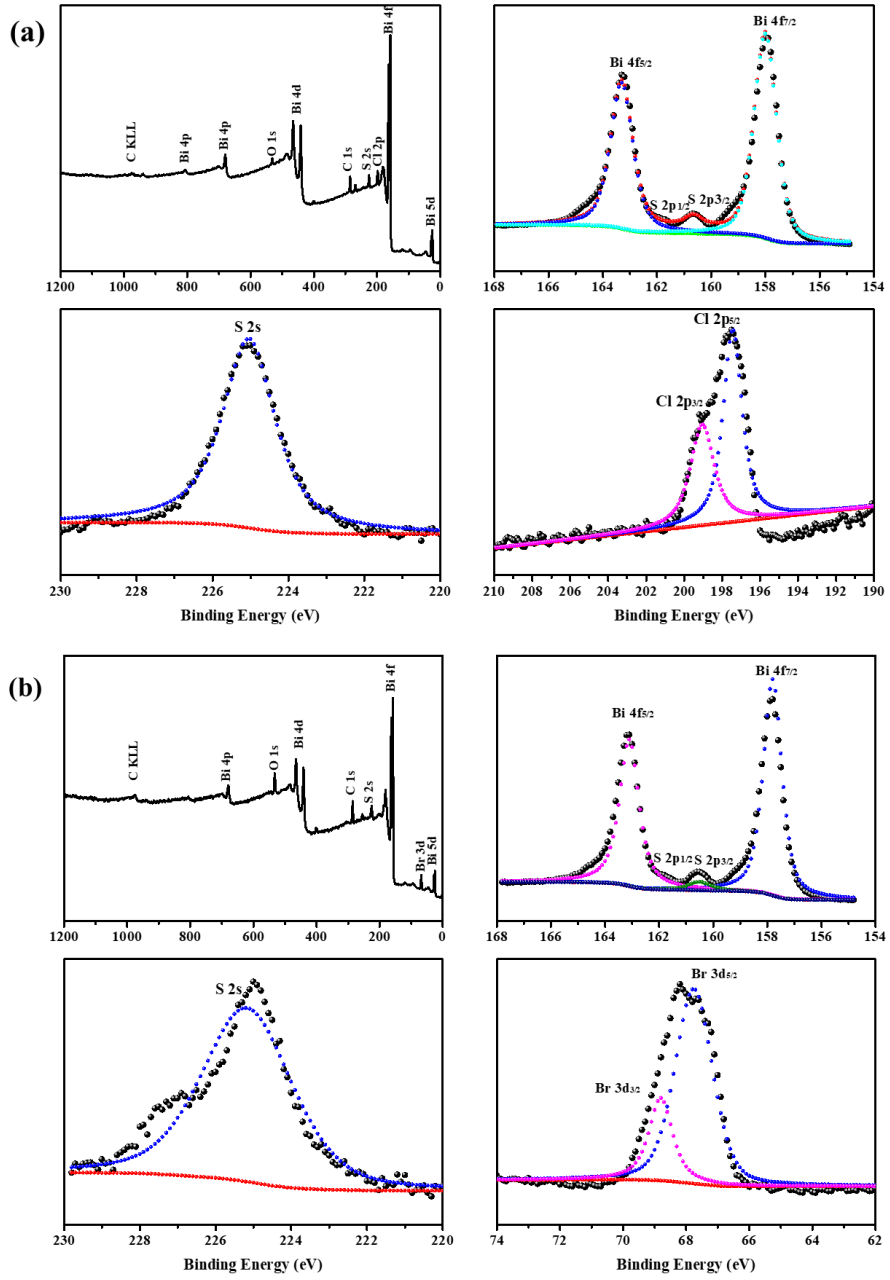

Figure 3.16 XPS survey spectra and high-resolution XPS scan spectra of (a) $Bi_{13}S_{18}Cl_2$ and (b) $Bi_{13}S_{18}Br_2$ samples

3.3.4 Fabrication of bismuth chalcogenide halide thin films by PVD process

In chapter II, we have fabricated $Bi_{13}S_{18}I_2$-based solar cell with a PCE of 0.85%, in which $Bi_{13}S_{18}I_2$ thin film fabricated by a modified solvothermal process is used as a light absorber. In the present study, a facile PVD process was developed for the

fabrications of uniform $Bi_{13}S_{18}X_2$ thin films as the light absorbers for the $Bi_{13}S_{18}X_2$-based solar cells. Figure 3.17 shows the XRD patterns of as-prepared $Bi_{13}S_{18}Br_2$ film by PVD process and films obtained after heat-treatment at different temperatures in N_2 atmosphere for 12 h. The as-prepared $Bi_{13}S_{18}Br_2$ thin film is an amorphous phase where only diffraction peaks of SnO_2 phase of FTO glass substrate were observed. With increasing the heat-treatment temperature, Bi_2S_3 phase was formed at 100 °C, $Bi_{13}S_{18}Br_2$ and Bi_2S_3 phases were formed at 150 °C, $Bi_{13}S_{18}Br_2$ single phase was formed at 200 and 250 °C. The crystallinity of $Bi_{13}S_{18}Br_2$ increased with increasing the heat-treatment temperature. At 300 °C, $Bi_{13}S_{18}Br_2$ phase was decomposed to Bi_2S_3 phase. The as-prepared $Bi_{13}S_{18}Br_2$ film has uniform thickness but low density with some small pores in the amorphous film (Figure 3.18). After the heat-treatment at 250 °C, a $Bi_{13}S_{18}Br_2$ film with high density and high crystallinity was obtained. The $Bi_{13}S_{18}Cl_2$ and $Bi_{13}S_{18}I_2$ thin films can also be fabricated by the process similar to $Bi_{13}S_{18}Br_2$, namely heat-treatment of the amorphous $Bi_{13}S_{18}Cl_2$ and $Bi_{13}S_{18}I_2$ thin films fabricated by PVD process at 250 °C in N_2 atmosphere (Figure 3.19).

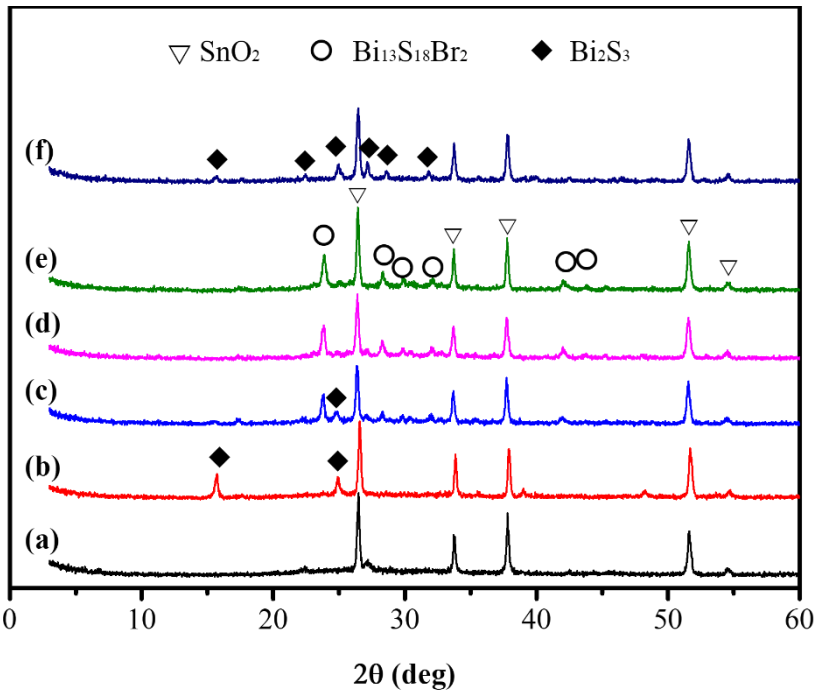

Figure 3.17 XRD patterns of (a) as-prepared $Bi_{13}S_{18}Br_2$ film on FTO glass substrate by PVD process and film obtained after heat-treatment at (b) 100, (c) 150, (d) 200, (e) 250, and (f) 300 °C

in N_2 atmosphere for 12h, respectively.

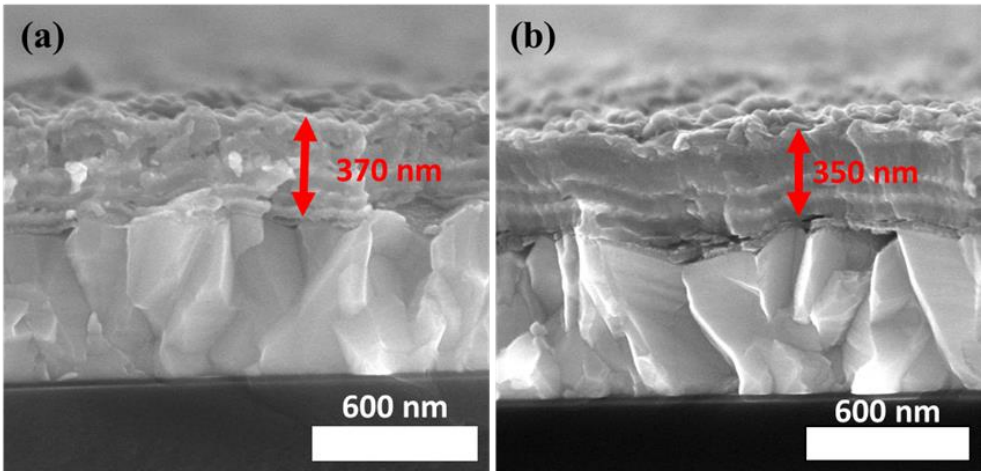

Figure 3.18 FE-SEM images (a) as prepared $Bi_{13}S_{18}Br_2$ film and (b) film after heat-treatment at 250 °C for 12h.

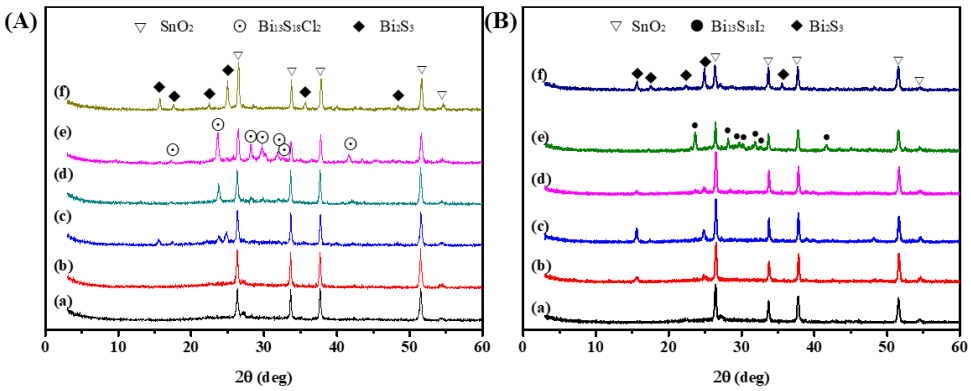

Figure 3.19 XRD patterns of (A) $Bi_{13}S_{18}Cl_2$ and (B) $Bi_{13}S_{18}I_2$ films deposited on FTO glass plates by PVD process and after heat-treatment. (a) As prepared films by PVD process and after thermal treatment at (b) 100, (c) 150, (d) 200, (e) 250, and (f) 300 °C in N_2 atmosphere for 12h.

Energy dispersive X-Ray spectroscopy (EDS) analysis was employed to confirm the chemical compositions of $Bi_{13}S_{18}X_2$ powder samples used for the PVD process, as-prepared $Bi_{13}S_{18}X_2$ films, and $Bi_{13}S_{18}X_2$ films after heat-treatment (HT) at 250 °C in N_2 atmosphere (Table 5). The $Bi_{13}S_{18}X_2$ powder samples have chemical compositions close to those of expected stoichiometric compositions of $Bi_{13}S_{18}X_2$. Furthermore, the

chemical compositions of the as-prepared $Bi_{13}S_{18}X_2$ films and the heat-treated films are almost the same as their powder samples, namely very close to their expected stoichiometric compositions. The nanostructures of the heat-treated $Bi_{13}S_{18}X_2$ films at 250 °C were investigated by using TEM and HRTEM analyses. As shown in Figure 3.20, the high density films are constructed from close-packed $Bi_{13}S_{18}X_2$ granular nanocrystals. Crystal sizes of nanocrystals of $Bi_{13}S_{18}Cl_2$, $Bi_{13}S_{18}Br_2$ and $Bi_{13}S_{18}I_2$ are about 10, 20, and 15 nm, respectively. The polycrystalline SAED patterns were observed for the $Bi_{13}S_{18}X_2$ films, which correspond to powder samples in Figure 3.9. However, the granular nanocrystal morphologies are different from their powder samples with fibrous crystal morphologies (Figure 3.5). The above results suggest that the transformation reactions from the amorphous $Bi_{13}S_{18}X_2$ phases to the crystalline $Bi_{13}S_{18}X_2$ phases are near *in situ* crystallization reactions. Namely, neighboring Bi, S and X compositions react together to form $Bi_{13}S_{18}X_2$ nanocrystals, where without long-distance diffusion for the formation of fibrous crystals.

Table 5. EDS analysis results of atonic percentages of $Bi_{13}S_{18}X_2$ powder samples, as-prepared $Bi_{13}S_{18}X_2$ films by PVD process and $Bi_{13}S_{18}X_2$ films after thermal treatment at 250 °C for 12 h.

Compounds	Elements	Expected	Powder	As-prepared	After HT
	Bi	39.39	39.09	40.33	40.53
$Bi_{13}S_{18}I_2$	S	54.55	54.35	53.02	53.14
	I	6.06	6.56	6.65	6.33
	Bi	39.39	39.22	40.26	40.19
$Bi_{13}S_{18}Br_2$	S	54.55	54.06	52.89	53.02
	Br	6.06	6.72	6.85	6.79
	Bi	39.39	38.79	40.65	41.87

$Bi_{13}S_{18}Cl_2$	S	54.55	54.71	52.84	52.05
	Cl	6.06	6.60	6.51	6.08

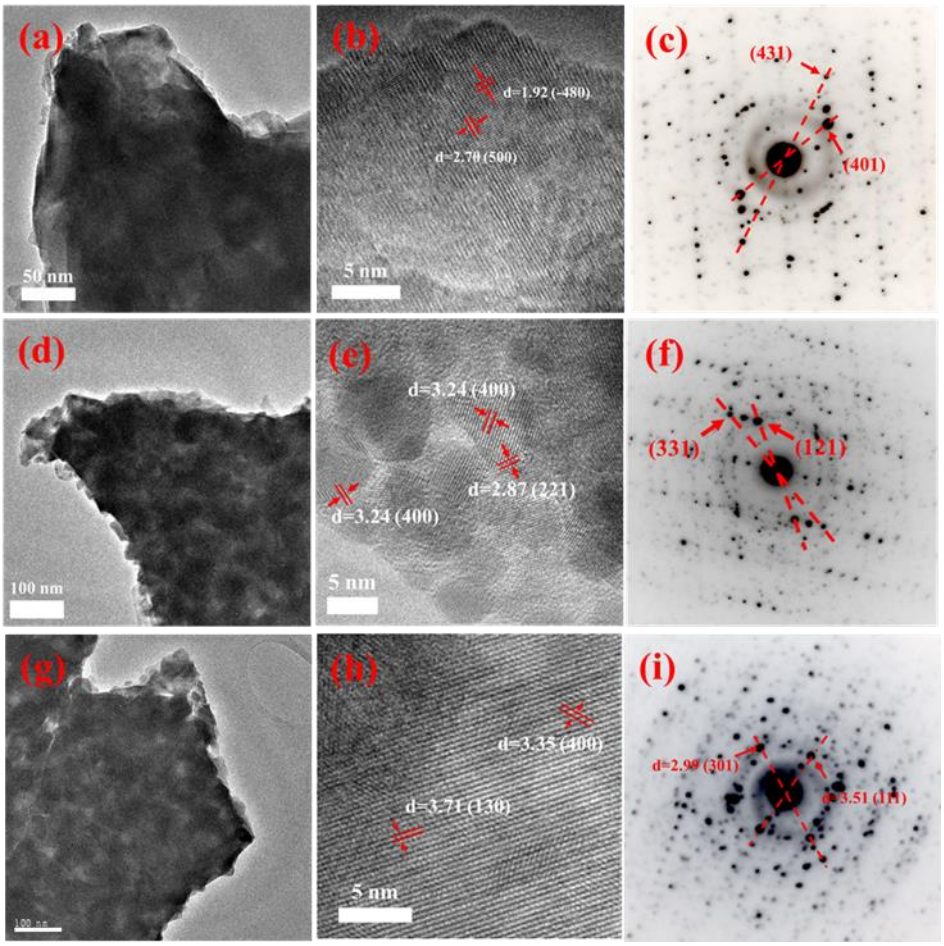

Figure 3.20 (a, d, g) TEM, (b, e, h) HRTEM images, and (c, f, i) SAED patterns of (a, b, c) $Bi_{13}S_{18}Cl_2$, (d, e, f) $Bi_{13}S_{18}Br_2$, and (g, h, i) $Bi_{13}S_{18}I_2$ films after heat-treatment at 250 ºC for 12 h in N_2 atmosphere.

3.3.5 Performances of $Bi_{13}S_{18}X_2$-based solar cells

To study solar cell performance, FTO/TiO_2/ $Bi_{13}S_{18}X_2$ electrodes were fabricated.

A dense TiO_2 film was coated on the surface of FTO conducting glass substrate as a hole blocking layer. Then, $Bi_{13}S_{18}X_2$ films with different thicknesses were deposited on the dense TiO_2 film surface by PVD process, then heat-treatment at 250 °C for 12 h in N_2 atmosphere. The $Bi_{13}S_{18}X_2$-based solar cells were constructed from the FTO/TiO_2/ $Bi_{13}S_{18}X_2$ electrodes, an electrolyte solution of I_3^-/I^- redox couple as hole-transporting material and a Pt-coated FTO conducting glass as counter-electrode, as shown in Figure 3.21(a). In the present study, we mainly focused on the effect of thickness of $Bi_{13}S_{18}X_2$ light harvesting layer on the solar cell performance because it is known that the thickness of light harvesting layer is one of the most importance factor for the solar cells.[50-52] If the light harvesting layer is too thin, it cannot harvest enough photons, resulting a low photocurrent. However, if the light harvesting layer is too thick, it will hander the charge carrier extraction due to its large resistance, leading to a high percentage of exciton recombination.

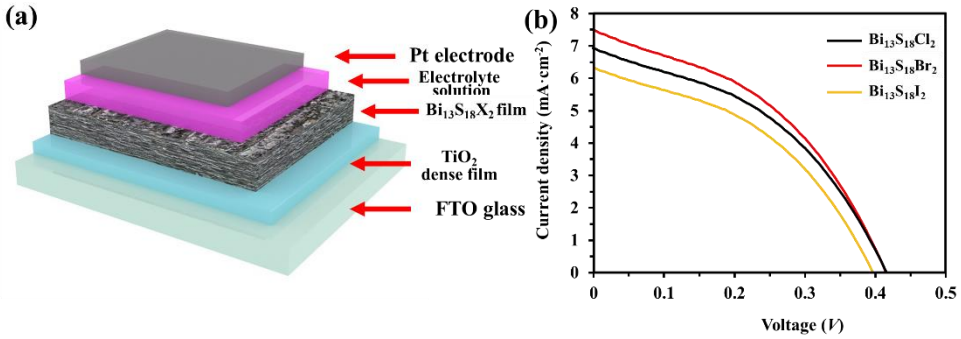

Figure 3.21 Schematic illustration of (a) $Bi_{13}S_{18}X_2$-based solar cell structure and (b) J-V curve of $Bi_{13}S_{18}X_2$-based solar cells with optimum film thickness of $Bi_{13}S_{18}X_2$.

A series of FTO/TiO_2/ $Bi_{13}S_{18}X_2$/ (I_3^-/I^- redox couple)/Pt devices were fabricated with different $Bi_{13}S_{18}X_2$ film thicknesses in a range of 100 to 500 nm. The solar cell parameters of short-circuit current densities (J_{sc}), open-circuit voltages (V_{oc}), fill factor (FF), and power conversion efficiency (PCE) are plotted as a function of $Bi_{13}S_{18}X_2$ film thickness in Figure 3.22. The J_{sc} value of $Bi_{13}S_{18}Br_2$-based solar cell increases, reach

the maximum value of 7.5 (mA/cm^2) at around 400 nm, and then decreases with the increase in the $Bi_{13}S_{18}Br_2$ film thickness (Figure 3.22(a)). $Bi_{13}S_{18}Cl_2$ and $Bi_{13}S_{18}I_2$ also exhibit the similar J_{sc} behavior with the maximum J_{sc} value around 350 nm. The maximum J_{sc} value increases in the order of $Bi_{13}S_{18}I_2$ < $Bi_{13}S_{18}Cl_2$ < $Bi_{13}S_{18}Br_2$. The V_{oc} values of $Bi_{13}S_{18}X_2$-based solar cells also increase, reach the maximum values at around 350 nm, and the decreases with the increase in the $Bi_{13}S_{18}X_2$ film thickness (Figure 3.22(b)). However, the changes of V_{oc} values with changing the $Bi_{13}S_{18}X_2$ film thickness are much smaller than the those of J_{sc} values. The maximum V_{oc} values are 0.42, 0.42, 0.38 V for $Bi_{13}S_{18}Cl_2$, $Bi_{13}S_{18}Br_2$, and $Bi_{13}S_{18}I_2$, respectively. These values are much smaller than the theoretical V_{oc} value of 0.9 V calculated from conduction band minimum of TiO_2 (-0.5 V) and redox potential of I_3^-/I^- (0.4 V) hole-transporting material.[53] The FF values also exhibit similar behavior to V_{oc} values with maximum FF values of 33%, 35%, and 30% at the $Bi_{13}S_{18}X_2$ film thickness around 400 nm (Figure 3.22(c)). The FF values are quite low compared with high performance solar cells.

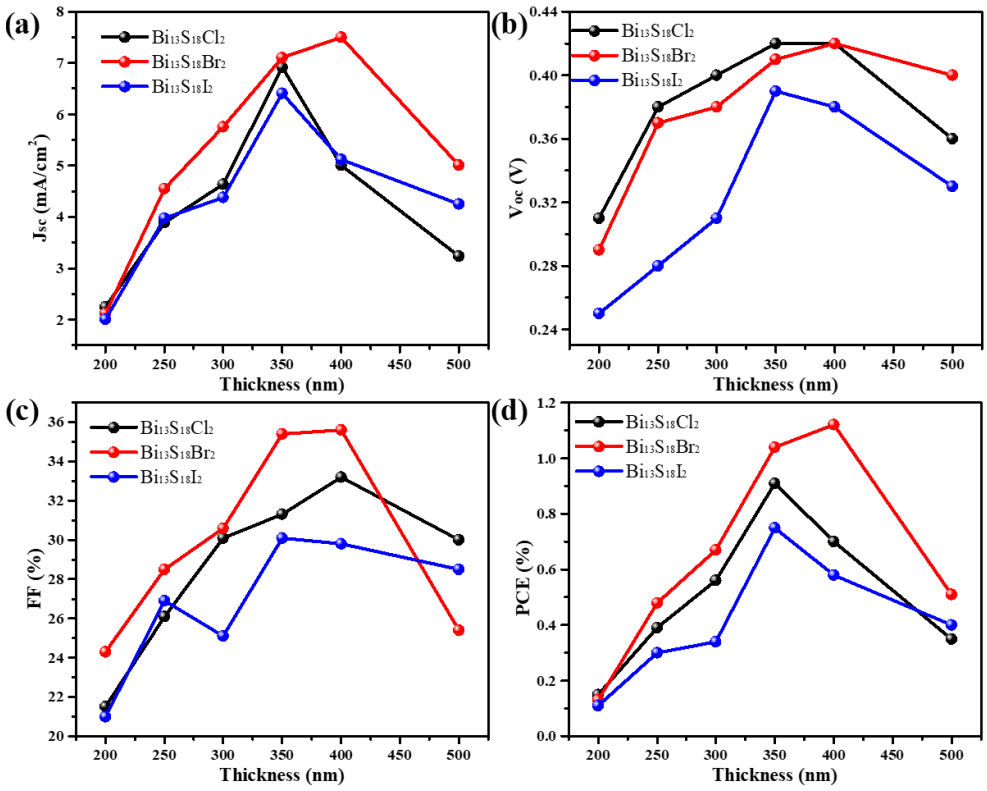

Figure 3.22 (a) Short circuit current density (J_{sc}), (b) open circuit voltage (V_{oc}), (c) fill factor (FF), and (d) power conversion efficiency (PCE) as a function of $Bi_{13}S_{18}X_2$ film thickness.

The PCE values are mainly dependent on the J_{sc} values, namely increase, reach the maximum values at around 400 nm, and then decreases with the increase in the $Bi_{13}S_{18}X_2$ film thickness (Figure 3.22). The maximum PCE value increases in the order of $Bi_{13}S_{18}I_2$ (0.75%) < $Bi_{13}S_{18}Cl_2$ (0.91%) < $Bi_{13}S_{18}Br_2$ (1.12%). The J-V curves and cell parameters of solar cells with the optimum film thickness are shown in Figure 3.22 (b) and Table 6. Compared with the $Bi_{13}S_{18}I_2$-based solar cells prepared by solvothermal process with cell parameters of PCE (0.85%), J_{sc} (3.82 mA/cm^2), V_{oc} (0.58 V), FF (38.3%), the $Bi_{13}S_{18}I_2$-based solar cell prepared by PVD process possesses cell parameters of PCE (0.75%), J_{sc} (6.41 mA/cm^2), V_{oc} (0.38 V), FF (30%). The much higher J_{sc} value for PVD process than that of solvothermal process is due to higher density and larger thickness of $Bi_{13}S_{18}I_2$ film prepared by PVD process, which enhances light harvesting. The higher V_{oc} and FF values for the solvothermal process can be attributed to nanorod crystal morphology and thinner $Bi_{13}S_{18}I_2$ film prepared by solvothermal process, which enhances the charge carrier extraction by reduces film resistance.[20] The PCE value increasing order of $Bi_{13}S_{18}I_2$ < $Bi_{13}S_{18}Cl_2$ < $Bi_{13}S_{18}Br_2$ corresponds to the J_{sc} value increasing order, namely PCEs are mainly dependent on J_{sc} values. Figure 3.23(a) shows the absorption spectra of the FTO/TiO_2/ $Bi_{13}S_{18}X_2$ electrodes of the optimum devices after J-V current measurements. All of these three electrodes exhibited a broad light absorption in the wavelength range from 300 to 800 nm. The visible light absorption increases in an order of $Bi_{13}S_{18}I_2$ < $Bi_{13}S_{18}Cl_2$ < $Bi_{13}S_{18}Br_2$, which corresponds with the increasing order of J_{sc} of the $Bi_{13}S_{18}X_2$-based devices.

Table 6. The device performance parameters for $Bi_{13}S_{18}X_2$-based solar cells

Cells	Thickness (nm)	V_{oc} (V)	J_{sc} (mA/cm^2)	FF (%)	PCE (%)
$Bi_{13}S_{18}Cl_2$	200	0.31	2.25	0.22	0.15
	250	0.38	3.89	0.26	0.39
	300	0.40	4.64	0.30	0.56
	350	0.42	6.92	0.31	0.91

	400	0.42	5.01	0.33	0.70
	500	0.36	3.24	0.30	0.35
$Bi_{13}S_{18}Br_2$	200	0.29	2.12	0.21	0.13
	250	0.37	4.55	0.29	0.48
	300	0.38	5.76	0.31	0.67
	350	0.41	7.11	0.36	1.04
	400	0.42	7.50	0.36	1.12
	500	0.40	5.01	0.25	0.51
$Bi_{13}S_{18}I_2$	200	0.25	2.01	0.22	0.11
	250	0.28	3.98	0.27	0.30
	300	0.31	4.38	0.25	0.34
	350	0.39	6.41	0.30	0.75
	400	0.38	5.12	0.29	0.58
	500	0.33	4.25	0.28	0.40

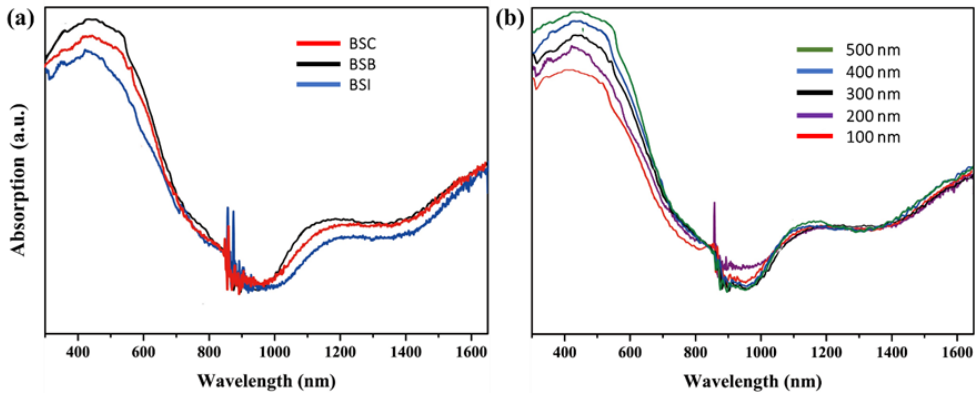

Figure 3.23 UV-Vis-NIR absorption spectra of (a) $Bi_{13}S_{18}X_2$ films used in solar cells and (b) $Bi_{13}S_{18}Br_2$ films with different thickness after heat-treatment at 250 ^oC for 12 h.

The optimum FTO/TiO_2/ $Bi_{13}S_{18}Br_2$ electrode was investigated by FE-SEM and AFM (Figure 3.24). The as-prepared $Bi_{13}S_{18}Br_2$ film is constructed from nanoparticles and has relatively smooth surface with some small pores (Figure 3.24 (a)), in which $Bi_{13}S_{18}Br_2$ is amorphous phase (Figure 3.17(a)). AFM image reveals its surface

roughness was about 120 nm (Figure 3.24 (d)). After heat-treatment at 250 °C, the amorphous phase was transformed to the crystalline $Bi_{13}S_{18}Br_2$ phase, which accompanies increase of nanoparticle size and surface roughness to about 150 nm and disappearing the small pores (Figure 3.24 (b) and (e)). The surface roughness can enhance the light scattering effect to improve the light absorption of $Bi_{13}S_{18}Br_2$ film resulting enlarged PCE.[54] The cross-sectional image of FTO/TiO_2/ $Bi_{13}S_{18}Br_2$ electrode reveals that the dense TiO_2 layer with a thickness of about 50 nm is coated tightly on FTO surface and the $Bi_{13}S_{18}Br_2$ layer of high density with thickness of about 400 nm coated tightly on TiO_2 layer, which guarantees its high photoelectric performance. The results suggested that the PVD process developed in the present study is promising for fabrication of high performance $Bi_{13}S_{18}X_2$ film for solar cells.

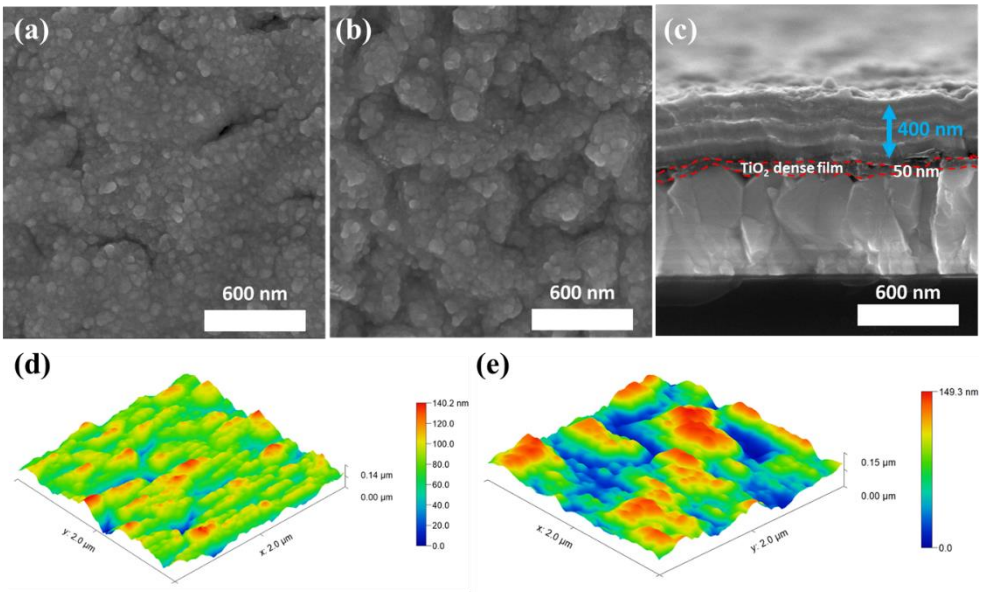

Figure 3.24 FE-SEM images of (a, b) top-view and (c) cross-section of (a) as-prepared FTO/TiO_2/ $Bi_{13}S_{18}Br_2$ electrode and (b, c) after heat-treatment at 250 °C for 12h. AFM images of (d) as-prepared FTO/TiO_2/ $Bi_{13}S_{18}Br_2$ electrode surface and (e) after heat-treatment at 250 °C for 12h.

3.4 Conclusions

The solvothermal process is effective for the synthesis of high quality stoichiometric $Bi_{13}S_{18}X_2$ compounds. The formations of $Bi_{13}S_{18}X_2$ compounds are strongly affected by S/Bi mole ratio, reaction temperature, and solvent in the solvothermal reaction system. $Bi_{13}S_{18}X_2$ compounds adopt the same triangular tunnel structure of hexagonal system with space group of P3 and composition of $(Bi^{3+})_{12}(B_2^{4+})_{0.5}(S^{2-})_{18}(X^-)_2$. The tunnel structure of $Bi_{13}S_{18}X_2$ is constructed from $[Bi_4S_6]$-ribbon spokes in c-axial direction, X^- located in the tunnel sites, and Bi(II) dimers of (Bi_2^{4+}) located at hexagonal center. $Bi_{13}S_{18}Cl_2$, $Bi_{13}S_{18}Br_2$, and $Bi_{13}S_{18}I_2$ compounds are indirect n-type semiconductors with narrow bandgaps of 0.76, 0.80 and 0.81 eV, respectively, and exhibit strong light absorbance in a wide wavelength range from UV to NIR. The uniform $Bi_{13}S_{18}X_2$ films can be fabricated by using a combined process of PVD and heat-treatment. The solar cells using the $Bi_{13}S_{18}X_2$ light absorbers with thickness about 400 nm exhibit the highest PCEs of 0.91, 1.12 and 0.75% for $Bi_{13}S_{18}Cl_2$, $Bi_{13}S_{18}Br_2$, and $Bi_{13}S_{18}I_2$, respectively. The highest cell performance of $Bi_{13}S_{18}Br_2$ in $Bi_{13}S_{18}X_2$ can be attributed its higher light absorption ability. These results demonstrate the potential application of $Bi_{13}S_{18}X_2$ as stable light absorber for a new type of solar cell that can be fabricated by a facile PVD process.

3.5 References

1. L. S. Gomez-Velazquez, A. Hernandez-Gordillo, M. J. Robinson, V. J. Leppert, S. E. Rodil and M. Bizarro, *Dalton Trans*, 2018, **47**, 12459-12467.
2. N. C. Miller and M. Bernechea, *APL Materials*, 2018, **6**, 084503.
3. J. L. DiMeglio and J. Rosenthal, *J Am Chem Soc*, 2013, **135**, 8798-8801.
4. P. C. K. Vesborg and T. F. Jaramillo, *RSC Advances*, 2012, **2**, 7933.
5. C. Wadia, A. P. Alivisatos and D. M. Kammen, *Environ Sci Technol*, 2009, **43**, 2072-2077.
6. A. Audzijonis, L. Žigas, A. Kvedaravičius and R. Žaltauskas, *Ferroelectrics*, 2009, **392**, 45-54.
7. D. Tiwari, F. Cardoso-Delgado, D. Alibhai, M. Mombrú and D. J. Fermín, *ACS Applied Energy Materials*, 2019, **2**, 3878-3885.
8. Y. Sasaki, *J. Appl. Phys*, 1965, 614.
9. A. Audzijonis, G. Gaigalas, L. Žigas, A. Pauliukas, R. Žaltauskas, A. Čerškus, D. Balnionis and A. Kvedaravičius, *J ELECTRON SPECTROSC*, 2008, **164**, 19-23.
10. J. Li, Y. Yu and L. Zhang, *Nanoscale*, 2014, **6**, 8473-8488.
11. M. Guan, C. Xiao, J. Zhang, S. Fan, R. An, Q. Cheng, J. Xie, M. Zhou, B. Ye and Y. Xie, *J Am Chem Soc*, 2013, **135**, 10411-10417.
12. X. Zhang, Z. Ai, F. Jia and L. Zhang, *J. Phys. Chem.*, 2008, **112**, 747-753.
13. J. Lee, B.-K. Min, I. Cho and Y. Sohn, *B KOREAN CHEM SOC*, 2013, **34**, 773-776.
14. H. Kunioku, M. Higashi and R. Abe, *Sci Rep*, 2016, **6**, 32664.
15. K. Ren, J. Liu, J. Liang, K. Zhang, X. Zheng, H. Luo, Y. Huang, P. Liu and X. Yu, *Dalton Trans*, 2013, **42**, 9706-9712.
16. S. Bargozideh and M. Tasviri, *New J Chem*, 2018, **42**, 18236-18241.
17. I. Aguiar, M. Mombrú, M. P. Barthaburu, H. B. Pereira and L. Fornaro, *Mater. Res. Express.*, 2016, **3**, 025012.
18. H. Shi, W. Ming and M.-H. Du, *Physical Review B*, 2016, **93**.

19. A. M. Ganose, S. Matsumoto, J. Buckeridge and D. O. Scanlon, *Chem Mater*, 2018, **30**, 3827-3835.
20. A. M. Ganose, K. T. Butler, A. Walsh and D. O. Scanlon, *J. Mater. Chem. A*, 2016, **4**, 2060-2068.
21. C. H. Ho, Y. H. Chen, Y. K. Kuo and C. W. Liu, *Chem Commun (Camb)*, 2017, **53**, 3741-3744.
22. R. Groom, A. Jacobs, M. Cepeda, R. Drummey and S. E. Latturner, *Chem. Mater*, 2017, **29**, 3314-3323.
23. K. Mariolacos, *Mater. Res. Bull.*, 2004, **39**, 591-598.
24. V. Kramer, *Naturforsch*, 1974, **29b**, 688.
25. Y. Yan, Y. Xu, S. Lei, X. Ou, L. Chen, J. Xiong, Y. Xiao and B. Cheng, *Dalton Trans.*, 2018, **47**, 3408-3416.
26. Y. Wu, H. Pan, X. Zhou, M. Li, B. Zhou, C. Yang, W. H. Zhang, J. Jie and C. Li, *Chem Sci*, 2015, **6**, 4615-4622.
27. K. Adams, A. F. González, J. Mallows, T. Li, J. H. J. Thijssen and N. Robertson, *J. Mater. Chem. A*, 2019, **7**, 1638-1646.C. Deng, H. Guan and X. Tian, *Mater. Lett.*, 2013, **108**, 17-20.
28. Y. Chen, G. Tian, T. Feng, W. Zhou, Z. Ren, T. Han, Y. Xiao and H. Fu, *CrystEngComm*, 2015, **17**, 6120-6126.
29. Z. Wu, Y. Jiang, X. Xiong, S. Ding, Y. Shi, X. Liu, Y. Liu, Z. Huang and J. Hu, *Catal. Sci. Technol.*, 2017, **7**, 3464-3468.
30. G. Miehe and V. Kupčík, *Die Naturwissenschaften*, 1971, **58**, 219-219.
31. G. Shen, D. Chen, K. Tang, L. Huang and Y. Qian, *J. Cryst. Growth*, 2003, **249**, 331-334.
32. Z. S. Aliev, S. S. Musayeva, F. Y. Jafarli, I. R. Amiraslanov, A. V. Shevelkov and M. B. Babanly, *J. Alloys Compd.*, 2014, **610**, 522-528.
33. K. Mariolacos, *Acta Cryst.*, 1975, 1947-1949.
34. C. Chen, L. Xu, G. A. Sewvandi, T. Kusunose, Y. Tanaka, S. Nakanishi and Q. Feng, *Cryst. Growth Des.*, 2014, **14**, 5801-5811.
35. A. Kahn, *Mater. Horiz.*, 2016, **3**, 7-10.

36. E. Makovicky, *Z. Kristallogr. Cryst. Mater*, 1985, **173**, 1-23.
37. V. Kramer, *J. Appl. Crystallogr.*, 1973, 499.
38. Z. Wu, Y. Liu, S. Zhang, Z. Huang, Q. Jiang, T. Zhou and J. Hu, *J. Mater. Chem. A*, 2018, **6**, 21404-21409.
39. Z. Luo, Y. Vasquez, J. F. Bondi and R. E. Schaak, *Ultramicroscopy*, 2011, **111**, 1295-1304.
40. J. A. Aguilar-Martínez, M. I. Pech-Canul, C. Leyva-Porras, E. Rodríguez and V. Iván Hernández, *Ceram. Int.*, 2013, **39**, 8237-8243.
41. B. H. Toby, *Powder Diffr.*, 2012, **21**, 67-70.
42. S. Sharifi-Asl, V. Yurkiv, A. Gutierrez, M. Cheng, M. Balasubramanian, F. Mashayek, J. Croy and R. Shahbazian-Yassar, *Nano Lett*, 2020, **20**, 1208-1217.
43. L. Dai, H. Li, H. Hu and S. Shan, *J. Geophys. Res.*, 2008, **113**.
44. J. Tauc, *Mater. Res. Bull.*, 1968, **3**, 37-46.
45. M. A. Butler, *J. Appl. Phys*, 1977, **48**, 1914-1920.
46. J. You, Z. Hong, Y. M. Yang, Q. Chen, M. Cai, T. B. Song, C. C. Chen, S. Lu, Y. Liu, H. Zhou and Y. Yang, *ACS Nano*, 2014, **8**, 1674-1680.
47. A. W. Bott, *Current Separations*, 1998, 87-91.
48. J. Grigas, E. Talik, M. Adamiec, V. Lazauskas and V. Nelkinas, *J ELECTRON SPECTROSC*, 2006, **153**, 22-29.
49. D. Liu, M. K. Gangishetty and T. L. Kelly, *J. Mater. Chem. A*, 2014, **2**, 19873-19881.
50. L. C. Andreani, A. Bozzola, P. Kowalczewski, M. Liscidini and L. Redorici, *ADV PHYS-X*, 2018, **4**, 1548305.
51. Y. Sun, S. Lin, W. Li, S. Cheng, Y. Zhang, Y. Liu and W. Liu, *Engineering*, 2017, **3**, 452-459.
52. G. A. Sewvandi, Z. Tao, T. Kusunose, Y. Tanaka, S. Nakanishi and Q. Feng, *ACS APPL MATER INTER*, 2014, **6**, 5818-5826.
53. L. Zheng, Y. Ma, S. Chu, S. Wang, B. Qu, L. Xiao, Z. Chen, Q. Gong, Z. Wu and X. Hou, *Nanoscale*, 2014, **6**, 8171-8176.

Chapter IV

Enhanced Photovoltaic Performance of BiSCl Solar Cells through Nanorod Array

4.1 Introduction

Photovoltaics (PVs), which directly convert solar energy to electric energy, offer a practical solution to challenge the increasing demand for sustainable energy. In the past decade, the hybrid organic-inorganic lead halide perovskites solar cells (PSCs) have gained huge attention and already achieved an excellent power conversion efficiency (PCE) of 25%.[1] Unfortunately, the intrinsic instability of PSCs and the environmental risk of toxic Pb are still unresolved, limiting its commercial applications.[2] As a potential alternative candidate for the lead halide perovskites, bismuth-based materials have gained increasing attention in the photovoltaic field because bismuth is a non-toxic and non-bioaccumulating element.[3] Furthermore, the bismuth-based materials are expected to show comparable light absorber properties to the lead halide perovskites and to be tolerant to vacancy and antisite defects by considering that both Pb(II) and Bi(III) adopt the same electronic configuration of $d^{10}s^2p^0$.[4-10]

Bi-VI-VII compounds exhibit a wide variety of interesting physical properties, such as semiconductivity, photoelectricity, electrooptical effect, photoconductivity, luminescence effect, magnetic susceptibility, ferroelectricity, piezoelectricity.[11-15] Importantly, Bi-VI-VII compounds possess a soft polarizability and can form various compounds with rich nanostructure diversity.[16, 17] A large number of studies have been extensively carried out on the Bi-VI-VII compounds as visible-light-driven photocatalysts.[18, 19] BiOX (X = Cl, Br, I) compounds possess tunable bandgaps from

3.46 eV for BiOCl to 1.77 eV for BiOI and has exhibited excellent photocatalytic activities.[14, 20, 21] Recently, some of Bi-VI-VII compounds have also been studied as light absorber for solar cells, gaining increasing attention as an alternative for lead halide perovskites. BiOI is the most promising light absorber for solar cells in the BiOX compounds due to its strong light absorption in a wavelength range from UV to visible light. Zhao et al. reported the first study on BiOI-based solar cells and gave a PCE of 0.1%.[15] Recently, Hoye et al. achieved a PCE of 1.8% for the BiOI-based solar cells, in which the BiOI light absorber film shown a high stability in ambient air and defect-tolerant features.[22]

As a promising light absorber, BiSI has been widely studied for solar cells. Hahn et al. reported first study on BiSI-based solar cells and gave a PCE of 0.25%.[23] Recently, Tiwari et al. addressed the energy-level band matching for the BiSI-based solar cells by using SnO_2 as the electron transport layer (ETL) and F8 (poly(9,9-di-n-octylfluorenyl-2,7-diyl) as the hole transport material (HTM), which achieved the best PCE of 1.32%.[24] In chapter III, our studies have demonstrated that $Bi_{13}S_{18}X_2$-based solar cells with an architecture of FTO/TiO_2/$Bi_{13}S_{18}X_2$/(I_3^-/I^-)/Pt exhibited PCEs of 0.91, 1.12, and 0.75% for $Bi_{13}S_{18}Cl_2$, $Bi_{13}S_{18}Br_2$ and $Bi_{13}S_{18}I_2$, respectively, suggesting the possible application of $Bi_{13}S_{18}X_2$ to photovoltaic and photoelectric devices.

The crystal morphology of the light absorbers can strongly affect the performance of solar cells, in which 1D nanomaterials are being explored to develop next-generation solar cells. The 1D nanomaterials can improve the light absorption ability and charge separation that are unique as compared to bulk materials.[25] Furthermore, the efficient carriers transport along the pathway direction and less grain boundaries of the oriented 1D nanomaterials can minimize carriers recombination losses.[2] Some nanorod array films have been designed as light absorbers for the new generation high efficient solar cells. The light absorbers of nanorod array oriented parallelly to the carrier transporting direction can efficiently suppress optical reflection and improve light scattering and trapping.[26] Such radical junction device structure guarantees sufficient light absorption, charge generation, and carriers separation and transportation.[27, 28] The nanostructured 1D array of light absorbers have been successfully applied in various solar cells, such

as groups of IV, II-VI, and III-V semiconductors, metal oxides, binary and multinary chalcogenides.[26, 27, 29, 30] Recently, nanostructured 1D array have also been extensively studied in perovskite solar cells.[31-33] Very recently, Xiong et al. proved that the performance of BiSI-based solar cells can be improved by using a light absorber layer of BiSI nanorod array on a tungsten substrate.[26]

However, only a limited number of studies on BiSCl have been reported since it was first reported by Ritsche in 1959.[34] These studies mainly focused on theoretical researches because BiSCl is not easy to be synthesized. The BiSCl single crystal was growth at high temperature over 600 ºC using Bridgeman-Stockbarger technique that requires expensive equipment.[34] The BiSCl powder sample was also prepared using high temperature processes, such as molten salt process.[35] Those sophisticated processes limit the experimental researches and applications of BiSCl and its physicochemical properties are, as yet, almost undiscovered.

In this chapter, we describe a facile solvothermal method to synthesize single-crystalline BiSCl nanofibers to systemically evaluate its photoelectric behavior as a light absorber for solar cells for the first time. BiSCl possesses the strong light absorption in a wavelength range from UV to visible light, corresponding to a bandgap of 1.96 eV. UPS spectrum and DFT calculation revealed that it is an n-type direct semiconductor with VBM and CBM located at 6.04 and 4.08 eV below the vacuum level, respectively. A homogeneous BiSCl nanorod array film on the TiO_2 porous film was successfully fabricated by a modified solvothermal process. The BiSCl-based solar cells with an architecture of FTO/TiO_2/BiSCl/(I_3^-/I^-)/Pt were fabricated using the BiSCl nanorod array films to study the potential of BiSCl as a light absorber for solar cells. The preliminary photovoltaic results exhibited a PCE of 1.36%, suggesting a potential possibility of BiSCl as a light absorber for solar cells which can be fabricated by the low-cost solution process.

4.2 Experimental

4.2.1 Synthesis of BiSCl nanofibers sample.

Typically, for the synthesis of BiSCl nanofibers sample, $BiCl_3$ (5 mmol) and CH_4N_2S (2 mmol) were solvothermally treated with 20 mL of acetone solvent in a Teflon-lined stainless autoclave with an internal volume of 80 mL at 200 ºC for a desired time under stirring conditions. The obtained sample was filtrated, washed with acetone, and then dried in a drying oven at 60 ºC for 12 h.

4.2.2 Fabrication and characterization of solar cells.

The TiO_2 electrode was prepared in the following manner.[36] The fluorine-doped tin oxide (FTO) conducting glass plate was cleaned in distilled water and acetone by ultrasonication for 10 min, consecutively. Then the FTO glass plate was dipped in 0.1 M titanium tetraisopropoxide (TTIP) solution for 1 min and washed with distilled water and ethanol, dried at room temperature, and calcined at 480 °C for 1 h to coat the FTO glass surface with a dense TiO_2 thin film. A TiO_2 nanocrystal paste was then coated on the dense TiO_2 thin film on the FTO glass plate by a screen printing technique and dried at 120 °C for 10 min. This process was repeated to obtain TiO_2 nanocrystal film with a thickness of about 10 μm. After the TiO_2 paste coating, the TiO_2 film was calcined at 450 °C for 30 min, and then dipped into the 0.1 M TTIP solution for 1 min, washed with distilled water and ethanol, dried at room temperature, and calcined at 480 °C for 1 h to obtain a TiO_2 nanoporous electrode. The TiO_2 nanocrystal paste was prepared by mixing a P25 TiO_2 nanocrystal sample (0.5 g), ethanol (2.5 g), α-terpineol (2.0 g), a 10 wt % solution of ethyl-cellulose 10 (1.4 g), and a 10 wt % solution of ethyl-cellulose 45 (1.1 g). The mixture was dispersed by ultrasonication for 30 min and then ball-milling for 72 h. After ball-milling, the ethanol was removed from the mixture using a rotary evaporator.[36]

0.5 mmol $BiCl_3$ (1.0511 g), 0.2 mmol CH_4N_2S (0.1012 g) were dissolved in 3 mL acetone solvent by stirring for 1 h, and then a yellow $BiCl_3$-CH_4N_2S mixed solution

was obtained. The mixed solution was coated on the TiO_2 nanoporous electrode surface and then dried at room temperature for 2 h. The coated process with $BiCl_3$-CH_4N_2S mixed solution was repeated for twice. The coated TiO_2 nanoporous electrode was placed on a shelf set in a Teflon-lined stainless steel autoclave with an internal volume of 80 mL. After adding 1 mL acetone solvent to the autoclave bottom, the autoclave was sealed and solvothermally treated at 200 ^oC for 12 h to obtain black-red BiSCl-coated TiO_2 electrode. After cooling to room temperature, the obtained black-red BiSCl-coated TiO_2 electrode was washed with acetone and then dried at 60 ^oC for 12 h in a drying oven.

A BiSCl solar cell was comprised of the BiSCl-coated TiO_2 electrode as an anode, Pt-coated FTO glass as a cathode, and an electrolyte solution between the anode and the cathode. The electrolyte solution contained 0.1 M LiI, 0.01 M I_2, 0.6 M 1-butyl-3-n-propylimidazolium iodide, 0.4 M 4-tert-butylpyridine, and 0.1 M guanidine thiocyanate in a mixed solvent of acetonitrile and valeronitrile (v/v = 85:15). The photocurrent−voltage characteristic curve for the BiSCl-based solar cell was measured using a Hokuto-Denko BAS100B electrochemical analyzer under irradiation with simulated sunlight of AM 1.5 (100 mW/cm^2), using a sunlight simulator (YSS-E40, Yamashita Denso). A light-passing mask was fixed on the surface of the FTO glass of the anode to set the effectively irradiating area on the cell at 0.25 cm^2. The external quantum efficiency (EQE) spectrum of the BiSCl-based solar cell was performed using a 250 W tungsten halogen lamp source with an Oriel Cornerstone 130 monochromator.

4.2.3 Physical analysis

The crystal structure of the sample was investigated using a powder X-ray diffractometer (XRD) (Shimadzu, model XRD-6100) with Cu Kα (λ = 0.1542 nm) radiation. Software Fullprof was used for Rietveld Refinement of structure. The morphology of the samples was observed using field emission scanning electron microscopy (FE-SEM) (JEOL, ISM-7001F) and the chemical composition was

measured using energy dispersive X-ray spectroscopy (EDX) attached to the FE-SEM at 15 kV of acceleration voltage. Transmission electron microscopy (TEM) and high-resolution TEM (HR-TEM) observations were performed on a JEOL Model JEM-3010 system at 300 kV. The ultraviolet-visible (UV-vis) absorption spectrum was obtained on a Shimadzu solidspec-3700 UV-Vis-NIR spectrophotometer at room temperature. The TG-DTA analysis was carried out using a thermal analyzer (Shimadzu, DTG-60H) at a heating rate of 10 ^{o}C/min. X-ray photoelectron spectroscopy (XPS) was performed using a Kratos AXIS SUPRA X-ray photo-electron spectrometer. The XPS spectra were calibrated to the adventitious carbon peak at 284.8 eV. Ultraviolet photoelectron spectroscopy (UPS) was carried out using a Thermo Fisher ESCALAB 250Xi with helium-lamp radiation (21.22 eV) as an excitation source, and Fermi level was calibrated with Au. The relationship of work function (Φ), lamp radiation ($h\nu$), second-electron cutoff energy (E_{cutoff}), and Fermi energy (E_F) can be illustrated by

$$\Phi = h\nu - E_{cutoff} \quad (1)$$

Where $\Phi = E_{vac} - E_F$, with E_{vac} as the vacuum-level energy.[39]

4.2.4 Computational details

DFT calculations were performed using generalized gradient approximation (GGA) in the scheme of Perdew–Burke–Ernzerhof (PBEsol) as implemented in the CASTEP code.[37, 38] The core electrons were replaced with the ultrasoft core potentials. The valence electronic configurations of the ultrasoft pseudopotentials for Bi, S, and Cl were $6s^2 6p^3$, $3s^2 3p^4$, and $3s^2 3p5$, respectively. Both the plane-wave basis sets and k-point sampling were checked for convergence, with a cutoff energy of 360 eV and k-point grid of 3 × 6 × 3 for unit cell of BiSCl. Geometry optimization was performed by the BFGS algorithm under convergence tolerances of 5.0×10^{-6} eV/atom for energy, 0.01 eV/Å for maximum force, 0.02 GPa for maximum stress.

4.3 Results and discussion

4.3.1 Solvothermal synthesis and structure of BiSCl nanofibers.

BiSCl nanofibers can be synthesized by solvothermal treatment of a $BiCl_3$-CH_4N_2S mixed solution. The influence of reaction time on the formation of BiSCl was investigated using XRD, as shown in Figure 4.1(a). The XRD results indicate that a new phase with a chemical composition of $Bi_{35}S_{37}Cl_{31}$ phase was formed after the reaction for 0.5 h in the solution with a $BiCl_3/CH_4N_2S$ mole ratio of 5 : 2 at 200 °C. The chemical composition of $Bi_{35}S_{37}Cl_{31}$ was determined by EDS analysis (Figure 4.2). By prolonging the reaction time, the crystallinity of $Bi_{35}S_{37}Cl_{31}$ increased, simultaneously the formation of BiSCl phase was observed after the reaction for 1 h. Then, the fraction of $Bi_{35}S_{37}Cl_{31}$ decreased and that of BiSCl increased. After the reaction for 6 h, the $Bi_{35}S_{37}Cl_{31}$ disappeared completely, then a single phase of BiSCl was obtained. The result suggested that BiSCl is formed from $Bi_{35}S_{37}Cl_{31}$ by conversion reaction.

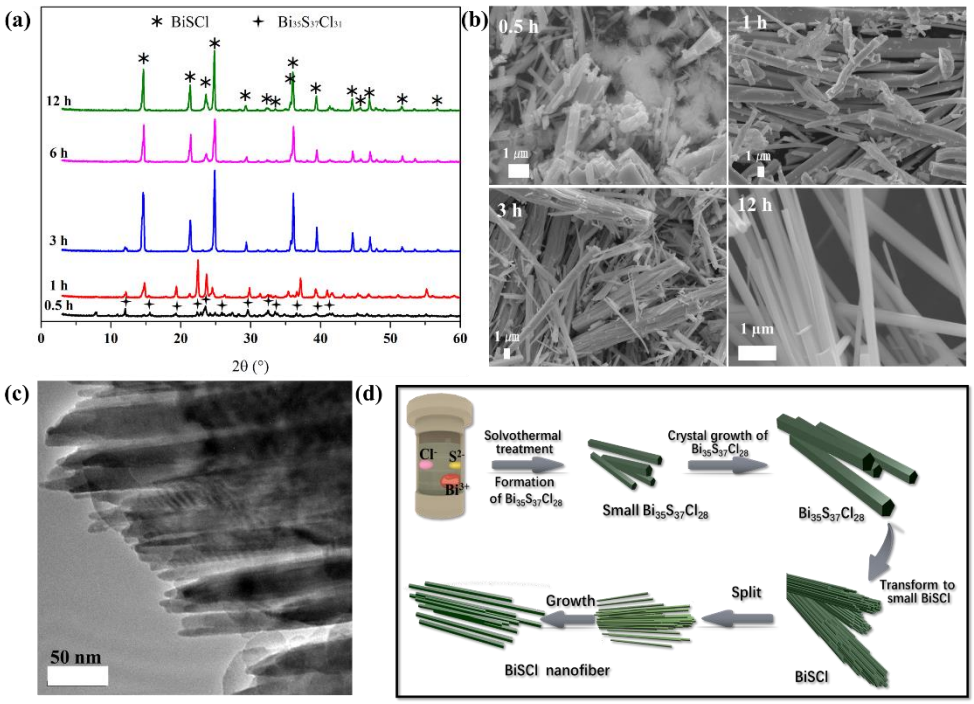

Figure 4.1 (a) XRD patterns and (b) FE-SEM images of products synthesized by solvothermal treatment of solution with $BiCl_3/CH_4N_2S$ mole ratio of 5 : 2 at 200 °C for different reaction times. (c) TEM image of product synthesized by solvothermal treatment for 6 h. (d) Schematic

illustration of formation reaction mechanism of BiSCl.

The conversion reaction of $Bi_{35}S_{37}Cl_{31}$ to BiSCl was investigated by FE-SEM and TEM observations. In the samples obtained from 0.5 h reaction, small rod-like particles of $Bi_{35}S_{37}Cl_{31}$ were formed (Figure 4.1(b)). By increasing the reaction time up to 1 h, the small rod-like particles grew to large rod-like particles, in which $Bi_{35}S_{37}Cl_{31}$ was partially transformed to BiSCl. After the reaction for 3 h, the large rod-like particles began to be split into small BiSCl nanofibers, accompanying conversion of $Bi_{35}S_{37}Cl_{31}$ to BiSCl. The splitting of large rod-like particles into nanofibers was confirmed using TEM observation, as shown in Figure 4.1(c). The split small BiSCl nanofibers grew to longer BiSCl fibers after 6 h reaction. The BiSCl fibers synthesized by solvothermal treatment for 12 h possess a nanofibrous morphology with a particle size of about 200 nm in diameter and 20 μm in length. The formation process of BiSCl can be schematically illustrated in Figure 4.1(d). A TG-DTA analysis and XRD results (Figure 4.3) suggest that BiSCl is stable up to 300 ^{o}C in air, where BiSCl partially decomposes to BiOCl. The BiSCl finally changed to a mixture of $Bi_{14}O_{20}SO_4$ and $Bi_{24}O_{31}Cl_{10}$ at above 700 ^{o}C. Compared with BiSI, BiSCl exhibits a slightly lower thermostability in air (Chapter II).

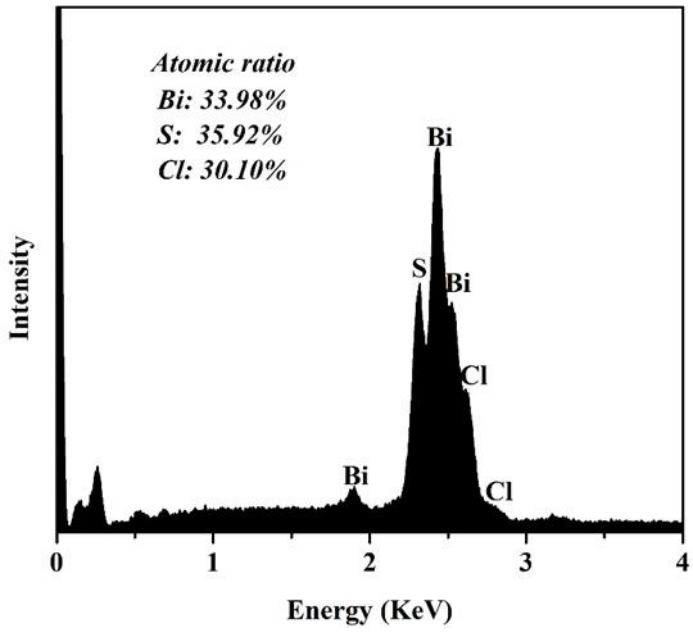

Figure 4.2 EDS spectrum of product synthesized by solvothermal treatments of $BiCl_3$-CH_4N_2S

mixtures with $BiCl_3/CH_4N_2S$ mole ratio of 5 : 2 at 200 °C for 0.5 h.

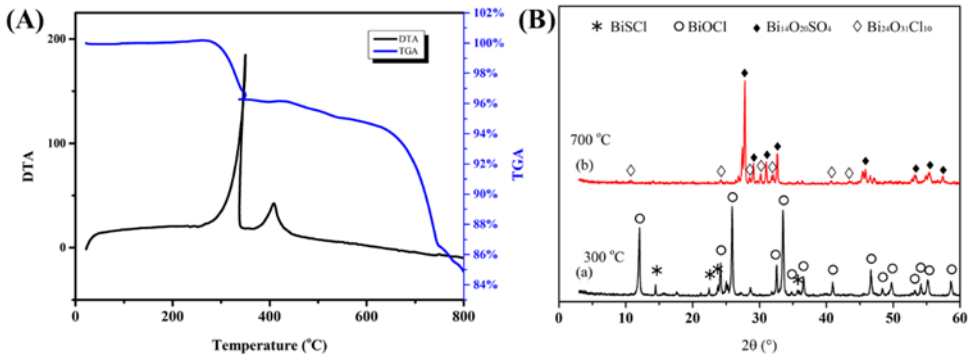

Figure 4.3 (A) TG-DTA curves of BiSCl nanofibers, and (B) XRD patterns of BiSCl nanofibers after heated at (a) 300 °C and (b) 700 °C for 3 h, respectively.

A structure refinement of BiSCl was carried using the Rietveld method. The refinement result shows an excellent fit to the orthorhombic system with a space group of *Pnam* (Figure 4.4(a)). The correlation error indices of R_p and R_{wp} were 6.68% and 8.54%, respectively. The refined atomic positions are provided in the Table S1. The refined lattice parameters of BiSCl are a = 7.6793(11) Å, b = 3.9351(9) Å, and c = 10.0444(14) Å, which are in very good agreement with previously reported data of BiSCl single crystal.[13] As shown in Figure 4.4(b), double chain subunit of $[(BiSCl)_2]_\infty$ is formed by linking Bi with S and Cl together by strong Bi-S and Bi-Cl bonds along the direction of c-axis, and the $[(BiSCl)_2]_\infty$-chains are held together by weak Van der Waals type bonds.[13]

The structure and morphology of BiSCl were characterized by TEM. The representative HR-TEM image of an individual BiSCl nanofiber showed a clear lattice fringe image with a fringe image spacing of 0.37 nm (Figure 4.4(e)), which corresponds to the (011) plane of BiSCl. The SAED result revealed that the BiSCl nanofiber was a single crystal, where the nanofiber axis corresponds to [002] direction, in other words, BiSCl crystals grow in the c-axis direction (Figure 4.4(f)). All atoms in BiSCl crystal lie on mirror planes normal to the c-axis. It is understandable that the crystallite grew along the c-axis due to the inherent chain type structure, which causes the formation of the fibrous morphology.

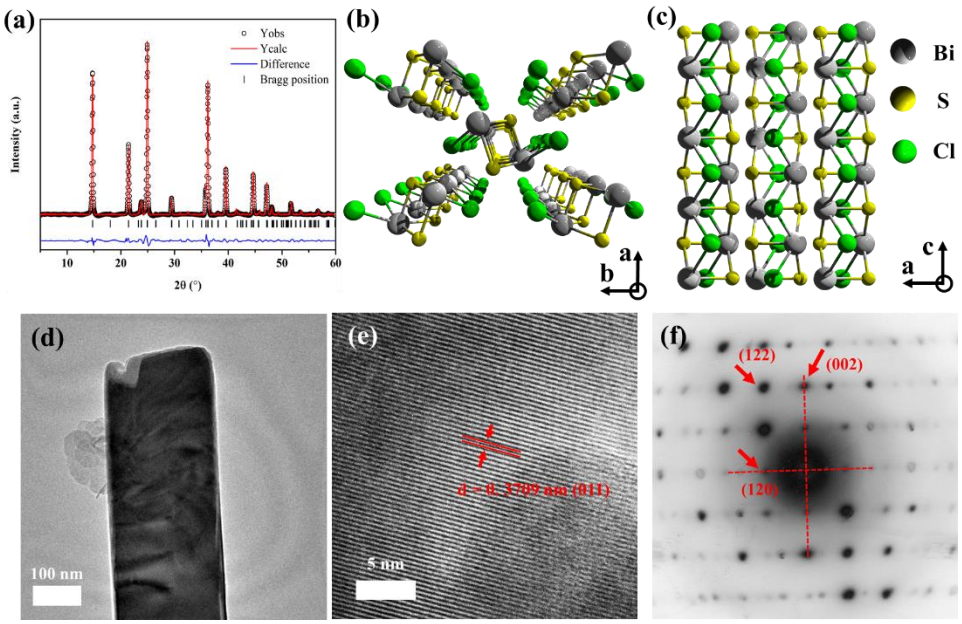

Figure 4.4 (a) Rietveld refinement result of XRD pattern of BiSCl. Three-dimensional view of BiSCl structure along (b) [001] direction, and (c) [010] direction. (d) TEM image, (e) HRTEM, (f) SAED pattern of BiSCl nanofibers.

Table 1. Fractional atomic coordinates and equivalent isotropic displacement parameters for BiSCl structure with space group *Pnam* from structural refinement using fine scan XRD data.

Atom	*a*	*b*	*c*	occupancy	B
Bi	0.13590(5)	0.25000	0.13580(3)	1.00	0.4514
S	0.81475(8)	0.25000	0.04552(4)	1.00	0.2072
Cl	0.52738(3)	0.25000	0.80204(6)	1.00	0.2120

The surface chemical composition and element chemical state in the BiSCl nanofibers were examined by XPS. The XPS survey spectrum revealed the predominance of bismuth, sulfur and chlorine, as well as a small amount of carbon and oxygen impurities (Figure 4.5). The carbon and oxygen may correspond to the residual organic precursor and adsorbed oxygen molecules on the particle surface. The Bi spin-orbit doublet peaks of Bi-$4f_{7/2}$ and Bi-$4f_{5/2}$ were observed at 158.7 and 164.0 eV, which

is consistent with the XPS results of BiSI reported in chapter II, indicating the appearance of Bi^{3+} at the surface of BiSCl nanofibers. The Cl-$2p_{3/2}$ and Cl-$2p_{1/2}$ spin-orbit coupling was observed at 197.8 and 199.3 eV, respectively. A single peak observed at 225.4 eV is attributed to S-2s, revealing the existence of the S^{2-} species. The XPS quantitative analysis results suggest that the atomic ratio of Bi : S : Cl is 1:0.94:0.97, which is consistent with the atomic ratio of 1:0.93:0.96 obtained by energy dispersive analysis of EDS (Figure 4.6(d)). The EDS-mapping on the nanofibers revealed uniform spatial distribution of Bi, S, and Cl elements (Figure 4.6). The results of chemical composition suggest the Bi-rich and S- and Cl-poor exist in the solvothermal BiSCl nanofibers. Similar Bi-rich and S-poor in BiSI have been also reported recently, which can be attributed to formation of S vacancy point defects in BiSI.[9]

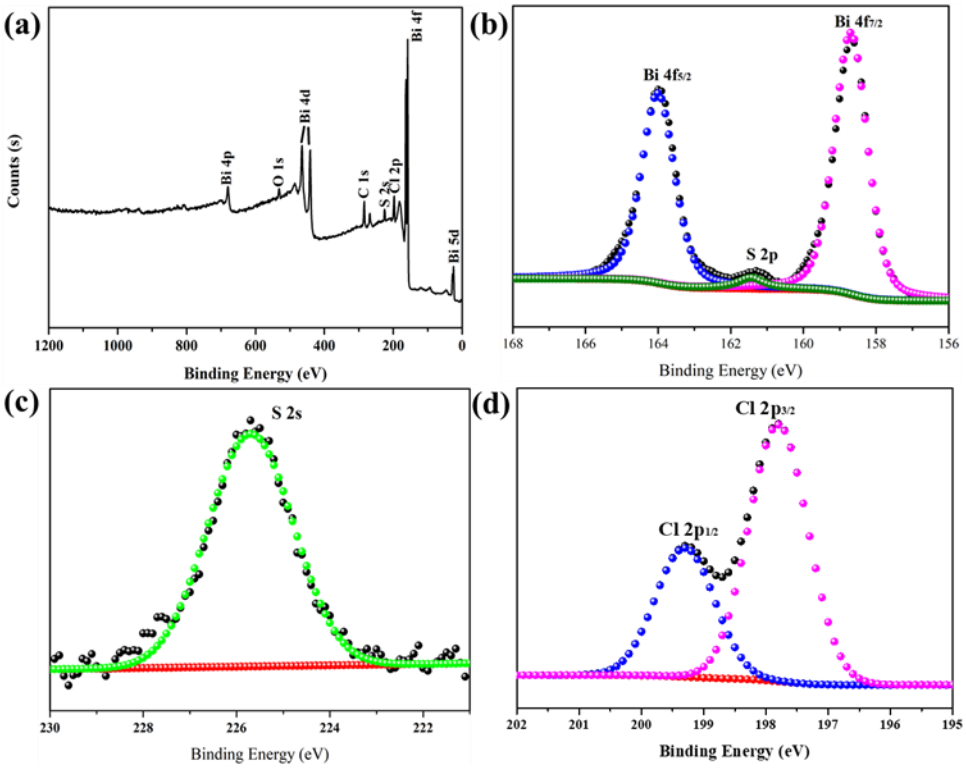

Figure 4.5 (a) XPS survey spectra and (b-d) high-resolution XPS scan spectra of BiSCl nanofibers.

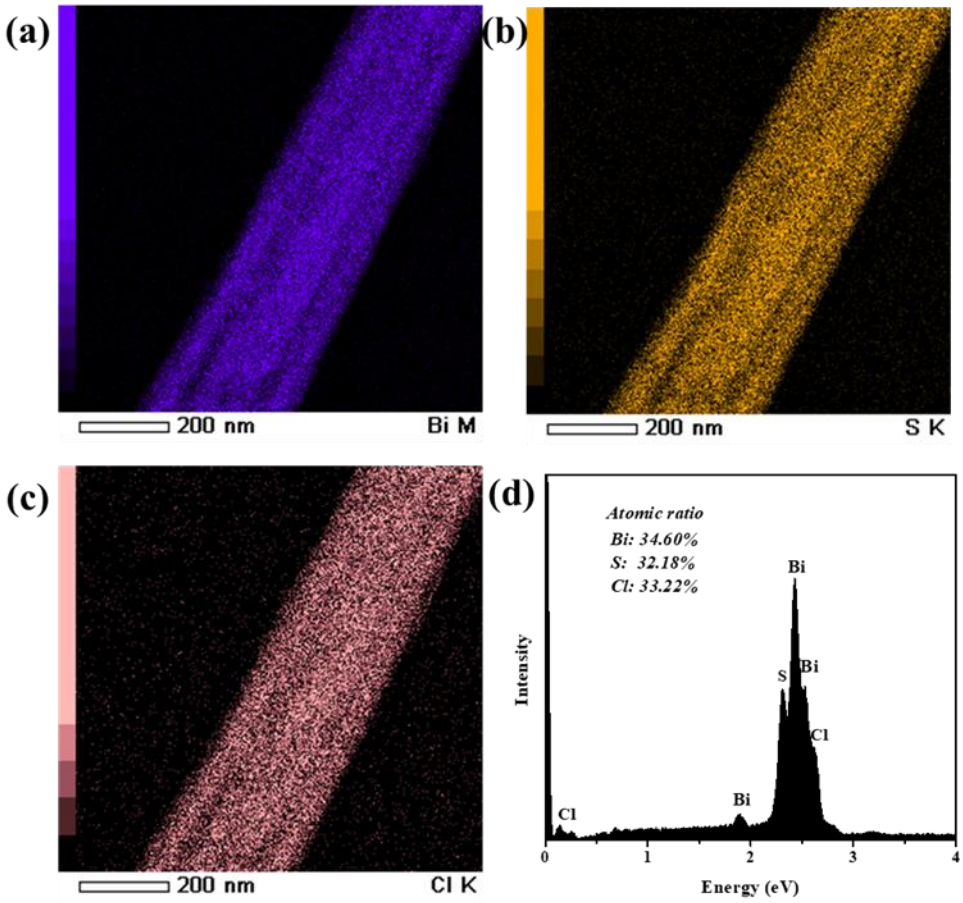

Figure 4.6 (a-c) EDS mapping of individual BiSCl nanofiber, and (d) EDS spectrum of individual BiSCl nanofiber.

4.3.2 Photoelectric properties of BiSCl nanofibers.

Some studies have been reported on the solar cells using a BiSI light absorber and given some high potential results.[2, 24, 26, 39] BiSCl has a red-dark colour and similar structure to BiSI, which stimulates us to investigate the photoelectric properties of BiSCl as a light absorber for solar cells. Figure 4.7(a) is the UV-visible absorption spectrum of BiSCl; a strong and broad absorption peak in the wavelength range of 300 to 650 nm was observed. Namely, the electrons in BiSCl can be excited in this wavelength range, suggesting a potential as a light absorber for solar cells. The bandgap energy (E_g) of a semiconductor can be estimated using Tauc's formula $(A\mathit{hv})^{1/n} = B(\mathit{hv}-E_g)$, where A, B, and *hv* are the absorption coefficient, a constant, and the incident

photon energy, and the exponent n is equal to 1/2 or 2 for the allowed direct or indirect transition, respectively.[40] It has been reported that BiSCl is a direct semiconductor.[41, 42] Therefore, plotting $(A\textit{hv})^2$ versus *hv* and extrapolating the linear portion of the curve to the *hv* axis gives the bandgap of 1.96 eV (Figure 4.7(b)).

The band structure, Fermi level, and work function are greatly important parameters for photoelectric materials.[43] The work function and VBM of BiSCl were examined by using UPS spectroscopy. The solvothermal BiSCl nanorods show a second electron cutoff energy (E_{cutoff}) of 16.50 eV in Figure 4.7 (c). The Φ can be evaluated as 4.72 eV from equation (1), which means the Fermi level located at 4.72 eV below the vacuum level. The insert Figure of Figure 4.7(c) shows an enlargement of UPS spectrum near Fermi edge, indicating that the VBM is located at 1.32 eV below the Fermi level. Therefore, the VBM and CBM will be located at 6.04 and 4.08 eV below the vacuum level, respectively, because the E_g is 1.96 eV. Figure 4.7(d) shows the obtained energy band structure for BiSCl nanofibers. The VBM for BiSCl was also examined from the valence-band XPS spectrum as shown in Figure 4.8. The result revealed that the VBM is located at 1.30 eV below the Fermi level, in great agreement with the result of UPS spectrum. Therefore, BiSCl should be an n-type semiconductor similar to BiSI because Fermi level is close to the conduction band minimum.[44]

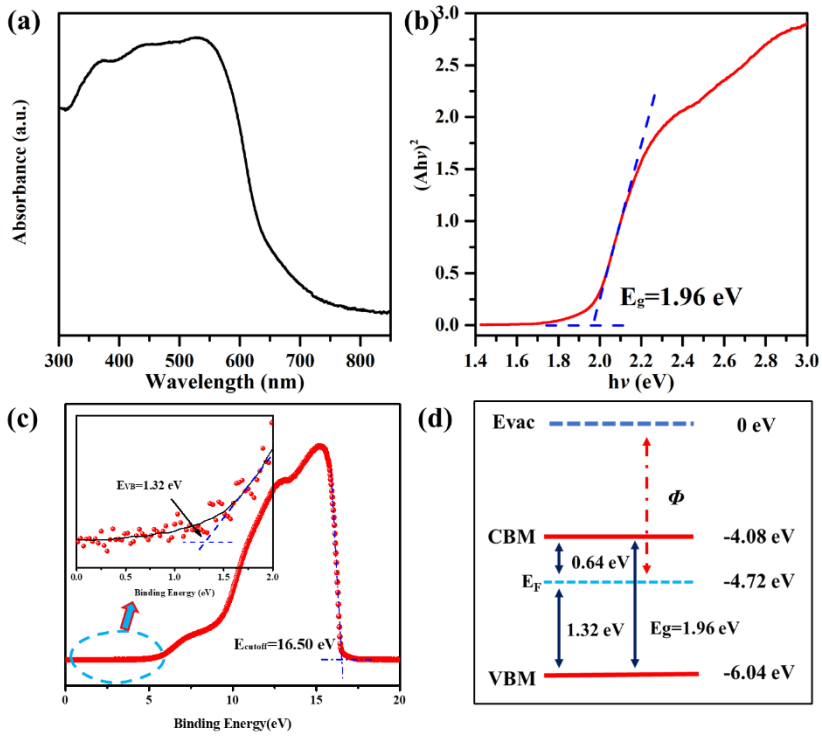

Figure 4.7 (a) UV-visible absorption spectrum and (b) corresponding plot of transformed Kubelka-Munk function versus *hv* of BiSCl nanofibers; (c) UPS spectrum and (d) energy band structure of BiSCl. The inset in (c) shows an enlargement Figure of blue-circled part.

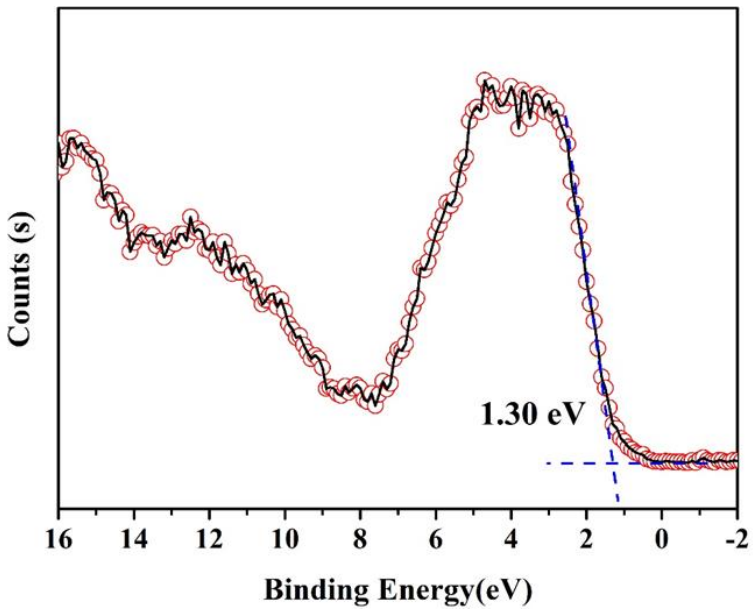

Figure 4.8 Valence-band XPS spectrum of BiSCl nanofibers.

In order to deeply understand the electronic structure of BiSCl, electronic band

structure and partial density of states (DOS) were calculated based on DFT calculations with CASTEP code.[37] Figure 4.9(a) shows that the VBM and CBM are situated at the same k-point of G of Brillouin zone, suggesting that BiSCl is a direct semiconductor. It is known that the direct semiconductors are suitable for the light absorber of thin film solar cells because of their vertical optical transitions, suggesting potential of BiSCl as the absorber for thin film photovoltaic applications.[2] The calculated bandgap transition is 1.93 eV, which is in agreement with those reported by Audzijonis et al. based on DFT method.[41] Our calculation of bandgap is in excellent agreement with the experimental value for the BiSCl nanofibers. The DOS and partial-DOS of Bi, S, and Cl atoms are shown in Figure 4.9(b). The valence band in the range from 0 to -5 eV is composed of p-orbitals of Bi, S and Cl atoms, and s-orbital of Bi atom, where the VBM is dominated by S p-orbital and Cl p-orbital with relatively smaller contribution from Bi p-orbital and s p-orbital. The conduction bands consist of the p-orbitals of Bi, S and Cl atoms, whilst the CBM is dominated by Bi p-orbital.

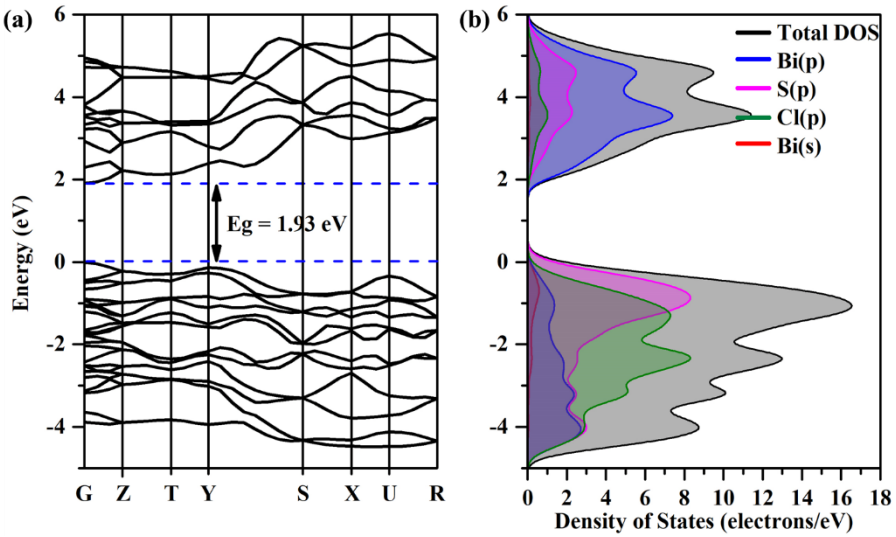

Figure 4.9 (a) Band structure and (b) density of states and partial density of states of BiSCl.

4.3.3 Solar cells performance of BiSCl nanorod array film as light absorber.

As discussed above, BiSCl holds promise for solar cells as a light absorber because it is a direct semiconductor and exhibits strong light absorption in the wavelength range from UV to visible light as shown in Figure 4.7(a). However, to the best of our

knowledge, no any research has been reported on the BiSCl-based solar cells, which may be due to difficult fabrication of its film for the solar cells. Here, we developed a fabrication process of BiSCl-nanorod array film and carried out a preliminary PV study using the BiSCl-nanorod array film as a light absorber to confirm its possibility. We fabricated a BiSCl-based solar cell device with a structure as illustrated in Figure 4.10(a). In the solar cell, a TiO_2 dense film was coated on the surface of FTO conducting glass as a hole blocking layer and a TiO_2 porous film was coated on the TiO_2 dense film. A BiSCl-nanorod array film was fabricated on the TiO_2 porous film using a modified solvothermal process. An electrolyte solution of I_3^-/I^- redox couple was used as the hole-transporting material and a Pt-coated FTO conducting glass was used as a counter-electrode similar to the dye-sensitized solar cells. Figure 4.10 (b) shows the energy band levels diagram of the heterojunction in the solar cell, which suggests a proper band alignment for solar cells.

The FE-SEM image of FTO/TiO_2/BiSCl electrode revealed that the thickness of the porous TiO_2 film was about 10 μm (Figure 4.10(c)). XRD pattern proved that only peaks of BiSCl phase were observed except SnO_2 and TiO_2, indicating a single phase of BiSCl was formed on FTO/TiO_2 electrode (Figure 4.11). The solvothermal treatment can give a uniform BiSCl-nanorod array film, where 1D nanorods of BiSCl with a diameter of about 300 nm and a length of about 1.5 μm vertically oriented on TiO_2 porous film surface (Figure 4.10(d)).

To evaluate the photovoltaic performance of the solvothermally fabricated BiSCl-nanorod array solar cells, the photocurrent-voltage (*J-V*) characteristic curves of the devices were measured under simulated AM 1.5 spectrum (Figure 4.12(a)). The cells performance parameters of PCE, short-circuit photocurrent density (J_{SC}), open-circuit voltage (V_{OC}), and fill factor (*FF*) were evaluated from the *J-V* curves and summarized in Table S2. The narrow distribution of the cells parameters suggests the high stability of the cells performance. The best-performing device features are J_{SC} of 9.87 mA/cm^2, V_{OC} of 0.54 V, *FF* of 25.5%, and PCE of 1.36% (Figure 4.12(a)). Although the PCE of these preliminary solar cells are still low, the relatively larger J_{sc} value revealed the potential of BiSCl-nanorod array as a light absorber for photovoltaics and photoelectric

devices.

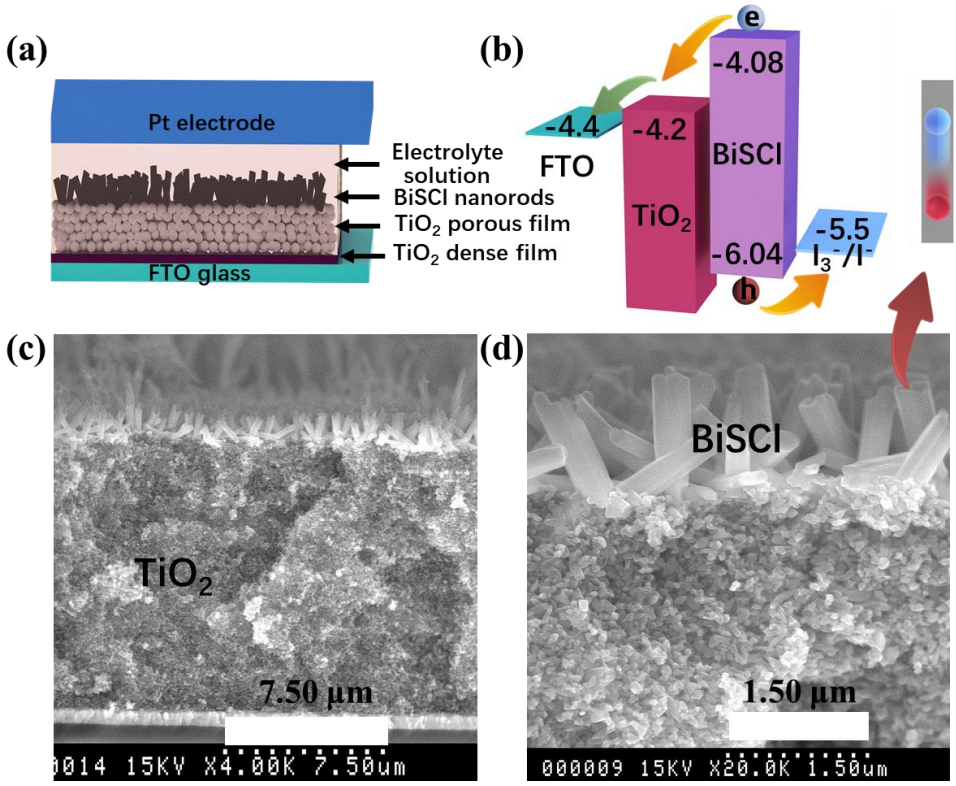

Figure 4.10 (a) Schematic illustration of BiSCl-based solar cell structure. (b) Energy band alignment of the FTO/TiO_2/BiSCl/(I_3^-/I^-) solar cell. (c) Cross-sectional FE-SEM image of FTO/TiO_2/BiSCl electrode. (d) is enlarged FE-SEM image of BiSCl-nanorod array film on TiO_2 porous film surface.

Table 2. Device performance parameters for BiSCl-nanorod array solar cells

Cells	V_{oc} (V)	J_{sc} (mA/cm^2)	FF (%)	PCE (%)
1	0.54	9.868	0.25	1.36
2	0.53	9.668	0.25	1.30
3	0.47	8.396	0.27	1.08
4	0.48	8.600	0.27	1.13
5	0.504	9.200	0.28	1.29

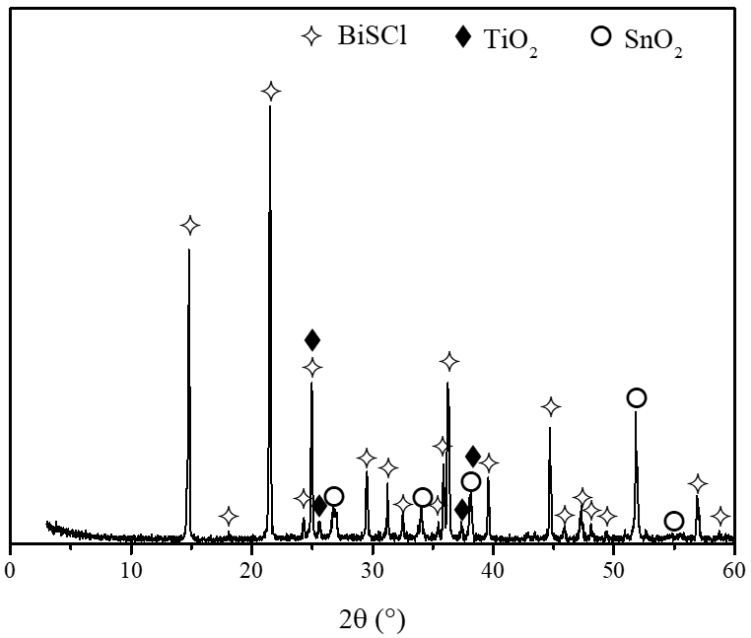

Figure4.11 XRD pattern of BiSCl-nanorod array film on FTO/TiO_2 electrode fabricated by solvothermal treatment at 200 ºC for 12 h.

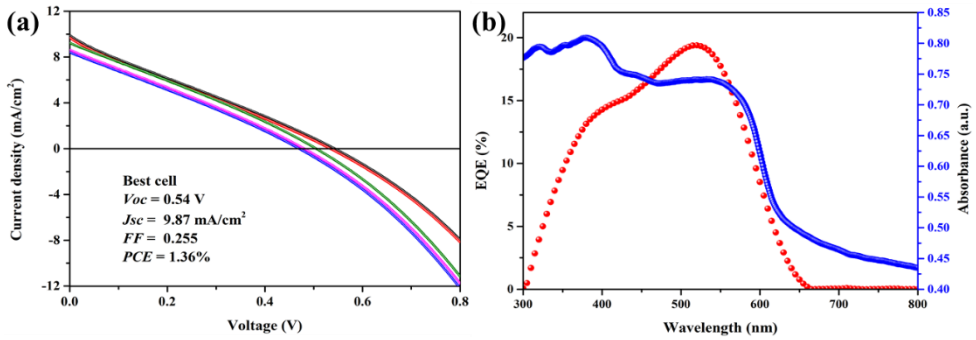

Figure 4.12 (a) *J*−*V* curves of the five FTO/TiO_2/BiSCl/ (I_3^-/I^-)/Pt solar cell devices. (b) UV-visible absorption spectrum of FTO/TiO_2/BiSCl electrode and EQE spectrum of the best solar cell device.

The relatively larger J_{SC} can be attributed to the improvement of carrier transport by the oriented BiSCl-nanorod array parallel to the carrier transporting direction. Zhou et al. reported that the 1D nanocrystals of light absorber can form an efficient carrier transport pathway in the solar cells when they are aligned in the direction of carrier transport.[45] Recently, Xiong et al. suggested that 1D nanostructured BiSI nanorod array can offer advantages of photon absorption and subsequent carrier collection.[26] In

addition, a large number of studies have also demonstrated that such 1D nanostructured array can reduce optical reflection and enhanced optical absorption in the solar cells.[27, 46, 47] The J_{SC} of BiSCl-nanorod array solar cells in the present work is about 3.6 times larger than that of BiSI-nanorod array solar cells reported by Xiong et al.[26] The significant improvement of J_{SC} can be attributed to the uniform and shorter in length of BiSCl-nanorod in the nanorod array film than those in the solar cells based on BiSI nanorod array film. The shorter nanorods can enhance the carriers transport efficiency and reduce the opportunity for the carriers recombination during their transporting process. Furthermore, the uniform BiSCl-nanorod array can enhance optical absorption efficiency owing to their improved antireflective and light-trapping effects because the inter-nanostructure multiple scattering effectively increases the optical path length.[48]

The maximum output voltage of the FTO/TiO_2/BiSCl/(I_3^-/I^-)/Pt solar cell can be calculated as 1.3 V from the CBM of TiO_2 (-4.2 eV) and the redox potential of I_3^-/I^- for the hole-transporting material (-5.5 eV), as shown in Figure 4.10(b).[49] However, the V_{OC} of 0.54 V for the present study is only half of the calculated maximum value. The large internal resistance of the device, including resistance of porous TiO_2 film and resistances at the interfaces of TiO_2/BiSCl and BiSCl/(I_3^-/I^-) solution, may be one of possible factors limiting the V_{OC} value. The large internal resistance of the device can also cause the low *FF*. The lower V_{OC} and *FF* suggest that cell performance can be greatly improved by enhancement of these cell parameters.

Figure 4.12(b) gives the EQE spectrum of the optimum BiSCl-nanorod array solar cell and UV-visible absorption spectrum of the FTO/TiO_2/BiSCl electrode. It can be seen that the device exhibits broad EQE which is consistent with the UV-visible absorption spectrum of the FTO/TiO_2/BiSCl electrode in the wavelength range of visible light from 400-650 nm. A maximum EQE value of 19.4% can be obtained at 520 nm. The drop of EQE values in a wavelength range longer than 550 nm could be an indication of short carrier lifetime.[24] The EQE spectrum is damped by the absorption of SnO_2 in a wavelength range shorter than 350 nm.[24]

Some methods can be used to further improve the performance of the BiSCl-based solar cells. Crystal defects and material engineering are considered as effective factors

to enhance the cell performance. As discussed above, the solvothermal BiSCl nanofibers are Bi-rich and S- and Cl-poor, namely formations of the S and Cl vacancy point defects and midgap state energy levels which could act as recombination centers of electrons and holes, resulting in the low quantum efficiency similar to the cases of the BiSI-, BiSeI-, and BiOI-based solar cells.[9, 22, 24] The Shockley-Queisser limit for a bandgap of 1.9 eV is 1.6 V, namely maximum V_{OC} of 1.6 V is possible for BiSCl-based solar cells.[50, 51] The replacement of the I_3^-/I^- solution with a solid hole transporting material that has a VBM lower than I_3^-/I^- redox potential but higher than the VBM of BiSCl, such as poly (fluorene-2,7-diyl) (F8, HOMO = -5.8 eV) and poly(9,9-dioctylfluorene-alt-benzothiadiazole) (F8BT, HOMO = -5.9 eV) would be an efficient way to improve V_{OC}.[52, 53] Move over, the optimization of the crystal morphology of light absorber is also an efficient way to improve the device performance. The smaller BiSCl-nanorod array can offer more efficient optical absorption and light-trapping effect to enhance J_{SC}. Very recently, Tiwari et al. fabricated a SnO_2/BiSI/F8 solar cells using a flake-shaped BiSI film as the light absorber and gave the champion PCE of 1.32% for the BiSI-based solar cells.[24]

4.4 Conclusions

In conclusion, single-crystalline of BiSCl nanofibers were synthesized by a facile solvothermal approach for the first time. BiSCl is an n-type semiconductor with a direct bandgap of 1.96 eV and exhibits a strong light absorption in the wavelength range from UV to visible light. The VBM is dominated by S and Cl p-orbital, whilst the CBM is dominated by Bi p-orbital. Uniform BiSCl-nanorod array film can be fabricated on porous TiO_2 electrode by a modified solvothermal process. The photovoltaic devices with architecture of FTO/TiO_2/BiSCl/ (I_3^-/I^-)/Pt using the BiSCl-nanorod array film exhibit a PCE of 1.36% and a relative larger J_{SC} of 9.87 mA/cm^2, revealing the potential of the BiSCl-nanorod array light absorber for a new type of solar cell that can be fabricated by low-cost solution process. The relatively larger J_{SC} can be attributed to

the homogeneous BiSCl-nanorod array film by improving carriers transport to reduce their recombination during the transporting process. This work is expected to contribute to broaden the Bi-based chalcohalide solar cells and to provide some clues for developing low-cost and environment-friendly solar cells.

4.5 References

1. M. A. Green, E. D. Dunlop, J. Hohl-Ebinger, M. Yoshita, N. Kopidakis and A. W. Y. Ho-Baillie, *Progress in Photovoltaics: Research and Applications*, 2019, **28**, 3-15.
2. A. M. Ganose, K. T. Butler, A. Walsh and D. O. Scanlon, *Journal of Materials Chemistry A*, 2016, **4**, 2060-2068.
3. A. Slikkerveer and F. A. de Wolff, *Med Toxicol Adverse Drug Exp*, 1989, **4**, 303-323.
4. A. Walsh, D. J. Payne, R. G. Egdell and G. W. Watson, *Chem Soc Rev*, 2011, **40**, 4455-4463.
5. F. Wei, Z. Deng, S. Sun, F. Zhang, D. M. Evans, G. Kieslich, S. Tominaka, M. A. Carpenter, J. Zhang, P. D. Bristowe and A. K. Cheetham, *Chemistry of Materials*, 2017, DOI: 10.1021/acs.chemmater.6b03944.
6. D. Tiwari, D. Alibhai and D. J. Fermin, *ACS Energy Letters*, 2018, **3**, 1882-1886.
7. R. E. Brandt, R. C. Kurchin, R. L. Hoye, J. R. Poindexter, M. W. Wilson, S. Sulekar, F. Lenahan, P. X. Yen, V. Stevanovic, J. C. Nino, M. G. Bawendi and T. Buonassisi, *J Phys Chem Lett*, 2015, **6**, 4297-4302.
8. A. J. Lehner, D. H. Fabini, H. A. Evans, C.-A. Hébert, S. R. Smock, J. Hu, H. Wang, J. W. Zwanziger, M. L. Chabinyc and R. Seshadri, *Chemistry of Materials*, 2015, **27**, 7137-7148.
9. A. M. Ganose, S. Matsumoto, J. Buckeridge and D. O. Scanlon, *Chem Mater*, 2018, **30**, 3827-3835.
10. A. M. Ganose, C. N. Savory and D. O. Scanlon, *Chem Commun (Camb)*, 2016, **53**, 20-44.
11. Y. Sasaki, *Journal of Applied Physics*, 1965, **4**, 614.
12. D. Siapkas, *Ferroelectrics*, 1974, **7**, 295-296.
13. G. P. Voutsas and P. J. Rentzeperis, *Zeitschrift für Kristallographie - Crystalline Materials*, 1980, **152**.
14. W.-W. Liu and R.-F. Peng, *Journal of Electronic Science and Technology*, 2020, **18**, 100020.
15. K. Zhao, X. Zhang and L. Zhang, *Electrochemistry Communications*, 2009, **11**, 612-

615.

16. F. Demartin, C. M. Gramaccioli and I. Campostrini, *Mineralogical Magazine*, 2018, **74**, 141-145.
17. L. Zhu, Y. Xie, X. Zheng, X. Yin and X. Tian, *Inorganic Chemistry*, 2002, **41**, 4560-4566.
18. R. He, D. Xu, B. Cheng, J. Yu and W. Ho, *Nanoscale Horizons*, 2018, **3**, 464-504.
19. L. Li and M. Wang, 2016, DOI: https://doi.org/10.5772/62206.
20. J. Hu, X. Wu, C. Huang, W. Fan and X. Qiu, *Applied Surface Science*, 2016, **387**, 45-50.
21. Y. Guo, Y. Zhang, N. Tian and H. Huang, *ACS Sustainable Chemistry & Engineering*, 2016, **4**, 4003-4012.
22. R. L. Z. Hoye, L. C. Lee, R. C. Kurchin, T. N. Huq, K. H. L. Zhang, M. Sponseller, L. Nienhaus, R. E. Brandt, J. Jean, J. A. Polizzotti, A. Kursumovic, M. G. Bawendi, V. Bulovic, V. Stevanovic, T. Buonassisi and J. L. MacManus-Driscoll, *Adv Mater*, 2017, **29**.
23. N. T. Hahn, A. J. E. Rettie, S. K. Beal, R. R. Fullon and C. B. Mullins, *The Journal of Physical Chemistry C*, 2012, **116**, 24878-24886.
24. D. Tiwari, F. Cardoso-Delgado, D. Alibhai, M. Mombrú and D. J. Fermín, *ACS Applied Energy Materials*, 2019, **2**, 3878-3885.
25. T. J. Kempa, R. W. Day, S.-K. Kim, H.-G. Park and C. M. Lieber, *Energy & Environmental Science*, 2013, **6**, 14.
26. J. Xiong, Z. You, S. Lei, K. Zhao, Q. Bian, Y. Xiao and B. Cheng, *ACS Sustainable Chemistry & Engineering*, 2020, **8**, 13488-13496.
27. G. Otnes and M. T. Borgström, *Nano Today*, 2017, **12**, 31-45.
28. M. Yu, Y. Z. Long, B. Sun and Z. Fan, *Nanoscale*, 2012, **4**, 2783-2796.
29. M. D. Kelzenberg, S. W. Boettcher, J. A. Petykiewicz, D. B. Turner-Evans, M. C. Putnam, E. L. Warren, J. M. Spurgeon, R. M. Briggs, N. S. Lewis and H. A. Atwater, *Nat Mater*, 2010, **9**, 239-244.
30. Z. Fan, H. Razavi, J. W. Do, A. Moriwaki, O. Ergen, Y. L. Chueh, P. W. Leu, J. C. Ho, T. Takahashi, L. A. Reichertz, S. Neale, K. Yu, M. Wu, J. W. Ager and A. Javey, *Nat*

Mater, 2009, **8**, 648-653.

31. J. H. Im, J. Luo, M. Franckevicius, N. Pellet, P. Gao, T. Moehl, S. M. Zakeeruddin, M. K. Nazeeruddin, M. Gratzel and N. G. Park, *Nano Lett*, 2015, **15**, 2120-2126.
32. J. Liu, L. Zhu, S. Xiang, H. Wang, H. Liu, W. Li and H. Chen, *ACS Sustainable Chemistry & Engineering*, 2019, **7**, 16927-16932.
33. B. Cao, H. Liu, L. Yang, X. Li, H. Liu, P. Dong, X. Mai, C. Hou, N. Wang, J. Zhang, J. Fan, Q. Gao and Z. Guo, *ACS Appl Mater Interfaces*, 2019, **11**, 33770-33780.
34. R. Nitsche and W. J. Merz, *Journal of Physics and Chemistry of Solids*, 1960, **13**, 154-155.
35. M. Ruck, P. F. Poudeu Poudeu and T. Söhnel, *Zeitschrift für anorganische und allgemeine Chemie*, 2004, **630**, 63-67.
36. C. Chen, L. Xu, G. A. Sewvandi, T. Kusunose, Y. Tanaka, S. Nakanishi and Q. Feng, *Crystal Growth & Design*, 2014, **14**, 5801-5811.
37. S. J. Clark, M. D. Segall, C. J. Pickard, P. J. Hasnip, M. I. J. Probert, K. Refson and M. C. Payne, *Zeitschrift für Kristallographie - Crystalline Materials*, 2005, **220**.
38. J. P. Perdew, A. Ruzsinszky, G. I. Csonka, O. A. Vydrov, G. E. Scuseria, L. A. Constantin, X. Zhou and K. Burke, *Phys Rev Lett*, 2008, **100**, 136406.
39. Y. C. Choi and E. Hwang, *Nanomaterials (Basel)*, 2019, **9**.
40. J. Tauc, R. Grigorovici and A. Vancu, *physica status solidi (b)*, 1966, **15**, 627-637.
41. A. Audzijonis, L. Žigas, G. Gaigalas, R. Sereika and B. Žygaitienė, *Journal of Cluster Science*, 2010, **21**, 577-589.
42. H. Zhang, S. H. Sun, J. C. Liu, F. Hong, Y. Zhu, B. Zhou and Y. M. Hu, *Nano*, 2020, **15**, 2050116.
43. A. Kahn, *Materials Horizons*, 2016, **3**, 7-10.
44. J. You, Z. Hong, Y. M. Yang, Q. Chen, M. Cai, T. B. Song, C. C. Chen, S. Lu, Y. Liu, H. Zhou and Y. Yang, *ACS Nano*, 2014, **8**, 1674-1680.
45. Y. Zhou, L. Wang, S. Chen, S. Qin, X. Liu, J. Chen, D.-J. Xue, M. Luo, Y. Cao, Y. Cheng, E. H. Sargent and J. Tang, *Nature Photonics*, 2015, **9**, 409-415.
46. J. Zhu, Z. Yu, S. Fan and Y. Cui, *Materials Science and Engineering: R: Reports*, 2010, **70**, 330-340.

47. J. Wallentin, N. Anttu, D. Asoli, M. Huffman, I. Aberg, M. H. Magnusson, G. Siefer, P. Fuss-Kailuweit, F. Dimroth, B. Witzigmann, H. Q. Xu, L. Samuelson, K. Deppert and M. T. Borgstrom, *Science*, 2013, **339**, 1057-1060.
48. B. Hua, Q. Lin, Q. Zhang and Z. Fan, *Nanoscale*, 2013, **5**, 6627-6640.
49. G. A. Sewvandi, Z. Tao, T. Kusunose, Y. Tanaka, S. Nakanishi and Q. Feng, *ACS Appl Mater Interfaces*, 2014, **6**, 5818-5826.
50. W. Shockley and H. J. Queisser, *Journal of Applied Physics*, 1961, **32**, 510-519.
51. A. Polman, M. Knight, E. C. Garnett, B. Ehrler and W. C. Sinke, *Science*, 2016, **352**, aad4424.
52. D.-H. Hwang, J.-D. Lee, J.-M. Kang, S. Lee, C.-H. Lee and S.-H. Jin, *Journal of Materials Chemistry*, 2003, **13**, 1540.
53. Y. Zhang and P. W. M. Blom, *Applied Physics Letters*, 2011, **98**, 143504.

Chapter V

Summary

In the present study, several facile solvothermal processes were developed for the synthesis of a series of bismuth chalcohalides. The systematical studies were carried out on the photoelectric behaviors of these bismuth chalcohalides. The low cost processes for fabrication of their films were developed also for the photovoltaic studies. The results suggest that the bismuth chalcohalides are promising materials as new type of light absorber materials for solar cells. The main results of this study are summarized as follows:

In Chapter I, the properties of semiconductor for photovoltaic devices, main characteristics and history of photovoltaic devices are described. Furthermore, Bi-VI-VII-type semiconductors and their applications are also presented. In addition, the purposes of this research are also clarified.

In chapter II, systematic studies on the syntheses and formation reactions of rod-like $Bi_{13}S_{18}I_2$ and BiSI under solvothermal conditions and their photoelectric behavior are described. The formations of BiSI and $Bi_{13}S_{18}I_2$ are strongly dependent on the S/Bi mole ratio, reaction temperature, and solvent in the reaction system. The photoelectric results revealed that $Bi_{13}S_{18}I_2$ is an n-type semiconductor with a narrow bandgap of 0.75 eV, and possesses a strong light absorbance in the wavelength range from ultraviolet (UV) to near-IR (NIR) light, suggesting the promising light absorber material for solar cells. Moreover, for the photovoltaic study of $Bi_{13}S_{18}I_2$, a modified solvothermal process was developed to fabricate a uniform $Bi_{13}S_{18}I_2$ film on the porous TiO_2 electrode. The preliminary photovoltaic results demonstrated a PCE of 0.85% of the $Bi_{13}S_{18}I_2$-based solar cell for the first time.

In chapter III, a novel solvothermal process to synthesize high quality stoichiometric $Bi_{13}S_{18}X_2$ compounds, fundamental photoelectric and photovoltaic behaviors of these compounds are addressed. The chemical composition of

$(Bi^{3+})_{12}(B_2^{4+})_{0.5}(S^{2-})_{18}(X^-)_2$ and the triangular tunnel structure of hexagonal system with space group of P3 were determined by Rietveld refinements of XRD results for the first time, which resolves the arguments on their structures. $Bi_{13}S_{18}Cl_2$, $Bi_{13}S_{18}Br_2$ and $Bi_{13}S_{18}I_2$ are indirect n-type semiconductors, displaying a strong and broad light absorption in the range from UV to NIR light with narrow bandgaps of 0.76, 0.80 and 0.81 eV, respectively. Their band structures were given for the first time, which shows their possibilities as photovoltaic materials. Furthermore, a novel facile PVD approach was developed for the low cost fabrication of thin BSX films for solar cells. Uniform $Bi_{13}S_{18}X_2$ thin films can be fabricated easily using this process. The photovoltaic study demonstrated that the $Bi_{13}S_{18}Cl_2$, $Bi_{13}S_{18}Br_2$ and $Bi_{13}S_{18}I_2$-based solar cells exhibited PCEs of 0.91, 1.12 and 0.75%, respectively, for the first time.

In chapter IV, a novel solvothermal process was successfully developed to synthesize single crystalline BiSCl nanofibers, which offers an opportunity to systemically study its photoelectric behavior. BiSCl nanofibers is a direct n-type semiconductor with a bandgap of 1.96 eV, corresponding the strong light absorption in a wavelength range from UV to visible light, which suggests potential application as a light absorber for solar cells. The band structure and band energy level of BiSCl were given. The solvothermal process was modified to fabricate a BiSCl-nanorod array film for high performance solar cells. The BiSCl-based solar cell with an architecture of FTO/TiO_2/BiSCl/(I_3^-/I^-)/Pt possesses a proper band energy alignment, which gave a PCE of 1.36% with a large J_{SC} of 9.87 mA/cm^2.

As described above, the present study provides some new significant knowledge in the research field of the bismuth chalcohalide semiconductor materials, including the formation mechanism under solvothermal conditions, photoelectric properties and photovoltaic behavior as Bi-VI-VII semiconductors for solar cells. Firstly, the solvothermal reactions can be adopted to facile and efficient synthesis processes for the bismuth chalcohalides. In these processes, the formed phases are dependent strongly on the precursors used, S/Bi mole ratio, reaction temperature, and solvent in reaction system, which can serve as a guide to prepare other compounds of Bi-VI-VII. These bismuth chalcohalides possess ribbon-like and chain structures. The formations of rod-

like crystal morphologies in the solvothermal processes can be achieved to their inherent ribbon-like and chain structures.

Up to now, almost no studies on the photoelectric properties of $Bi_{13}S_{18}Cl_2$, $Bi_{13}S_{18}Br_2$, $Bi_{13}S_{18}I_2$, and BiSCl compounds have been reported. The fundamental photoelectric studies on the photoelectric properties of these compounds clarified their bandgaps, band energy levels, and type of semiconductor for the first time, which are significant physical parameters for the applications of these materials to the semiconductor materials, photoelectric materials, and photovoltaic materials. In this sense, this study is a pioneer work for Bi-VI-VII semiconductors.

In the present study, two novel processes, modified solvothermal process and facile PVD process, were developed to fabricate uniform films of bismuth chalcohalides. These processes can be applied to low cost fabrications of bismuth-based solar cells as well as other electronic devices of Bi-VI-VII semiconductors. These two processes can provide the bismuth chalcohalide films with different morphologies, which offers an opportunity to study to morphology effect on the solar cell performance. Their nanorod array films can be fabricated by solvothermal processes. Such nanorod array films are beneficial to enhancing photo absorption, promoting carrier collection and transport, and reducing optical reflection as the light absorber layer for solar cells.

The photovoltaic performances of $Bi_{13}S_{18}Cl_2$, $Bi_{13}S_{18}Br_2$, $Bi_{13}S_{18}I_2$, and BiSCl compounds are clarified for the first time. The systematical study on $Bi_{13}S_{18}X_2$ (X: Cl, Br, I) reveals that $Bi_{13}S_{18}Br_2$ is the most promising light absorber, which gives the next research direction for the $Bi_{13}S_{18}X_2$-based solar. The photovoltaic study results for BiSX (X: Cl, Br, I) suggest higher solar cell performance of BiSCl than that of BiSI. Comparison of light absorber films fabricated by solvothermal process and PVD process can give some knowledge about morphology effect on the photovoltaic performance. The light absorber of $Bi_{13}S_{18}I_2$ prepared by PVD possess a high density and surface roughness, which can enhance the light absorption and light-scattering effect to enhances light harvesting of the $Bi_{13}S_{18}I_2$ film, resulting in the higher short-circuit photocurrent density (J_{SC}) value than that of the solvothermal process. However, the nanorod-array light absorber prepared by modified solvothermal processes can form

an efficient carriers transport pathway in the solar cells when they are aligned in the direction of carrier transport, generating relatively larger J_{SC}.

The results described above prove the potential application of bismuth chalcohalides as non-toxic and stable light absorber for a new type of solar cells can be fabricated by a facile solvothermal and PVD approaches. At the same time, it also provides facile methods for other film based photoelectric devices application.

In our next challenges, we will, firstly, focus on optimum architecture of the solar cells used the bismuth chalcohalide light absorbers, including proper band energy alignment and materials. Replacement of the hole transport material of electrolyte solution with a suitable solid hole transport layer will be a promising method to further improve the photovoltaic performance. This requires skilled techniques to prepare the different layers in the cell device. To characterize the effect on cell performance, such as time-correlated single photon counting measurements, external quantum efficiency measurement, are necessary to deeply understand the photovoltaic mechanism and the interrelation of distinct layers. Of course, the thickness and morphology control of light absorber play crucial roles for high PCE. The bismuth chalcohalides nanorod arrays film prepared by modified solvothermal process and high density and uniform film made by PVD have distinct influence for solar cells parameters.

Besides, bismuth chalcohalides have high potential as photocatalyst. The particle size and morphology control, and alloyed compound are possible solutions for effectively enhancing photocatalytic performance. The application of bismuth chalcohalides to other electronic devices is also interesting research area.

Publications

Publications in Journals

1. **Li, S.**; Xu, L.; Kong, X.; Kusunose, T.; Tsurumachi, N.; Feng, Q., Bi13S18X2-Based Solar Cells (X = Cl, Br, I): Photoelectric Behavior and Photovoltaic Performance. *Physical Review Applied* **2021,** *15* (3).
2. **Li, S.**; Xu, L.; Kong, X.; Kusunose, T.; Tsurumachi, N.; Feng, Q., Bismuth chalcogenide iodides Bi13S18I2 and BiSI: solvothermal synthesis, photoelectric behavior, and photovoltaic performance. *Journal of Materials Chemistry C* **2020,** *8* (11), 3821-3829.
3. **Li, S.**; Zhang, C.; Min, F.; Dai, X.; Pan, C.; Cheng, W., Electronic structural properties of BiOF crystal and its oxygen vacancy from first-principles calculations. *Russian Journal of Physical Chemistry A* **2017,** *91* (12), 2425-2430.
4. Zhang, W.; **Li, S.**; Ma, H.; Hu, D.; Kong, X.; Uemura, S.; Kusunose, T.; Feng, Q., Ferroelectric mesocrystalline BaTiO3/BaBi4Ti4O15 nanocomposite: formation mechanism, nanostructure, and anomalous ferroelectric response. *Nanoscale* **2019,** *1111()* (9), 3837-3846.
5. Xu, L.; **Li, S.**; Uemura, S.; Kusunose, T.; Kong, X.; Feng, Q., Polymorphic Evolution of TiO2 in Hydrothermal Reaction System of Layered Titanate Nanosheets. *ChemistrySelect* **2018,** *3* (30), 8703-8712.
6. Xu, L.; Fang, H.; **Li, S.**; Zhu, J.; Pan, C.; Pan, Y.; Feng, Q., Tailored Hydrothermal Synthesis of Specific Facet-Dominated TiO2 Nanocrystals from Lepidocrocite-Type Layered Titanate Nanosheets: Systematical Investigation and Enhanced Photocatalytic Performance. *Langmuir* **2020,** *36* (16), 4477-4495.
7. Zhang, W.; Ma, H.; **Li, S.**; Hu, D.; Kong, X.; Uemura, S.; Kusunose, T.; Feng, Q., Anomalous piezoelectric response of ferroelectric mesocrystalline BaTiO3/Bi0.5Na0.5TiO3 nanocomposites designed by strain engineering. *Nanoscale* **2018,** *10* (17), 8196-8206.
8. **Li, S.**; Xu, L.; Kong, X.; Kusunose, T.; Tsurumachi, N.; Feng, Q., Enhanced

photovoltaic performance of biscl solar cells through nanorod array. ChemSuschem. (under review)

Publications in Conferences

1. **Sen Li**, Qi Feng., Bi-based Organic Inorganic Hybrid Halide Perovskite Compound for Solar Cells. 2016 年日本化学会中国四国支部大会, ポスター, Kagawa, P102, 2016/11/05.
2. **Sen Li**, Qi Feng., Synthesis and Characterization of Bismuth Chalcogenide Halide Compounds for Solar Cells. 第 23 回ヤングセラミクストーティング in 中四国, Okayama, P89, 2016/12/17.
3. **Li Sen**, Xu Linfeng, Feng Qi., Synthesis and Characterization of Bismuth Chalcogenide Halide Compounds for Solar Cells. 2017 年日本化学会中国四国支部大会,Tottori, P148, 2017/11/11.
4. **Li Sen**, Xu Linfeng, Feng Qi., Synthesis and Characterization of Bismuth Chalcogenide Halide Compounds for Solar Cells. 第 56 回セラミックス基礎科学討論会, Tsukuba, P56, 2018/01/11.
5. **Sen Li**, Linfeng X u, Qi Feng., Synthesis and Characterization of Bismuth Chalcohenide Halide Compounds for Solar Cells. 第 57 回セラミックス基礎科学討論会, Sendai, P7, 2019/01/16-17.
6. **Li Sen**, Xu Linfeng, Qi Feng., Bismuth chalcogenide iodides of $Bi_{13}S_{18}I_2$: Solvothermal Synthesis, Photoelectronic Behavior, and Photovoltaic Performance. The 13th Pacific Rim Conference of Ceramic Societies, Okinawa, P68, 2019/10/27-11/1.

Acknowledgment

I want to express the depth of my gratitude to many people who gave me a great help; I could not have completed my doctoral program without the help. Definitely, the past 6 years in Kagawa university, Japan will become my most rememberable and precious time in my life.

I would like to firstly thank my supervisor, Prof. **Qi Feng**, for his kind guidance, cultivation, and continuous supervision, excellent advice and continuous encouragement towards the completion of this present research successfully in time. His rigorous and pragmatic academic attitude is worth studying for my life. Besides the fundamental knowledge he had taught me, more importantly, he realized early that I have a strong desire to research, anything, and you gave me the freedom to develop. And I'm also appreciate the wife of my Prof. Feng, Lin Yu, for her much supports and patience on our research supervisor team, for her delicious foods.

I would also like to express my thanks to my vice supervisors Prof. Takafumi Kusunose and Prof. Noriaki Tsurumachi for their kind advice, valuable suggestion, necessary support, and enthusiastic assistances to my Ph. D program. In addition, I would like to express my thanks to Prof. Chengling Pan and Associate Prof. Shaoding Sheng (Anhui University of Science and Technology) for recommending and encouraging me to study in Japan. Grateful acknowledgements are to Senior Linfeng Xu (Anhui University of Science and Technology), Wenxiong Zhang (Tokyo University), Xingang kong (Shaanxi University of Science and Weixing Zhao (Baoji University of Arts and Science) for their valuable suggestion, enthusiastic assistances and life experience.

I would like to acknowledge the former and current administrative staff at Kagawa University. Thank you very much for making my life easier in Japan: Especially, I would like to thank Qing Zhang who offer me great help in study and life. In addition, I also want to give my appreciation to Ms. Yuka Kojima for teaching me Japanese and helping me prepare the interview of the scholarship.

I would like to thank the scientists, who introduced me to the facilities at Kagawa University. Special thanks to Mr. Toshitaka Nakagawa (FE-SEM) and Ms. Ayami Nishioka. I greatly enjoyed your expertise with the electron microscopes. Thank you for giving me so many ideas to solve my problems.

I also owe my sincere gratitude to my friends and fellow classmates in our research group, who gave me many helps and much pleasures on my life and study.

Lastly, I would like to acknowledge my family for their love, understanding and support throughout my research and life in Japan, in particular, I sincerely appreciate my best friend, Shuo Yu, for her accompany and encouragement, and the most precious and unforgettable time in UK.

.

Sen Li

Feng Laboratory, Department of Advanced Materials Science,

Faculty of Engineering and Design

Kagawa University, Kagawa, Japan

June, 2021